

Phonons, electron-phonon coupling and charge transport in low-dimensional materials

Présentée le 1^{er} mai 2023

Faculté des sciences et techniques de l'ingénieur
Laboratoire de théorie et simulation des matériaux
Programme doctoral en science et génie des matériaux

pour l'obtention du grade de Docteur ès Sciences

par

Norma RIVANO

Acceptée sur proposition du jury

Dr J. C. Plummer, président du jury
Prof. N. Marzari, Dr G. Pizzi, directeurs de thèse
Prof. B. Kozinsky, rapporteur
Prof. K. S. Thygesen, rapporteur
Prof. A. Kis, rapporteur

... je crois que rien n'est vain de ce qui fuit aimé.
A. Blanchard

Alla mia famiglia.

Acknowledgments

PhDs are often compared to a long and intense journey, and mine is no exception. As I reach the end of this journey, I would like to express my sincere gratitude to the many people who have supported me and contributed to the work discussed in this thesis.

First and foremost, I thank my supervisor, Nicola Marzari, for providing me with the opportunity to work in a stimulating and unique environment. I am grateful for the trust he placed in me, the granted freedom, and the scientific and human guidance. His invaluable mentorship has played a key role in my personal and professional growth.

I am also deeply grateful to my mentors and colleagues who have contributed to my success in completing this journey. My co-supervisor, Giovanni Pizzi, provided me with invaluable scientific guidance and feedbacks. I would also like to acknowledge Davide Campi for all the scientific discussions and Luciano Colombo for his constant encouragement and chats. I owe a special debt of gratitude to Thibault Sohler, whose unwavering support, invaluable mentorship, and exceptional kindness and humanity have been a constant source of strength throughout my PhD. Without his guidance, this thesis would not have been possible.

I am grateful to all the members of the THEOS group, past and present, who have made these years in Lausanne unforgettable; unfortunately they are too many to be listed here. A special thanks go to Francesco, Tommaso, and Riccardo, with whom I started and finished this chapter of our lives together. I will always cherish the memories we shared. Thanks to Giuliana, Chiheb, Luca, Loris, Chiara, Lorenzo, Michele and Arianna. I will miss all of you immensely.

To my friends from Cagliari, I am grateful for the long-lasting and solid examples of friendship, which have served as a reminder to stay true to myself and persevere through personal and professional challenges.

Finally, I want to thank my family for their unconditional love and support. The valuable lessons and happy childhood they have gifted me have been the backbone of my journey, and for this, I am eternally grateful.

Lausanne, 24 March 2023

Abstract

Over the past few decades, nanostructures have garnered significant attention due to their potential for embodying new physical paradigms and delivering cutting-edge technological applications. Dimensionality strongly affects the vibrational, electron-phonon, and transport properties of materials by carrying unique and profound signatures that are key to spectroscopic characterization and, more generally, to the future of nanotechnology. This thesis aims to contribute to the general progress in understanding and predicting from first principles these dimensionality signatures. To achieve this goal, we combine analytical modeling and algorithmic development, as well as automation techniques targeting high-throughput calculations.

The first part of the thesis focuses on one-dimensional (1D) systems, including atomic chains, polymers, nanotubes, and nanowires. Our theoretical understanding and computational tools are less developed in this case compared to higher-dimensional systems, i.e., two-dimensional (2D) and three-dimensional (3D) bulk materials.

From the modeling perspective, the ability to simulate the physics of 1D systems from first-principles is highly desirable and density-functional perturbation theory represents a powerful tool. In the past, its combination with analytical models has allowed us to reach a comprehensive understanding of phonons and their coupling to electrons in 3D and 2D materials. However, most of the available *ab-initio* codes rely on periodic-boundary conditions in the three spatial dimensions, which poses some challenges when dealing with reduced dimensionality. Here, we develop an implementation of density-functional and density-functional perturbation theory tailored for 1D systems. The key ingredient is the inclusion of the Coulomb cutoff, a reciprocal space technique designed to correct for the spurious interactions arising between the periodic images in periodic-boundary conditions. Our work restores the proper 1D open-boundary conditions, unveiling the true response of the isolated 1D system.

We then investigate polar-optical, infrared-active, phonons and their coupling to electrons in 1D semiconductors and insulators. A microscopic understanding of these phonons in 3D materials is a pillar of solid-state physics, but that same understanding breaks down in lower dimensions, with key consequences for properties such as transport and for spectroscopic

characterization. In 3D, the local dipoles parametrized by the Born effective charges affect the dispersion relations of these phonons by driving a dielectric frequency shift that is constant across the Brillouin zone: the longitudinal-transverse optical splitting. This shift breaks down at the zone center in lower dimensions with an asymptotic behavior ruled by dimensionality; linear in 2D systems, while still debated in 1D. This work provides for the first time, to the best of our knowledge, a definite answer to this challenge by developing the missing theory for the 1D case, an analytical model, and a validation from first-principles simulations. This is possible thanks to the newly developed density-functional perturbation theory implementation. Notably, such a model enables the interpretation of Raman and infrared spectra of 1D systems, which we expect to be of great use for material characterization at the nanoscale. Additionally, the same model leads to another relevant analytical result: the Fröhlich electron-phonon coupling, which plays a crucial role in transport as well as polaritronics and many other fields.

The second part of the thesis focuses on 2D materials, also known as Flatland. Here, we specifically investigate phonon-limited charge transport in electrostatically doped semiconductors with a two-fold ambition. On the one hand, we are drawn to the computational quest for high-mobility candidates by exploring large databases of materials. On the other hand, we focus on individual materials and seek to engineer their transport properties. In this respect, we discuss our contributions within a joint theoretical and experimental collaboration that aims to enhance the performances of 2D channels for field-effect transistors by applying a permanent strain. Both efforts are pursued by combining density-functional perturbation theory, accounting explicitly for dimensionality and doping, with Boltzmann transport theory beyond the relaxation time approximation. All this is powered by the AiiDA materials informatics infrastructure, an open-source Python platform designed to automate and manage simulations and resulting data while ensuring preservation and searchability.

Keywords: Low-dimensional materials, semiconductors, screening, phonons, polar-optical phonons, Raman and infrared spectroscopic characterization, electron-phonon interactions, charge transport, material discovery, strain engineering.

Sommario

Negli ultimi decenni, le nanostrutture hanno suscitato un crescente interesse, motivato dalla loro promessa di proporre nuovi paradigmi fisici e di consentire applicazioni tecnologiche all'avanguardia. La dimensionalità di un materiale ha un forte impatto sulle sue proprietà vibrazionali, di interazione elettrone-fonone e di trasporto, portando a firme ben definite e fondamentali per la caratterizzazione spettroscopica e il futuro della nanotecnologia. Questa tesi intende contribuire al progresso generale nella comprensione e nella predizione di queste firme di dimensionalità, partendo da principi primi. A tale scopo, combineremo modelli analitici con lo sviluppo di nuovi algoritmi e tecniche di automatizzazione mirate, al fine di rendere possibili calcoli su un grande numero di dati in tempi rapidi.

La prima parte della tesi è dedicata ai materiali unidimensionali (1D), che includono catene di atomi, polimeri, nanotubi e nanofili. La nostra comprensione teorica, così come gli strumenti computazionali a nostra disposizione, sono meno maturi in questo caso rispetto ai materiali con dimensionalità più elevata, ovvero bidimensionali (2D) e tridimensionali (3D).

Dal punto di vista computazionale, è altamente desiderabile la capacità di simulare la fisica dei sistemi unidimensionali (1D) partendo da principi primi. A tale scopo, la teoria delle perturbazioni applicata alla teoria del funzionale densità rappresenta uno strumento potente, già utilizzato in passato in combinazione con modelli analitici per raggiungere una comprensione completa dei fononi e del loro accoppiamento con gli elettroni nei materiali 3D e 2D. Tuttavia, la maggior parte dei codici *ab-initio* disponibili si basano su condizioni al contorno periodiche nelle tre dimensioni spaziali, il che rappresenta una sfida quando si ha a che fare con materiali a bassa dimensionalità. In questo lavoro, abbiamo sviluppato un'implementazione della teoria del funzionale densità, e della teoria delle perturbazioni ad essa applicata, su misura per i sistemi 1D. L'ingrediente chiave è l'inclusione del Coulomb cutoff, una tecnica in spazio reciproco progettata per correggere le interazioni spurie che sorgono tra le immagini periodiche in condizioni al contorno periodiche. Il nostro lavoro ripristina le corrette condizioni al contorno aperte in 1D, svelando così la vera, risposta fisica del sistema unidimensionale isolato.

Sviluppata l'implementazione, ci concentriamo sull'analisi dei fononi polari-ottici, attivi

nell'infrarosso, e sul loro accoppiamento con gli elettroni nei semiconduttori e isolanti 1D. La comprensione microscopica di questi fononi nei materiali 3D rappresenta un pilastro fondamentale della fisica dello stato solido. Tuttavia, tale comprensione viene meno nelle nanostrutture, con importanti conseguenze sia per le proprietà dei materiali, come quelle di trasporto, sia per la loro caratterizzazione spettroscopica. Nei materiali 3D, i dipoli locali parametrizzati dalle Born effective charge influenzano le relazioni di dispersione dei fononi polari-ottici, causando un aumento delle loro frequenze (effetto dielettrico) che è costante su tutta la zona di Brillouin, noto come 'longitudinal-optical splitting'. Tuttavia, questo shift viene meno al centro della Brillouin zone nei materiali a bassa dimensionalità, con un andamento asintotico governato dalla dimensionalità; lineare nei sistemi 2D, mentre ancora oggetto di dibattito in 1D. Il lavoro presentato in questa tesi propone, per la prima volta, una risposta definitiva a questo dibattito, sviluppando la teoria dei fononi polari-ottici mancante per il caso 1D, un modello analitico e una validazione mediante simulazioni da principi primi resa possibile grazie alla nuova implementazione proposta. In particolare, il modello sviluppato consente di interpretare gli spettri Raman e infrarossi dei sistemi 1D; ciò rappresenta un'importante risorsa per la caratterizzazione dei materiali su scala nanometrica. Inoltre, lo stesso modello porta ad un ulteriore risultato analitico rilevante: l'accoppiamento elettrone-fonone di Fröhlich, cruciale per esempio nel campo del trasporto e nella polaritronica.

La seconda parte della tesi è dedicata ai materiali bidimensionali, noti anche come Flatlandia. In questo caso, l'obiettivo è quello di studiare il trasporto di carica, limitato da fononi, in semiconduttori drogati elettrostaticamente, con una duplice ambizione. Da un lato, ci concentriamo sulla ricerca computazionale di candidati ad alta mobilità, esplorando un ampio database di materiali. D'altro canto, ci focalizziamo su singoli materiali e lavoriamo per mettere a punto, o ingegnerizzare, le loro proprietà di trasporto. A tal proposito, in questa tesi discutiamo gli sforzi intrapresi in una collaborazione congiunta, teorica e sperimentale, che mira a progettare e ingegnerizzare canali 2D per transistor ad effetto di campo, applicando una deformazione permanente al materiale. Entrambi gli obiettivi sono perseguiti attraverso l'uso combinato della teoria delle perturbazioni applicata alla teoria della densità funzionale, tenendo conto esplicitamente della dimensionalità e del drogaggio, e della teoria del trasporto di Boltzmann, oltre l'approssimazione del tempo di rilassamento. Tutte le simulazioni sono state eseguite utilizzando l'infrastruttura informatica di AiiDA, una piattaforma Python, open-source, progettata per automatizzare e gestire le simulazioni e i dati risultanti, garantendo al tempo stesso la conservazione e la ricerca di tali dati.

Parole chiave: Nanostrutture, semiconduttori, screening, fononi, fononi polari ottici, caratterizzazione spettroscopica, Raman e infrared, interazioni elettrone-fonone, trasporto di carica, material discovery, strain engineering.

Contents

Acknowledgments	i
Abstract	iii
Sommario	v
List of Figures	ix
List of Tables	xiii
List of Acronyms	xv
1 Introduction	1
1.1 Organization of the thesis	3
2 Quantum picture of solids	5
2.1 Adiabatic approximation	5
2.1.1 Electronic structure	7
2.1.2 Lattice dynamics	9
2.1.3 Long-wavelength infrared-active phonons	12
2.1.4 Towards non-adiabatic effects: electron-phonon coupling	13
2.2 Charge transport and Boltzmann transport equation	15
2.3 Summary	17
3 DFT and DFPT for one-dimensional materials	19
3.1 Introduction	19
3.1.1 Statement of the problem: periodic vs open-boundary conditions	20
3.2 Implementation of 1D open-boundary conditions	23
3.2.1 1D Coulomb cutoff	23
3.2.2 Phonon interpolation and non-analytical corrections	29
3.3 Summary	30
4 Infrared-active phonons in one-dimensional materials, their coupling to electrons and spectroscopic signatures	33
4.1 State of the art and motivation	34
4.2 Analytical model	35

Contents

4.2.1 Solving the Poisson equation	38
4.3 Analytical results	44
4.4 Application to chains, wires and tubes	46
4.4.1 Polar-optical phonons	48
4.4.2 Electron-phonon interactions	51
4.5 Experimental relevance	53
4.6 Summary	56
5 Charge transport in 2D gated semiconductors	59
5.1 Motivation	60
5.2 Mobilities from first principles and from Fermiology	61
5.3 The high-throughput quest	63
5.3.1 Database, method and screening strategy	64
5.3.2 Results and discussion	67
5.4 Summary	73
6 Engineering mobility by permanent strain: the MoS₂ case	75
6.1 Introduction	75
6.2 Theoretical analysis	77
6.3 Summary	82
7 Conclusions	85
A Computational details	87
A.1 One-dimensional materials: model and first-principles calculations	87
A.2 Two-dimensional materials: mobility calculations	88
A.3 Theoretical methods and computational details for MoS ₂	89
Bibliography	91
Curriculum Vitae	105

List of Figures

2.1	Sketch of the scattering process between two particles: an electron in red and a phonon in blue. Before the collision they are respectively characterized by momentum and energy (\mathbf{k}, E) and $(\mathbf{q}, \hbar\omega)$, while after the collision by (\mathbf{k}', E') and $(\mathbf{q}', \hbar\omega')$	16
3.1	Sketch of the supercell construction for 1D systems and the effect of introducing the Coulomb cutoff.	22
3.2	In the first panel (a) we show the KS potential (inverted y axis) averaged along the wire, with (green) and without (red) the inclusion of the cutoff. In the second panel (b) we focus on the x-axis cross-section of the KS potential and we highlight the physical region. Also the electronic charge density is reported for reference. In the last panel (c) we zoom on the physical region and we plot besides the KS potential also the ionic and Hartree terms, always comparing each potential with and without the 1D cutoff.	26
4.1	Figure readapted from Ref. [1]. In the first panel, the Raman spectra of the NW stems (red) and the NNs (blue) are shown, obtained in the backscattering geometry at room temperature. On the right, a scanning electron microscopy (SEM) image of the regular array of NNs on top of NWs is reported.	35
4.2	Schematic representation of the 1D system within our model, i.e., filled cylinder of radius t . The dielectric properties (ϵ^m , Z^a) are summarized both inside and outside the cylinder. The equations to be solved in each region are reported. . .	36
4.3	Crystal structure of BN atomic-chain (a), armchair BN armchair nanotube (4,4) (b), and GaAs nanowire (c).	46
4.4	In the left panel (a) the radial charge density of, respectively, the BN atomic chain and one BN nanotube are shown. In the right panel (b) we report a schematic representation of how to extract the radius t from the charge density profile. The charge densities shown are obtained by averaging along the chain axis, and plotting in the radial direction. This is done for BN nanotubes of different sizes. A vertical dotted line, for each size, corresponds to the applied threshold. . . .	47

List of Figures

4.5	Phonon dispersion of BN atomic-chain, (4,4) nanotube, and wurtzite GaAs nanowire of 24 atoms including the hydrogen atoms saturating the surface dangling bonds. For each material, left panel compares 3D-PBC and 1D-OBC DFPT calculations, explicit for 1D (symbols) and interpolated for both (lines). Right panel shows the agreement of our model with 1D DFPT for the LO branch in the long-wavelength limit.	49
4.6	Size effects (mechanical and polar) on LO and TO modes for BN (6,6), (5,5) and (4,4) armchair nanotubes from 1D-DFPT. Right panel compares both modes. Left panel focuses on the polar shift for the LO branch by setting as common offset $\omega_0 = 0$. The sketch represents the mechanical evolution of tangential TO_T vs radial TO_R optical modes.	51
4.7	EPC matrix elements obtained from DFPT for LO phonons. We consider only intraband scattering within the valence or conduction band near Γ and Z . In red we report the results for the standard QE code, relying on 3D PBCS, and in green the ones obtained within 1D-DFPT. Last, we plot our analytical model on top of explicit DFPT results.	52
4.8	Evolution of the LO branch as a function of the radius of the BN chain (toy model) obtained by the model. The color bar indicates different Raman/infrared wavelengths in experiments.	54
4.9	Evolution of the LO branch in the long-wavelength limit for the two GaAs nanowires from Ref. [1] (10 and 100 nm in radius) obtained by the model. The comparison with experiments [1] is reported.	55
5.1	Some of the existing valley profiles, differentiated based on the number of valleys, their relative distance in energy (y-axis), their steepness, depth, and degree of anisotropy. These parameters provide crucial information for targeting specific applications.	63
5.2	Sketch of the computational protocol for the screening of high-mobility single-valley (SV) candidates.	64
5.3	Representation of the sampling grid used for transport calculation. The initial electronic states are represented in green, while the final ones in blue, and the phonons which enable these scattering processes in red.	66
5.4	Conductivity versus band gap (computed at DFT-PBE/PBEsol level) for the 2D materials selected by our screening. The electron-doped candidates are denoted by blue circles, while the hole-doped ones are shown in red. We also report for comparison the candidates previously selected within the original version of the database as discussed in Ref [2], grey symbols.	67

5.5	We report three plots for each of the selected candidates (C_2F_2 , SSb_2Te_2 , N_4 respectively). In order, we first show (left panel) the structure of the valley relevant for transport. Then, we report (central panel) the ‘velocity plot’ which shows for each \mathbf{k} state in the valley the energy from the band edge versus the norm of the velocity. The red-shaded region identifies the states within the transport energy window ($\partial f^0 / \partial \epsilon$). Last, we show (right panel) the ‘scattering plot’, showing the probability, given by the red color-map, for the initial state (black square) at the Fermi level to be scattered in any other final state within the valley.	69
5.6	Interpolated EPC in C_2F_2 . The color plot show the strength of the coupling by considering an initial electronic state (white star) and all the possible final states covering the full extent of the valley. Each plot represents a different phonon mode considered for the coupling. Phonon modes are ordered based on their energy associated to each transition: from left to right, from top to the bottom. Note that the color scale is different for each plot.	70
5.7	Interpolated EPC in SSb_2Te_2 . The color plot show the strength of the coupling by considering an initial electronic state (white star) and all the possible final states covering the full extent of the valley. Each plot represents a different phonon mode considered for the coupling. Phonon modes are ordered based on their energy associated to each transition: from left to right, from top to the bottom. Note that the color scale is different for each plot.	71
5.8	Interpolated EPC in N_4 . The color plot show the strength of the coupling by considering an initial electronic state (white star) and all the possible final states covering the full extent of the valley. Each plot represents a different phonon mode considered for the coupling. Phonon modes are ordered based on their energy associated to each transition: from left to right, from top to the bottom. Note that the color scale is different for each plot.	72
6.1	Crystal structure of MoS_2 , top (a and b panels) and lateral (c panel) views. Mo atoms are depicted in red and S atoms in blue.	76
6.2	Valley profile of MoS_2 unstrained in the first panel (blue), and after applying a tensile strain (red) in the second panel. The arrows indicate the relative energy distances between the K and Q valleys.	77
6.3	Electronic band structure and density of electronic states for the unstrained system (blue) and the 2% tensile strain (red). The zero of energy is set at the top of the valence band for each case: the Fermi level, accounting for doping and electronic temperature, is shown.	78
6.4	Phonon dispersion curves for unstrained MoS_2 (blue) in comparison with the strained case, 2% tensile uniform strain (red).	79

List of Figures

6.5	Electronic band structure and density of electronic states for the unstrained system (blue) and the 2% tensile strain (red). The zero of energy is set at the top of the valence band for each case: the Fermi level, accounting for doping and electronic temperature, is shown.	81
6.6	Variation of (a) valley energy separation, ΔE_{KQ} , and (b) room-temperature electron mobility as a function of the applied strain.	82
6.7	Interpolated EPC for three acoustic modes (i.e., LA, TA, ZA) in MoS ₂ . The first and third panels (a, c) refer to the unstrained material and differ in the initial electronic state (white star), with one being in the lowest K (a) or K' valley (c). The second and fourth panels (b, d) show the corresponding cases for the 2% strained system, with the Q valleys absent and lying outside the thermal layer. The color plot shows the strength of the coupling to all possible final states for each phonon mode (energetically ordered from left to right).	83
A.1	Phonon dispersion relations of (5,5) and (6,6) BN nanotubes, respectively. On the left panels, we compare the <i>ab-initio</i> results using DFPT in 3D (no cutoff between period copies and 3D long-ranged electrostatic dipole-dipole long-range interactions) and using 1D-DFPT (1D Coulomb cutoff and 1D long-range interactions). On the right panels, the interpolated and explicit DFPT results are shown for long-wavelength polar-optical phonons and compared with the analytical model.	89

List of Tables

5.1	<i>Ab-initio</i> properties computed in this work for three of the best candidates discussed (electron or hole doped). In order, we list the energy gap, the energy separation with respect to the next available valley, the highest carrier velocities at the Fermi level, the effective masses (x and y components, explicitly indicated when non isotropic), the maximum phonon frequency, the average computed electronic lifetime, conductivity and mobility.	73
A.1	<i>Ab-initio</i> zone-center values for ω_{LO} , ω_{TO} and the mechanical splitting $\Delta\omega_{\text{mech}}$, and the effective radius t . This is computed by averaging the electronic density profile in the out-of-wire directions and performing a gaussian fitting for the chain ($t=2\sigma$), while setting a meaningful threshold for the other systems. . . .	88

List of Acronyms

1D	One-dimensional
2D	Two-dimensional
3D	Three-dimensional
DFT	Density-functional theory
DFPT	Density-functional perturbation theory
BEC	Born effective charge
BZ	Brillouin zone
LO	Longitudinal optical
LR	Long range
TO	Transverse optical
ZO	Out-of-plane optical
EPC	Electron-phonon coupling
EPI	Electron-phonon interaction
BTE	Boltzmann transport equation
PBCs	Periodic-boundary conditions
QE	Quantum ESPRESSO
KS	Kohn-Sham
OBCs	Open-boundary conditions
IFCs	Interatomic Force Constants
NW	Nanowire
SO	Surface optical
NN	Nanoneedle
NNT	Nanotube
FET	Field-effect transistor
SCE	Short-channel effect

List of Acronyms

TMD	Transition-metal dichalcogenide
RTA	Relaxation-time approximation
CRTA	Constant relaxation-time approximation
EPA	Electron-phonon averaged
DOS	Density of states
PBE	Perdew-Burke
SV	Single-valley
SOC	Spin-orbit coupling
ICSD	Inorganic Crystal Structure Database
COD	Crystallography Open Database
MPDS	Materials Platform for Data Science
HT	High-throughput
ZA	Out-of-plane acoustic

1 Introduction

I would like to describe a field, in which little has been done, but in which an enormous amount can be done in principle...What I want to talk about is the problem of manipulating and controlling things on a small scale.

R. Feynman

Over the past few decades, the world has witnessed tremendous technological advances that have revolutionized and shaped many aspects of our lives and the society we live in; from the way we communicate, move, work and entertain ourselves, to our energy consumption and the way medicine can cure us. Providing more and more high-performing materials, as well as novel strategies and ideas to engineer and optimize their properties, has now become a central topic and certainly represents a major challenge for the 21st century. In this context, significant attention has been captivated by the fascinating world of low-dimensional materials, also known as nanostructures.

Low-dimensional structures are materials that possess two, one or zero-dimensional periodicity. The non-periodic dimension is small enough (at the nanoscale) for their physical properties to lay somewhere between those of individual atoms and the bulk material. This translates into unique and tunable properties, making them appealing for both fundamental science and technological applications. The potentials of low-dimensional materials for next-generation devices are virtually unlimited. Quoting the Nobel laureate Richard Feynman, ‘There’s plenty of room at the bottom’ meaning that there is vast potential for miniaturization in the field of science and technology [3]. Low-dimensional materials are in this sense a testament to Feynman’s vision, offering a unique opportunity to explore the frontier of the small and to design novel materials and devices with unparalleled properties. It is not just Feynman’s mind that has been stimulated by the possibilities these materials come to offer. Dimensionality is known since a long time to be a critical parameter in solid-state physics and nanomaterials inspired several pioneering works, such as the ones of Dresselhaus [4, 5, 6],

Hicks[7, 8], Novoselov and Geim [9], Kroto[10], Taniguchi[11] and Drexler[12], among many others. Even the European Commission has recognized the potential of these materials, as testified the Graphene flagship [13, 14, 15, 16, 17].

This wave of excitement and creativity can be better understood if contextualized at a time when the traditional semiconductor industry is facing challenges in further sustaining the exponential growth predicted by Moore's law. To date, the scaling down of traditional semiconductor technology has reached its physical limits, and low-dimensional materials hold the promise of overcoming these limitations. The major issue related to the miniaturization race is the amount of dissipated heat generated by the building-block of every electronic circuit: the field-effect transistor. Field-effect transistors rely on the capability of electrostatically inducing a significant change in the electronic properties of a target material, used as a channel, by modulating the density of mobile charges. This electrostatic control over the channel breaks down when reducing the size of the material to a critical length at the nanoscale. As a consequence the so-called short-channel effects arise, among which the main challenge is represented by waste heat. In this respect, low-dimensional materials allow for smaller critical lengths, thus expanding the horizons in terms of achievable miniaturization and further supporting the roadmap dictated by Moore's law. In particular, after the successful isolation of two-dimensional materials, such as graphene and transition metal dichalcogenides, a new class of field-effect transistor has emerged, offering promising electrical and mechanical properties for practical applications [16, 18, 19, 20, 21]. Similar efforts have been put forward by exploiting one-dimensional materials such as nanotubes [22, 23].

One-dimensional materials have have historically received less attention compared to bulk three-dimensional and two-dimensional materials. This is primarily due to the technical challenges in their synthesis and characterization. However, this is changing rapidly as the field continues to evolve. Advances in synthesis techniques, such as chemical vapor deposition and molecular-beam epitaxy, have made it possible to produce high-quality one-dimensional materials with controlled structures and compositions [1]. Additionally, the development of new characterization techniques has enabled the study of these materials in greater detail[24].

However, to fully harness the potential of low-dimensional systems, it is highly desirable to be able to predict and simulate their physics from first principles. For this, density-functional perturbation theory represents a powerful tool that has been shown to accurately predict vibrational and electron-phonon properties, which are at the core of this thesis [25, 26, 27, 28, 25, 29]. This modeling capability would allow us to support and complement experiments, providing deeper insight into the underlying microscopic mechanisms that are essential for the design and fabrication of new materials and devices. In this quest, machine learning and automated materials discovery certainly play a crucial role, enabling the search through large databases of materials and the identification of those with desired properties.

The work presented in this thesis aims to deepen the current understanding of the impact of dimensionality on materials properties. In the following chapters, we focus on phonons,

electron-phonon couplings, and charge transport in one-dimensional and two-dimensional systems. To investigate these topics, we employ analytical and theoretical modeling, as well as first-principles simulations and state-of-the-art automation techniques. Our ambition for one-dimensional materials is to bridge the existing gap in methodological and theoretical *ab-initio* understanding. For two-dimensional systems, which are currently more widely researched, we aim to provide a foundation for further exploration. The results presented in this work represent a starting point for future research, and we hope they will foster and inspire both the theoretical and experimental communities to continue pushing the boundaries of knowledge in the field of nanostructure.

1.1 Organization of the thesis

The thesis is organized as follows.

In **Chapter 2** we introduce the main concepts at the center of this thesis. Starting from the general atomistic picture, we briefly illustrate the exact many-body problem for crystals. After introducing a useful hierarchy of approximations, we discuss, within the adiabatic approximation, electrons and phonons. Namely, we focus on polar-optical phonons, anticipating the critical dimensionality signature on their dispersion relations. Eventually, we reintroduce in our picture the effect of electron-phonon interactions. This is the starting point for developing the topic of charge transport and Boltzmann transport theory. All this is discussed keeping the mathematical formalism to a minimum and framing the whole discussion in terms of density-functional and density-functional perturbation theory.

In **Chapter 3** we present a novel implementation, based on density-functional and density-functional perturbation theory, to simulate ground-state and linear-response properties of one-dimensional systems from first principles. The aim is to curate the spurious interactions due to the periodic images which are present in simulations relying on periodic-boundary conditions. This is achieved by implementing a modified version of the Coulomb cutoff technique in our *ab-initio* code of reference, Quantum ESPRESSO. Our implementation eventually unlocks the possibility to compute energies, forces, stresses, phonons and electron-phonon properties for any kind of system periodic only along one dimension.

In **Chapter 4** we focus on polar-optical, infrared-active, phonons and we develop the missing theory for 1D systems: nanowires, nanotubes, and atomic and polymeric chains. We detail the derivation of an electrostatic model which describes the interplay between the phonon-induced polarization and electronic screening. From such model, we obtain a fully analytical expression for the long-wavelength dispersion relations of polar-optical phonons as a function of phonon momenta and system radius. In addition, the same model leads to another key analytical result, the Fröhlich electron-phonon coupling, fundamental for transport applications. We validate and complement these analytical results by comparison with first-principles calculations thanks to the implementation presented in the previous chapter, thus proving its effectiveness in restoring the true one-dimensional response. Finally, we show how the

Chapter 1. Introduction

dielectric properties and the radius of the one-dimensional materials can be linked, by the present model, to Raman and infrared shifts, opening novel characterization avenues at the nanoscale.

In **Chapter 5** we shift our attention to two-dimensional materials. Namely, we focus on phonon-limited charge transport in gated semiconductors and on the quest for high-mobility candidates. To this aim, we improve and extend a previous study by exploring the expanded version of a curated portfolio of 2D structures. This gives us 1205 novel easily exfoliable candidates from which we start our quest. We combine density-functional perturbation theory with Boltzmann transport beyond the relaxation-time approximation, with special attention to the role of dimensionality and doping in driving electron-phonon interactions. We discuss the most interesting candidates and the entire discovery workflow powered by the AiiDA materials informatics infrastructure.

In **Chapter 6** we present a joint experimental and theoretical effort aiming at the design and engineering of MoS₂ channels for field-effect transistors. The basic idea is to induce a permanent strain in the material by deposition on a corrugated substrate and exploit such strain to enhance carrier mobilities. We introduce in this chapter the preliminary theoretical results and discuss the future perspectives.

2 Quantum picture of solids

In this opening chapter we are interested in recalling the main concepts useful to discuss two key actors in condensed matter physics and in this thesis: electrons and phonons. In the following we will focus on the big picture, highlighting the central physical concepts while keeping the mathematical formalism to a minimum. For a more in-depth discussion, we refer to famous texts such as Refs. [30, 31, 32, 33, 34]. Namely, special attention will be devoted to the role of materials dimensionality in shaping electrons and phonons behaviors as well as the ‘dynamics’ of their interaction, which is indeed central for transport applications. The starting point of the discussion is the well-known atomistic picture, i.e., materials are made by a large number of elementary constituents, that is atoms. Here we are interested in crystalline solids in which atoms, bound together by electrostatic interactions, are arranged in a ordered fashion thus relying on a simple yet powerful property: periodicity. The resulting quantum-mechanical problem is cumbersome and too complex to be solved by any analytical or numerical tool at our disposal. For this reason the standard approach is to rely on a hierarchy of approximations. In this chapter we will make use of the so-called *frozen-core approximation* and magnetic and relativistic effects will be neglected unless specified otherwise. Finally the *adiabatic approximation* will allow us to recast this complex problem in a solvable form in such a way to compute all the relevant physical properties of a variety of systems periodic in three, two or one dimensions. This will pave the way to the concepts of electronic structure and lattice dynamics, i.e., phonons, in both bulk materials and nanostructures. The need for understanding the interaction between these two quasi-particles will finally push our storytelling further in the attempt of reintroducing in our picture the so-called non-adiabatic effects via perturbation theory.

2.1 Adiabatic approximation

Let us start by constructing our atomistic model for a generic crystal, a collection of interacting nuclei and electrons. Thanks to the frozen-core approximation, we decompose atoms in ions, that is nuclei plus core electrons, and valence electrons. The main advantage of such an approximation is a dramatic reduction of the number of electronic degrees of freedom

explicitly appearing in our problem. Besides, this assumption is well-motivated by the fact that, to a large extent, the chemical properties of each atom, and thus most of materials properties, are ruled by valence electrons.

At this point, we can mathematically formulate the full quantum mechanical problem describing the physics of our crystal. We exploit the two aforementioned approximations (i.e., frozen-core and no magnetic and relativistic effects) and the corresponding Schrödinger equation reads as

$$\underbrace{\left[-\frac{\hbar^2}{2} \sum_a \frac{\nabla_a^2}{M_a} - \frac{\hbar^2}{2m_e} \sum_i \nabla_i^2 + V_{ne}(\mathbf{r}, \mathbf{R}) + V_{nn}(\mathbf{R}) + V_{ee}(\mathbf{r}) \right]}_{H_{\text{tot}}} \Phi(\mathbf{r}, \mathbf{R}) = E^{\text{tot}} \Phi(\mathbf{r}, \mathbf{R}), \quad (2.1)$$

where \mathbf{r} and \mathbf{R} represent, respectively, the full set of electronic and ionic coordinates. On the left-hand side of Eq. 2.1, the total Hamiltonian of the coupled nuclear-electronic problem is composed by the kinetic energy of each ion a and each electron i , and the Coulombic energy interaction between the constituents (i.e., ions and electrons V_{ne} , ion-ion V_{nn} and electron-electron V_{ee}). Clearly our treatment implies that ions and electrons interact only via Coulomb coupling. This Hamiltonian, despite the approximations we made, still leads to an unsolvable problem for our means. For this reason, we introduce a third and crucial simplification: the adiabatic approximation. This consists in noticing that ions, being much more massive than electrons (i.e., $M_a/m_e \approx 10^3 - 10^5$), exhibit a much slower dynamics, thus hinting to the possibility of decoupling nuclear (slow) and electronic (fast) motions. In essence, since the electrons move much faster, they adapt very rapidly to any changes in nuclear geometry and thus are commonly said to ‘follow adiabatically the motion of the nuclei’. Such an assumption is supported by spectroscopic measurements showing that the energy scales of these two key players are indeed quite different: photon emission/absorption mediated by atomic oscillations happens in the infrared region, while electronic transitions are usually in the visible and ultraviolet regions of the electromagnetic spectrum. In practice, the key idea is to decouple the electronic and vibrational degrees of freedom, thus writing the total eigenfunction Φ as the product of the total ionic χ_n and electronic Ψ_e wavefunctions:

$$\Phi(\mathbf{r}, \mathbf{R}) = \chi_n(\mathbf{R}) \Psi_e^{\mathbf{R}}(\mathbf{r}). \quad (2.2)$$

This implies that there is no exchange of energy between the electrons and the lattice, from which the term ‘adiabatic’. Thus, our original problem can be recast in a purely electronic one (depending only parametrically and non analytically on the atomic positions), whose solution is then needed to solve the ionic/nuclear one. In other words, we can first solve the eigenvalue equation for the electronic problem

$$\left[-\frac{\hbar^2}{2m_e} \sum_i \nabla_i^2 + V_{ne}(\mathbf{r}, \mathbf{R}) + V_{ee}(\mathbf{r}) \right] \Psi_e^{\mathbf{R}}(\mathbf{r}) = E_e^{\mathbf{R}} \Psi_e^{\mathbf{R}}(\mathbf{r}), \quad (2.3)$$

where $\Psi_e^{\mathbf{R}}(\mathbf{r})$ and $E_e^{\mathbf{R}}$ are the wavefunctions and energies for the electrons subsystem, corre-

sponding to the clamped-ion configuration parameterized by \mathbf{R} (i.e., *fixed lattice approximation*). Once the electronic energies E_e (labeled accordingly to all the possible electronic states, e.g., ground-state, first excited...) are computed for a given ion configuration $\{\mathbf{R}\}$, the nuclear energies can be calculated as if the ions move in the associated adiabatic potential energy surface. This is given by the calculated electronic energy and the restored ion-ion interaction term:

$$\left[-\frac{\hbar^2}{2} \sum_a \frac{1}{M_a} \nabla_a^2 + \underbrace{V_{nn}(\mathbf{R}) + E_e^{\mathbf{R}}}_{U(\mathbf{R})} \right] \chi_n(\mathbf{R}) = E^{\text{tot}} \chi_n(\mathbf{R}), \quad (2.4)$$

where $U(\mathbf{R})$ is often referred to as the Born-Oppenheimer energy surface. As a result, a vast category of problems in solid-state physics traces back to the solution of these two constitutive equations. Naturally, there exist a wide range of phenomena which to be explained require to go beyond this adiabatic approximation; those are generically termed ‘non-adiabatic phenomena’. These effects are usually re-introduced in our picture by treating them as perturbations, and as such still within the adiabatic framework, if the induced potential variation is sufficiently small. Thus, reminding that phonons are the quanta of ionic vibrations, electron-phonon interactions appear naturally as the first order correction to the adiabatic approximation here presented. We will come back to this central topic in the following.

2.1.1 Electronic structure

To solve the electronic many-body problem formulated in the above section, different strategies have been developed over the last sixty years and can be adopted nowadays thanks to the acquired computational capabilities. Most of the methods which are routinely used belong to the so-called ‘from first-principles’, or *ab-initio* family. Each of them has its own advantages and drawbacks. The key difference is the quantity on which they rely to describe the system: the electronic density, the many-body wavefunction or the Green’s function. Here, we focus on the first approach which is commonly known as density-functional theory (DFT), based on the famous Hohenberg-Kohn theorem (1964) and the work of Kohn and Sham (1965) [35, 36]. This approach consists in a reformulation of the many-body problem in Eq. 2.1 by remapping it into a simpler but equivalent, and in principle exact, single-particle problem in which the protagonist is the ground-state electronic charge density. Once this density is known, all the relevant materials properties can be obtained as long as related to physical observables which can be written as functionals of this density –this includes ground-state properties such as energy, force and stress tensors, and many others. The advantage with respect to the other two mentioned approaches is clear: a dramatic reduction of the degree of freedoms since the electronic charge density only depends on the spatial coordinates in the three dimensions of space. On the other hand, the main disadvantage consists in the hierarchy of approximations needed to rewrite the energy of the system as a functional of the charge density [33, 37].

Thanks to the DFT remapping, we are now working in a single-particle framework. Thus, in the rest of this thesis we will rely on the band theory to describe the electronic structure of materials. In particular, the electron-ion and electron-electron interactions are now described

by an effective potential sharing the periodicity of the underlying crystal lattice. This is equivalent to say that each electron independently moves under the action of a local crystal field potential describing its embedding into a crystalline environment constituted by the ions and the remaining electrons. However, we remark that we are not treating electrons as non-interacting particles, we are just remapping our problem in a way that the potential chosen in the new picture include all the relevant features of electron-electron interactions. While there exist different ways to describing such potential, one of the most effective is by the self-consistent-field method. Since DFT literature is mostly written in atomic units, instead of the international system, we compactly write the many-body problem of the previous section, Eq. 2.1, within the DFT framework:

$$\left[-\frac{\nabla^2}{2} + V_H([\rho], \mathbf{r}) + V_{xc}([\rho], \mathbf{r}) + V_{\text{ext}}(\mathbf{r}) \right] \phi_i(\mathbf{r}) = \epsilon_i \phi_i(\mathbf{r}), \quad (2.5)$$

where one makes use of the distinction between electron-ion interactions V_{ext} (external potential term) and electron-electron interactions V_H and V_{xc} (Hartree and exchange-correlation terms, respectively). This distinction emphasizes that the ions are somehow external to the electron system, and indeed their charges are the only information needed to solve our problem, thus justifying the name *ab-initio* or first-principles methods. Concerning the purely electronic part of the potential, the Hartree term clearly corresponds to the Coulombic pairwise interaction between electrons, while the exchange-correlation potential has the purpose of reintroducing the many-body effects. There exist many approximated strategies to write this terms, but its true form is in principle unknown. This latter term is the bottleneck in our problem and the limiting aspect in most of DFT based calculations.

Up to this point, our discussion implicitly refers to a generic three-dimensional (3D) crystal, where all the potentials and wavefunctions are considered to be periodic in the three spatial dimensions, and thus \mathbf{r} and \mathbf{R} are both vectors living in the 3D space. When we lower the dimensionality of our systems –that is, we consider one-dimensional (1D) or two-dimensional (2D) crystals– we are basically reducing the possible configurations that electrons can assume, i.e., their phase-space. As a consequence of this simple observation, periodicity changes the analytical dependence of the wavefunctions, and similarly of the potentials, on the spatial coordinates:

$$\mathbf{r} = \begin{cases} (x, y, z) & 3\text{D} \\ (\mathbf{r}_p, z) & 2\text{D} \\ (\mathbf{r}_\perp, z) & 1\text{D} \end{cases} \rightarrow \mathbf{k} = \begin{cases} (k_x, k_y, k_z) & 3\text{D} \\ (k_x, k_y, 0) & 2\text{D} \\ (0, 0, k_z) & 1\text{D} \end{cases} \rightarrow \psi_{\mathbf{k},s}(\mathbf{r}) = \begin{cases} w_{\mathbf{k},s}(\mathbf{r}) e^{i\mathbf{k}\cdot\mathbf{r}} & 3\text{D} \\ w_{\mathbf{k},s}(\mathbf{r}_p, z) e^{i\mathbf{k}_p\cdot\mathbf{r}_p} & 2\text{D} \\ w_{\mathbf{k},s}(\mathbf{r}_\perp, z) e^{ik_z z} & 1\text{D} \end{cases}$$

where w is the periodic part of the Bloch wavefunction, and p indicates in-plane vectors and vector components in 2D, while \perp refers to the transversal ones in 1D. Another critical aspect introduced by dimensionality, which is a consequence of the previous point, pertains to the distinct nature of electronic screening. Within our density functional theory (DFT)

framework, screening is incorporated via the Hartree and exchange-correlation terms. These terms generally describe the electrons' ability to rearrange themselves in order to counteract an external electric field or perturbation to the system. As a result, the effective potential experienced by each electronic charge is the sum of the perturbing potential and the potential generated in response, leading to a weaker potential relative to the original perturbation. The impact of dimensionality on screening is well-documented and can have significant implications. Mathematically we can understand this by simply considering the Fourier transform of the Coulomb interaction for an n -dimensional system (with n being 1,2,3) [38]:

$$v_c(|\mathbf{q}|) = \begin{cases} \frac{4\pi e^2}{|\mathbf{q}^2|} & 3\text{D} \\ \frac{2\pi e^2}{|\mathbf{q}|} & 2\text{D} \\ -e^2 e^{q^2 a^2} \text{Ei}(-|\mathbf{q}|^2 a^2) & 1\text{D} \end{cases} \quad (2.6)$$

where $\text{Ei}(x)$ is the exponential integral function and a is a short-distance cutoff introduced to avoid the non-integrable 1D divergence at $\mathbf{r} = 0$. Thus, the reduced phase space manifests in different ways and in different properties, for which the screening is key. Another related aspect, in low-dimensional systems, is the sensitivity to the external environment and stimulations (such as light, or the presence of heterostructures and/or substrates). In short, the key message is that one can exploit this sensitivity, combined with the peculiarity of the materials response, to tune relevant properties for target applications. To this aim, it is desirable to reach an accurate understanding of how dimensionality shapes materials properties. This concept will come back several times in the following sections and chapters.

2.1.2 Lattice dynamics

The electronic problem described in Section 2.1.1 is solvable for any set of clamped ionic positions $\{\mathbf{R}\}$ within the DFT framework, as in this thesis, or by means of other approaches (see Sec. 2.1.1). However, the static lattice picture is destined to fail since even at zero temperature the ions have a non-vanishing square momentum associated to their finite mass. This is supported by a number of experimental evidences (e.g., specific heat, thermal expansion, melting, and transport properties in general including superconductivity and interaction with radiation). From this stems the need of studying, besides purely electronic structure, the lattice dynamics of crystals in order to reach a comprehensive understanding of the physical properties of materials. Once the energy of the electronic system is known, this translates into the potential energy for the ions and thus their dynamics can be derived leading to the concept of phonons, their dispersion relations and vibrational properties. In a nutshell, within the adiabatic approximation of Born-Oppenheimer the ions move in a potential energy surface, $U(\mathbf{R})$, determined by the electronic energy of the system calculated at fixed ions. In this picture the ions oscillate around their lattice equilibrium positions $\{\mathbf{R}_0\}$, while the electrons are assumed to be in the ground state for each nuclear configuration. In other words, we are interested in small displacements around the equilibrium configuration of the ground

adiabatic energy surface (supposed to be non-degenerate). These ionic oscillations can be described in terms of instantaneous positions:

$$\mathbf{R}_l(t) = \mathbf{R}_l^0 + \mathbf{u}_l(t) \quad (2.7)$$

where \mathbf{R}_l^0 denotes the equilibrium or rest position of the l^{th} ion and \mathbf{u}_l is the ionic displacement with respect to this initial configuration.¹ If the displacements \mathbf{u}_l are small compared to the lattice spacing, one can expand the total energy in a Taylor series with respect to the displacements and truncate the expansion after the first non-vanishing term, i.e., second order expansion:

$$U(\mathbf{R}_l^0 + \mathbf{u}_l) = U(\mathbf{R}_l^0) + \sum_{l\alpha} \frac{\partial U}{\partial \mathbf{u}_{l\alpha}} \mathbf{u}_{l\alpha} + \frac{1}{2} \sum_{l\alpha, l'\beta} \frac{\partial^2 U}{\partial \mathbf{u}_{l\alpha} \partial \mathbf{u}_{l'\beta}} \mathbf{u}_{l\alpha} \mathbf{u}_{l'\beta}, \quad (2.8)$$

where the Greek subscripts indicate the Cartesian components, while the Latin ones here label the ions (i.e., Bravais lattice and basis). The first-order term is zero, corresponding to the forces acting on the ions at equilibrium:

$$\left. \frac{\partial U}{\partial \mathbf{u}_l} \right|_0 = 0; \quad (2.9)$$

this is by definition the rest condition for the crystal. Eventually, we are left with an Hamiltonian which is quadratic in the ionic displacements:

$$H = \sum_l \frac{p_l^2}{2M_l} + \frac{1}{2} \sum_{l\alpha, l'\beta} \frac{\partial^2 U}{\partial \mathbf{u}_{l\alpha} \partial \mathbf{u}_{l'\beta}} \mathbf{u}_{l\alpha} \mathbf{u}_{l'\beta}. \quad (2.10)$$

This is called *harmonic approximation* since the nuclear problem is now equivalent to the classical one of a set of identical harmonic oscillators whose force constants are given by the derivatives of the potential energy. This approximation has been proven to work very well to predict the vibrational properties of the majority of crystalline solids. Under such assumption, the solution to the nuclear problem becomes analytic, showing that the motion of nuclei in crystals is quantized and the quanta of vibrations are called phonons.

The condition of vanishing forces acting on each atom, Eq. 2.9, provides the equilibrium geometry of the crystal. However, the vibrational frequencies are obtained by solving the equations of motion associated to the harmonic Hamiltonian in Eq. 2.10. Thus, we get to the final secular equation in reciprocal space:

$$\det \left| D_{ll'}^{\alpha\beta}(\mathbf{q}) - \omega^2(\mathbf{q}) \right| = 0 \quad (2.11)$$

¹Note that a rigorous notation would require to write the rest position of the atom within the crystal as $\mathbf{R}^0 = \mathbf{R}_l^0 + \mathbf{R}_b^0$, where l indicates the cell, while b the position of the atom within the basis in the cell.

where $D_{ll'}^{\alpha\beta}(\mathbf{q})$ is called dynamical matrix and corresponds to the Fourier transform of the Hessian (also termed force-constants matrix) of the Born-Oppenheimer energy scaled by the nuclear masses $\frac{1}{\sqrt{M_l M_{l'}}} \frac{\partial^2 U}{\partial \mathbf{R}_l \partial \mathbf{R}_{l'}}$, and ω are the phonon frequencies. Within the DFT framework, on which this thesis relies, the Born-Oppenheimer energy surface driving the lattice dynamics can be computed by solving the Kohn-Sham problem in Eq. 2.5, but then, in order to compute the first and second derivatives of the energy, we need to introduce density-functional perturbation theory (DFPT). In practice, to solve the nuclear problem and obtain the vibrational frequencies of a given material, DFPT exploits the well-known Hellmann-Feynman theorem and the problem is reduced to compute the density of the ground-state electronic system $n^{|\mathbf{R}|}(\mathbf{r})$ and its linear response to a distortion in the lattice geometry $\partial n^{|\mathbf{R}|}(\mathbf{r})/\mathbf{R}_l$. As for DFT, we refer to dedicated textbooks and reviews for a more detailed explanation [26].

Let us close this section by giving a more intuitive picture about phonons and some useful comments about their dimensionality signatures. Lattice vibrations are described by waves corresponding to the displacements of each atom with respect to its equilibrium position. As for electronic wavefunctions, phonons are labeled by two quantum numbers: the phonon (or crystal) momentum \mathbf{q} in the Brillouin zone (BZ), due to the periodicity of the crystal, and a band index ν labeling the different branches, in total $3 \times N_{\text{atoms}}$. It follows that phonons are also represented, similarly to electrons, in terms of dispersion relation curves, or phonon bands, in reciprocal space. By focusing on the long-wavelength limit (i.e., $\mathbf{q} \rightarrow 0$), it is possible to classify phonons based on the following two criteria: the propagation direction and their acoustic or optical character. As regards the direction, for a fixed \mathbf{q} one can always specify one longitudinal and two transverse modes, that is directions of motion for the atoms. Then, if the unit cell contains at least two atoms, it is possible to distinguish between acoustic and optical phonons depending if the atoms move in or out-of phase with respect to each other. In low-dimensional materials, 2D and 1D, in-plane (chain) and out-of-plane (chain) modes are intrinsically different. This is due to the fact that atomic displacements in the vacuum direction are necessarily ‘mechanically’ (i.e., due to symmetry and dimensionality considerations) dissimilar. Naively speaking, the effective springs bringing the atoms back to their equilibrium positions are characterized by smaller force constants in the vacuum direction with respect to the in-plane or in-chain direction, and this affects the dispersion relations. This distinction between longitudinal and transverse modes is crucial both in the case of acoustic phonons and optical phonons. In the former case, we name those out-of-plane or chain acoustic modes as ‘flexural’; these are known to exhibit a dispersion relation which is not linear but quadratic at small momenta $\hbar\omega_{\mathbf{q},\nu} \propto |\mathbf{q}|^2$. As a consequence, flexural phonons are expected to dominate the physics of low-dimensional systems at low energy and small momenta. This quadratic behavior has been at the center of a long-standing debate concerning the stability of free standing 2D materials at finite temperature and the possible appearance of ripples. At variance, if the material is deposited on a substrate, such as in field-effect transistors, the energy of the flexural mode will tend to a finite constant value at Γ . Similar considerations and question marks should be in principle valid for 1D systems as well. As far as optical modes are concerned, dimensionality gifts us with another

crucial fingerprint, which is even more remarkable in that it is specific of the dimensionality considered, and not simply related to the presence of vacuum as it was for the acoustic phonons. The understanding of such signature is crucial and will be at the center of a large part of this thesis. Thus, this topic deserves a separate section.

2.1.3 Long-wavelength infrared-active phonons

Let us focus the discussion on a specific kind of lattice vibrations, the so-called polar-optical, infrared-active phonons, and namely their long-wavelength behavior. In any semiconductor and/or insulator with different atomic sublattices one can associate to atomic bonding some ionic/polar character (e.g., NaCl, GaAs, BN). Such bonding character, in this context, is quantified by means of the Born effective charges (BECs) concept [39, 39, 26]. These effective charges are different from the nominal ionic ones; they are a dynamical concept, related to the density response to an external perturbation, such as phonons, and are indeed defined as tensors rather than scalars. The formal definition for the BEC tensor components of an atom a is [26]:

$$Z_{\alpha,\beta}^a = \frac{1}{e} \frac{\partial F_\alpha^a}{\partial E_\beta} = \frac{\Omega}{e} \frac{\partial P_\alpha}{\partial u_\beta^a} = \int r_\beta \frac{\partial \rho}{\partial u_\beta^a} d\mathbf{r}, \quad (2.12)$$

where Ω is the volume of the unit cell. Thus, we can interpret these charges as proportional to the variation of the force, \mathbf{F} , acting on the ion along a direction α as a consequence of an electric field, \mathbf{E} , along β , or, equivalently, as the change in the α^{th} component of the electronic polarization, \mathbf{P} , given by the atomic displacement along β . These charges are thus commonly associated to the polarity of a materials.² The intuitive consequence of this polar character is that long-wavelength optical phonons make the atoms behave as oscillating dipoles –with charge given by the BECs– interacting with each other. Thus, as soon as the atoms in the lattice have non-vanishing BECs, optical phonons can generate a polarization density and couple with electric fields. As a consequence, these modes are termed polar and are infrared active. In addition, for longitudinal atomic displacement patterns, and in particular for purely longitudinal optical (LO) modes³, a long-range (LR) electric field is generated that becomes macroscopic in the long-wavelength limit. Since we are dealing with semiconductors/insulators rather than metallic systems, the associated LR electrostatic interactions are only partially screened by electrons and thus the macroscopic electric field is ultimately felt by the nuclei as an additional restoring force; this dramatically affects the dispersion of the LO modes. In particular, creating an additional electric energy density in the material is more costly and thus the frequency of the LO mode is generally blue-shifted. In 3D bulk materials the energy shift of a LO mode can be analytically described thanks to the seminal work from Cochran and Cowley [40]:

²Here by ‘polar’ we do not assume that the material has net electronic macroscopic polarization per se, we instead refer to the polarization potentially induced by the perturbation.

³These are labeled as such in the long-wavelength limit of $\mathbf{q} \rightarrow 0$.

$$\omega_{\text{LO}}^{\text{3D}}(\mathbf{q} \rightarrow 0) = \sqrt{\omega_0^2 + \frac{4\pi e^2}{\epsilon^\infty \Omega} \left(\sum_a \frac{Z_a \cdot \mathbf{e}_{\text{LO}}^a}{\sqrt{M_a}} \right)^2}, \quad (2.13)$$

where ϵ^∞ is the macroscopic dielectric tensor, \mathbf{e}_{LO}^a refers to LO phonon eigenvectors, and ω_0 is the LO frequency for $\mathbf{q} \rightarrow 0$ in the absence of polar or dielectric, as will be termed in the following, effects. The dielectric contribution to the dispersion of the LO mode is clearly constant around the BZ center (included Γ) as a function of the norm of the momentum, while its strength is tuned by the screened effective charges. Moreover, the size of the shift depends on the direction in reciprocal space along which \mathbf{q} is tending to Γ . This creates a discontinuity in terms of dispersion relation for the LO modes. We anticipate here that while this effect is modulated in strength by the dielectric properties of the material, its overall dependency on phonon momenta and size is ruled solely by dimensionality.

For 2D materials, the analogous of the 3D expression in Eq. 2.13 has been recently derived, in 2017, by T. Sohler and coauthors in Ref. [41]. This work highlights a strong momentum-dependence of the dielectric shift, characterized by a linear asymptotic behavior and vanishing at Γ exactly. This has led to the name of ‘breakdown of LO-TO splitting’ as opposed to the well-known 3D splitting. A similar breakdown can be expected in 1D systems as well; nonetheless, the analytical proof and the details of its actual asymptotic behavior remained, until now, an open question (see Chapter 4).

Note that the dielectric contribution to the dispersion of the LO mode is often described in terms of a deviation from the transverse optical (TO) mode: LO-TO splitting. This is because in many materials (e.g., with cubic/tetragonal symmetries or planar hexagonal) LO and TO modes would be indeed degenerate in the absence of dielectric effects [40, 42, 26, 39, 26, 27, 25]. However, the lifting of these degeneracies ultimately depends on the symmetries and the dimensionality of the crystal. In 3D, with 3 equivalent directions at most, optical modes are up to triply degenerate at the zone center (based on group theory considerations [43]). In 2D, these modes are up to doubly degenerate, while a splitting with respect to the out-of-plane optical (ZO) modes always persists since in- and out-of-plane displacements are nonequivalent, as explained in the previous section. In 1D, the longitudinal direction is clearly different from the other two, which are instead possibly degenerate with each other. Thus, there is no degeneracy to recover, even if the polar energy shift vanishes. Accordingly, in the following we will refer to this phenomenon as dielectric or polar shift rather than LO-TO splitting.

2.1.4 Towards non-adiabatic effects: electron-phonon coupling

So far we considered the electronic and nuclear problem as decoupled (adiabatic approximation). First, we assumed that the electrons move in the static periodic potential created by the ions fixed at their equilibrium positions. In this picture electrons are represented by Bloch states and can move in the ionic potential without disturbance. Then, we solved the problem

for the ions given a certain electronic configuration. However this is not the whole story since valence electrons and phonons influence each other in a more complex way, and this mutual influence is relevant, and sometimes even dominant, for a variety of physical phenomena in solids. In this extended picture, it comes natural to think of phonons as perturbations creating a charge imbalance with respect to the unperturbed ionic potential. This ultimately translates into the possibility for electrons to jump from one electronic state to another, that is a scattering event (sketched in Fig. 2.1). Such scattering events are characterized by the exchange of energy and momentum between phonons and electrons, thus breaking indeed the adiabatic assumption. To address this coupling, one in principle needs to go beyond the adiabatic approximation exploited in the previous section and expand the total wavefunction in the form:

$$\Phi_m(\mathbf{r}, \mathbf{R}) = \sum_n \chi_{mn}(\mathbf{R}) \Psi_n^{(\mathbf{R})}(\mathbf{r}), \quad (2.14)$$

with n now labeling the electronic eigenstates. As a consequence, the eigenvalue problem for the ionic/nuclear subsystem becomes:

$$\underbrace{\left[-\frac{\hbar^2}{2} \sum_a \frac{1}{M_a} \nabla_a^2 + V_{\text{nn}}(\mathbf{R}) + E_n^{\mathbf{R}} \right]}_{H_{\text{adiab.}}} \chi_{mn}(\mathbf{R}) + \underbrace{\sum_{n'} \Delta H_{nn'}}_{H_{\text{el-ph}}} \chi_{mn'}(\mathbf{R}) = E_m^{\text{tot}} \chi_{mn}(\mathbf{R}), \quad (2.15)$$

where the first term in parenthesis is indeed the same nuclear Hamiltonian we obtained within the adiabatic approximation, while the second term is the correction which accounts for the coupling between phonons and electrons. ΔH can be actually decomposed in two contributions, $\Delta H'$ and $\Delta H''$, respectively proportional to the first and second derivative of the electronic wavefunctions with respect to the ionic displacements, thus reintegrating in our picture all the possible electronic excitations due to ionic motion. It is common strategy to truncate the correction to the Hamiltonian after the first term, which is considered to be the dominant in most of the cases.

In practice, if we assume the electron-phonon coupling to be weak (i.e., no electronic features at energies similar to phonons) we can treat it in a perturbative way, that is by linear response within DFPT:

$$H_{\text{adiab.}} \rightarrow H_{\text{non-adiab.}} = H_{\text{adiab.}} + H_{\text{el-ph}}. \quad (2.16)$$

To go beyond this level of approximation, one can rely on diagrammatic and non-perturbative approaches. In our framework, the strength of the coupling is given by the electron-phonon coupling (EPCs) matrix elements $g_{\mathbf{k}, \mathbf{k}+\mathbf{q}, \nu}$. These are defined as the transition probabilities for any given electron (Kohn-Sham state) to be scattered by a certain phonon into each of the possible final states as a consequence of the induced change in the self-consistent potential experienced by electrons. The larger the EPCs, the stronger the coupling, and the more relevant

are expected to be the non-adiabatic correction to the crystal Hamiltonian:

$$H_{\text{el-ph}} \propto g_{\mathbf{k}, \mathbf{k}+\mathbf{q}, \nu} = \sum_{a, \beta} \mathbf{e}_{\mathbf{q}, \nu}^{a, \beta} \sqrt{\frac{\hbar}{2M_a \omega_{\mathbf{q}, \nu}}} \langle \mathbf{k} + \mathbf{q} | \frac{\partial V_{\text{KS}}(\mathbf{r})}{\partial \mathbf{u}_{a, \beta}(\mathbf{q})} | \mathbf{k} \rangle, \quad (2.17)$$

where we are summing over all the phonon displacements of atom a along the direction β . In actual DFPT calculations, the potential $\partial V_{\text{KS}}(\mathbf{r})$ is calculated by explicitly taking into account the rearrangement of the electronic charge following a small ionic displacement. As a result, the EPC matrix elements computed are screened via the induced part of the effective KS perturbation (Hartree and exchange correlation).

Electron-phonon interactions (EPIs) are ubiquitous in condensed-matter physics. Moreover, reduced dimensionality has interesting and non trivial implications on the interplay between electrons and phonons. In this respect, a striking example is the Fröhlich interaction, that is the coupling between electrons and the polar-optical phonons discussed in the previous section. Because of the LR nature of the Coulomb interaction, this coupling presents a clear dimensionality signature. In fact, the limit of $\mathbf{q} \rightarrow 0$ of the Fröhlich interaction is known to diverge in 3D [44], while it tends to a finite value in 2D [45]. To our knowledge this effect has not been clarified in 1D systems yet and will be discussed in Chapter 4

2.2 Charge transport and Boltzmann transport equation

The ultimate objective of transport theory is to determine the macroscopic transport coefficients of a material, such as its electrical conductivity, resistivity, and mobility. These macroscopic properties are determined by the microscopic behaviors of electrons and holes within the material. The most rigorous approach to studying charge transport in materials is to solve the many-body Schrödinger equation for both electrons and phonons. The microscopic behavior of particles involved in transport phenomena is exceedingly complex, and as such, it is often described using statistical methods. This approach involves formulating a transport theory that can provide a function that is related to the particles' positions and velocities at any given time. While the Liouville equation is the ideal choice for such a theory, its complexity makes it intractable [46]. However, simplifications of this equation lead to the Boltzmann transport equation (BTE) and the connected theory of transport.[46, 47, 48, 34] The BTE provides a probability distribution of a single particle in the phase space as a function of time, which is representative of the distribution of all the particles.

The key-ingredient here is the electronic distribution function $f(\mathbf{k})$, which is the unknown of the problem. The rate of change of the distributions consists depends on three different terms, being the diffusion one, the one related to the external field and the collisional contribution:

$$\frac{\partial f_{\mathbf{k}}}{\partial t} \Big|_{\text{diff.}} = - \frac{\partial f_{\mathbf{k}}}{\partial r} \cdot \mathbf{v}(\mathbf{k}), \quad (2.18)$$

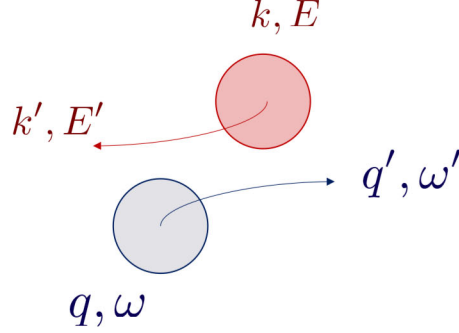


Figure 2.1: Sketch of the scattering process between two particles: an electron in red and a phonon in blue. Before the collision they are respectively characterized by momentum and energy (\mathbf{k}, E) and $(\mathbf{q}, \hbar\omega)$, while after the collision by (\mathbf{k}', E') and $(\mathbf{q}', \hbar\omega')$.

$$\frac{\partial f_{\mathbf{k}}}{\partial t}|_{\text{ext.field}} = -\frac{e}{\hbar} \left[\mathbf{E} + \frac{\mathbf{v} \times \mathbf{B}}{c} \right] \cdot \frac{\partial f_{\mathbf{k}}}{\partial \mathbf{k}}, \quad (2.19)$$

$$\frac{\partial f_{\mathbf{k}}}{\partial t}|_{\text{coll.}} = \sum_{\mathbf{k}'} P_{\mathbf{k}\mathbf{k}'} f(\mathbf{k}') (1 - f(\mathbf{k})) - P_{\mathbf{k}'\mathbf{k}} f(\mathbf{k}) (1 - f(\mathbf{k}')), \quad (2.20)$$

where in Eq.2.20 $P_{\mathbf{k}\mathbf{k}'}$ is the scattering probability from state \mathbf{k} to \mathbf{k}' . This can be computed by the Fermi Golden and considering as perturbation to the system Hamiltonian all the relevant sources of scattering (e.g., with defect, neutral or charge impurities). Under steady-state conditions, there will be no net change in the distribution function and the total sum of the partial derivative terms will be zero:

$$\frac{\partial f_{\mathbf{k}}}{\partial t}|_{\text{diff.}} + \frac{\partial f_{\mathbf{k}}}{\partial t}|_{\text{ext.field}} + \frac{\partial f_{\mathbf{k}}}{\partial t}|_{\text{coll.}} = 0. \quad (2.21)$$

Let us assume the occupation distribution $f(\mathbf{k})$ to be spatially uniform and time-independent (i.e., steady state). Then, the original Eq. 2.22 is further simplified and reduces to the fact that the distribution driven by the electric field is compensated by the scattering:

$$-\frac{e\mathbf{E}}{\hbar} \cdot \frac{\partial f}{\partial \mathbf{k}} = \left(\frac{\partial f}{\partial t} \right)_{\text{coll.}}, \quad (2.22)$$

and this is the equation we are interested in solving.

In this work we are interested in phonon-limited transport, meaning that the scattering mechanisms included in the calculation of $P_{\mathbf{k}\mathbf{k}'}$ are only electron-phonon interaction probabilities associated with the phonons of the system ν . As a consequence, we have:

$$P_{\mathbf{k}\mathbf{k}+\mathbf{q},\nu} \propto \frac{2\pi}{\hbar N} |g_{\mathbf{k}\mathbf{k}+\mathbf{q},\nu}|^2 \quad (2.23)$$

where $g_{\mathbf{k}\mathbf{k}+\mathbf{q},\nu}$ is the electron-phonon coupling matrix element (EPC), which in this work are calculated via DFPT. For the details of how the BTE is solved, since these are well-established,

we refer to specialized texts and reviews[34, 46, 47], and to Ref. [48] for the specific framework adopted in this thesis.

Other possible sources of scattering, not included in this thesis, are broadly speaking defects –usually found to dominate the low-temperature regime– and electron-electron interactions, which especially at high temperature and high doping (i.e., number of free carriers) could play an important role. In this thesis, we will focus on moderate-high doping at room temperature, where the phonon scattering is expected to play a central role, thus setting an upper limit for the performances achievable in real devices.

2.3 Summary

In this introductory chapter we aimed to qualitatively set and discuss the main topics at the center of this thesis: phonons, electron-phonon interactions and ultimately charge transport. In doing this, we attempted to highlight the role of dimensionality in shaping these properties, setting the ground for the next chapters. We introduced the basic formalism needed and we anticipate our main computational tools: density-functional and density-functional perturbation theory, and Boltzmann transport equation. In terms of concepts, we have introduced the many-body problem for crystalline solids within the well-known adiabatic approximation, and the key aspects of electronic structures and lattice dynamics, as well as electron-phonon interactions.

3 Density-functional and density-functional perturbation theory for one-dimensional materials

A direct objective of this thesis is to contribute to shedding light on the role of dimensionality in shaping materials properties, specifically in 1D systems. In this respect, particularly desirable would be the ability of performing accurate DFT [35, 36, 37, 33] and DFPT [26] calculations accounting for the correct dimensionality of these nanostructures. The bottleneck is that most of the available *ab-initio* codes rely on periodic-boundary conditions in the three spatial dimensions and this poses some challenges. Our goal here is to provide a reliable computational framework, based on DFT and DFPT as implemented within the standard Quantum ESPRESSO code [37, 49], to finally compute ground-state and linear-response properties for any 1D system. This will be the focus of the present chapter. First, in Section 3.1.1 we discuss the challenge posed by periodic-boundary conditions and we illustrate how to rigorously curate this issue by introducing the Coulomb cutoff technique. In Section 3.2, the implementation of the 1D framework within Quantum ESPRESSO is detailed: the subtleties of the cutoff implementation, as well as the modifications required throughout the code to compute, besides the potentials, energies, force and stress tensors, and linear response properties – that is phonons and electron-phonon interactions. Our developments will be applied in the next chapter to the study of polar-optical phonons and their coupling to electrons, showing the profound consequences of materials dimensionality and the relevance of the detailed implementation. A short summary follows in Section 3.3.

3.1 Introduction

Over the past three decades, nanostructures have captivated increasing interest due to their promises in terms of embodying novel physical paradigms and delivering cutting edge technological applications. Dimensionality plays indeed the role of an additional degree of freedom, expected to be relevant in several fields besides fundamental science. As regards 1D systems, our true *ab initio* theoretical understanding and the computational tools are yet less developed with respect to the higher-dimensional cases, that is 2D and 3D bulk materials. Thus, it rises

the urgency to bridge this gap.

On the modelling perspective, highly desirable is the ability of predicting and simulating the physics of low-dimensional systems from first-principles. For this, DFT and DFPT represent a powerful tool, proved to be accurately predictive in terms of electronic, structural and vibrational properties of materials [25, 26, 27, 28, 25, 29]. In particular, the combination of DFPT along with analytical models has been exploited in the past to reach a comprehensive understanding of phonons and their coupling to electrons in 3D and 2D materials [40, 41, 45, 29]; topics which are at the center of this thesis. The bottleneck is that most of the available *ab-initio* codes rely on periodic-boundary conditions in the three spatial dimensions (3D PBCs) and this poses some challenges when dealing with reduced dimensionality. While for some physical properties the spurious interactions between the periodic images can be suppressed by increasing the amount of vacuum within the simulation cell, many other properties will always be affected to some extent by the stray fields [45, 41, 50, 51, 52]. This is the case for polar (i.e., with spontaneous net macroscopic polarization [53, 54]) or charged and doped systems. More generally this is relevant for long-wavelength perturbations. In all these scenarios, the physical phenomena are indeed driven by long-range electrostatics which is ultimately ruled by materials dimensionality; this, in PBCs, is mystified by the presence of the periodic images. Works have been done in this direction based on the idea of suppressing these stray fields by smoothly truncating the Coulomb interactions between periodic images. This led to the capability of accounting for materials dimensionality when dealing with excited and neutral properties in 2D systems [29, 50], while only partly in 1D [50]. In fact, despite the efforts, computing linear-response properties of 1D materials via DFPT is still an open challenge.

In the following, we address this topic by developing a DFT and DFPT framework tailored for 1D materials. To this aim, we implement within the Quantum ESPRESSO (QE) distribution our version of the Coulomb cutoff technique [55, 50, 29] and we compute potentials, total energy, forces, stresses, phonons and electron-phonon interactions. We also implement the fitting non-analytic contribution to the dynamical matrix to insure smooth phonon Fourier interpolation. Thanks to our developments, we finally highlight the crucial role of open-boundary conditions in predicting the correct linear response of 1D systems. Namely, we will focus the discussion (see Chapter 4) on polar-optical phonons, infrared-active, and the Fröhlich coupling, showing for the first time in 1D – to our knowledge – their critical dimensionality signatures. Our work will be applied to a portfolio of relevant 1D systems including chains, wires and tubes.

3.1.1 Statement of the problem: periodic vs open-boundary conditions

First-principles calculations based on plane-wave basis sets rely on 3D PBCs. When simulating a system with reduced periodicity, such as 2D or 1D, this implies that periodic images are present in the non-periodic directions, being respectively one out-of-plane and two out-of-chain. Our goal consists in isolating the 1D system in such a way that it does not interact with

its images which otherwise would introduce spurious cross-talks in our calculations, eventually hindering the physical 1D response. This is of crucial importance in a variety of cases: neutral non-polar materials perturbed at long wavelengths, systems with net macroscopic polarization, and when doping or charging is included. In few words, correcting for the mentioned stray fields is essential whenever long-range electrostatics is relevant in nanostructures [29, 41, 51].

Let us start by framing the main concepts and the nomenclature. A 1D system is described as a crystal with periodicity only along one direction – $\hat{\mathbf{z}}$ in this case – termed ‘in-chain’, while having a limited extension (in the range of 1-100 nm) in the two other out-of-chain directions, $\hat{\mathbf{x}}$ and $\hat{\mathbf{y}}$. The cells in the crystal are identified by $\mathbf{R}_z = m_3 \mathbf{b}_3$ where m_3 is an integer and \mathbf{b}_3 is the in-chain primitive lattice vector; the out-of-chain components are instead constants. The position of each atom a within a cell is given by \mathbf{d}_a while its out-of-chain components may change depending on the structure (e.g., linear or zig-zag chains, tubes, wires). Switching to the reciprocal space, the crystal is described by the reciprocal vector \mathbf{G}_z generated by the in-chain primitive reciprocal lattice vector \mathbf{b}_3^* . Within DFT, the ground state properties of our system are fully determined by the charge density

$$\rho(\mathbf{r}_\perp, z) = 2e \sum_{\mathbf{k}, s} f(\epsilon_{\mathbf{k}, s}) |\psi_{\mathbf{k}, s}(\mathbf{r}_\perp, z)|^2, \quad (3.1)$$

where the sum runs over the spin-degenerate electronic states, labeled by the in-chain momentum k_z and the band index s , $f(\epsilon_{\mathbf{k}, s})$ is the Fermi occupation and $\psi_{\mathbf{k}, s}$ are the Bloch wavefunctions. The Kohn-Sham (KS) potential, V_{KS} , for a neutral/undoped 1D system consists in the external potential V_{ext} , the one created by the ions V_{ion} , plus two electronic contributions; that is the Hartree V_H and the exchange-correlation V_{xc} terms. The total potential reads as:

$$V_{\text{KS}}^{\text{1D}}(\mathbf{r}_\perp, z) = V_{\text{ext}}^{\text{1D}}(\mathbf{r}_\perp, z) + V_H^{\text{1D}}(\mathbf{r}_\perp, z) + V_{\text{xc}}^{\text{1D}}(\mathbf{r}_\perp, z). \quad (3.2)$$

These three potentials individually share the periodicity of the crystal, i.e., $V(\mathbf{r}_\perp, z + R_z) = V(\mathbf{r}_\perp, z)$, and the same holds for the electronic density in Eq. 3.1. What is relevant to highlight here is that materials properties can be derived starting from space integrals of the electronic charge density times these potentials.

When dealing with 3D PBCs, rather than simulating the isolated 1D system, one actually simulates an array of 1D systems repeated periodically in the two non-periodic dimensions of space with a given amount of vacuum to separate them. Thus the total potentials from each system, given in Eq.3.2, combine as

$$V_{\text{KS}}^{\text{3D}}(\mathbf{r}_\perp, z) = \sum_i V_{\text{KS}}^{\text{1D}}(\mathbf{r}_\perp - i\mathbf{R}_\perp, z), \quad (3.3)$$

where the index i runs over the periodic images along each of the two out-of-chain directions and \mathbf{R}_\perp is given by the distance between the images. The resulting potential $V_{\text{KS}}^{\text{3D}} \neq V_{\text{KS}}^{\text{1D}}$ satisfies

3D PBCs. Then, if the 1D system is perturbed at small momenta q_z (i.e., long-wavelengths) its electronic charge density, periodic only along the z -direction, will respond by generating a potential decaying in the out-of chain directions as $e^{-q \cdot |\mathbf{r}_\perp|}$, that is long-range (LR) interactions in real space. As soon as the range of these interactions is comparable with the distance d between the periodic repetitions, spurious contributions alter the response of the isolated system. In essence, PBCs constrain us to simulate a 3D crystal, consisting of weakly bounded 1D substructures, rather than the desired isolated 1D system. Similar considerations are valid, besides linear response, in charged, doped or polar materials where even the energetic and forces may be influenced by the presence of the periodic copies.

This issue can be addressed thanks to the Coulomb cutoff technique, as successfully demonstrated in several works [55, 50, 52, 29]. In fact, the standard method of simply increasing the vacuum between images only reduces the affected portion of the BZ, while the computational cost significantly increases. For a more systematic and physical solution, we implement a 1D Coulomb cutoff based on the one proposed in Ref. [50] in the relevant packages (PWScf and PHONONS) of the QE distribution [26, 37, 49]. This implementation leads to the correct 1D open boundary conditions (OBCs) for the computation of potentials, total energies, forces and stress tensors, phonons, and electron-phonon interactions.

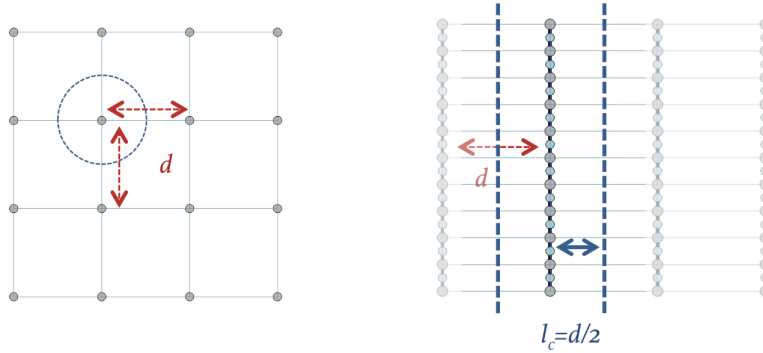


Figure 3.1: Sketch of the supercell construction for 1D systems and the effect of introducing the Coulomb cutoff.

Focusing, for instance, on linear response, when the electronic charge density is perturbed at momentum \mathbf{q} , the reach of the generated potential scales as $\lambda = 2\pi/q$ in the out-of plane (chain) direction(s). Thus for long-wavelength perturbations the spurious interactions persist even for very large distances [45, 41, 50, 51, 52]. In this light, the strategy of enlarging the vacuum to curate the stray fields not only increases the computational cost significantly, linearly (quadratic) with the distance in 2D (1D), but also never fully eliminates the issue. For momenta smaller than the inverse of the distance between periodic images there will always be the response of a 3D periodic system, instead of the physical 1D one. Note that these range of momenta, the closer to Γ the larger is the vacuum slab, are exactly those relevant for spectroscopic characterization, charge transport and many other prospective applications.

3.2 Implementation of 1D open-boundary conditions

The Coulomb cutoff technique consists in explicitly truncating the spurious interactions between the periodic images. This is done by modifying the Coulomb kernel rather than directly the potentials. The kernel is thus redefined as:

$$v_c(\mathbf{r}) = \frac{1}{r} \rightarrow \bar{v}_c(\mathbf{r}) = \frac{\theta(l_c - |\mathbf{r}_p|)}{|\mathbf{r}|}. \quad (3.4)$$

and all the LR contributions to the potentials (i.e., the ones affected by the stray fields, V_{ion} , V_{H}) are then obtained by convolution of this truncated kernel with the electronic charge density in Eq. 3.1

$$\bar{V}(\mathbf{r}) = e \int \rho(\mathbf{r}') \bar{v}_c(|\mathbf{r} - \mathbf{r}'|) d\mathbf{r}', \quad (3.5)$$

in such a way that a given charge in the 1D system interacts only with charges within a cylinder of radius l_c built around it. Note that although the kernel is discontinuous, the final potentials are indeed smooth thanks to the convolution with the charge density. Eventually, the material is effectively isolated, meaning that there is no physical 3D periodic system anymore; there is instead a 1D periodic system, repeated in the two additional dimensions of space in order to build potentials that mathematically still fulfill 3D PBCs but physically lead to the true 1D response.

3.2.1 1D Coulomb cutoff

In practice, within the code, the potentials (or at least their LR part) are generated in reciprocal space. Thus the truncated kernel from Eq. 3.4 becomes:

$$\bar{v}_c(G) = \frac{4\pi}{\mathbf{G}_{\perp}^2 + G_z^2} [1 + G_{\perp} l_c J_1(G_{\perp} l_c) K_0(G_z l_c) - G_z l_c J_0(G_{\perp} l_c) K_1(G_z l_c)] \quad (3.6)$$

where $J_n(x)$ and $K_n(x)$ are, respectively, the n^{th} order ordinary and modified cylindrical Bessel functions and l_c is the cutoff length. Note that for the $G_z = 0$ plane the expression in Eq. 3.6 is ill-defined since $K_1(x)$ diverges logarithmically for $x \rightarrow 0$. However, we are interested in the total potential given as the sum of the Hartree and ionic terms, both modified consistently via this kernel and each defined up to an arbitrary additive constant. Thus, the strategy proposed in the original work [50] to treat this singularity is to separate the divergence and include it in these constants; this is done by passing through a finite cylinder instead of the infinite one of Eq. 3.6. For the purposes of this work, we follow the same strategy with a crucial variation which will be highlighted in the following.

We start by defining $h = Nl_0$ to be the new height of the finite cylinder, where h_0 is an auxiliary unit length such that h is much larger than the cell size in the periodic direction. We then get

the following expression for the Fourier transform of the cutoff:

$$\bar{v}_c(\mathbf{G}_\perp, G_z) = \int_0^{l_c} \int_0^{2\pi} \int_0^h \frac{e^{-i(G_\perp r_\perp \cos\theta + G_z z)}}{\sqrt{r_\perp^2 + z^2}} r_\perp dr_\perp d\theta dz. \quad (3.7)$$

Focusing on the $G_z = 0$ plane, we are now left with

$$\bar{v}_c(\mathbf{G}_\perp, G_z = 0) = \int_0^{l_c} 2\pi J_0(G_\perp r_\perp) \log\left(\frac{h + \sqrt{h^2 + r_\perp^2}}{r_\perp}\right) dr_\perp, \quad (3.8)$$

where we can substitute $h = Nl_0$ and then split the expression in two integrals, I_1 and I_2 , of which only the first one depends on the height of the cylinder. The truncated kernel now reads:

$$\begin{aligned} \bar{v}_c(\mathbf{G}_\perp, G_z = 0) = & -2\pi \int_0^{l_c} J_0(G_\perp r_\perp) \log(r_\perp / l_0) dr_\perp + \\ & + 2\pi \int_0^{l_c} J_0(G_\perp r_\perp) \log(N + \sqrt{N^2 + (r_\perp / l_0)^2}) dr_\perp. \end{aligned} \quad (3.9)$$

The first integral, not dependent on h , has the following well-defined solution:

$$I_1 = 2\pi \frac{1 - J_0(G_\perp l_c) - G_\perp l_c J_1(G_\perp l_c) \log(l_c / l_0)}{G_\perp^2}, \quad (3.10)$$

while the second integral, I_2 , depends on h (i.e., on N) and gives:

$$I_2 = 2\pi l_c \log(2N) \frac{J_1(G_\perp l_c)}{G_\perp}. \quad (3.11)$$

Clearly this latter term contains the singularity we wanted to isolate (i.e., $\lim_{N \rightarrow \infty} I_2 = \infty$), and we can drop it by invoking charge neutrality as long as we apply the same cutoff to both the Hartree and the ionic potentials. Finally, we are interested in the $\bar{v}_c(\mathbf{G} = 0)$ value of the cutoff. Thus, if we consider the limit of I_1 for $G_\perp \rightarrow 0$, we get the limit behavior :

$$\lim_{G_\perp \rightarrow 0} I_1 \sim -\frac{\pi}{2} l_c^2 [2 \log(l_c / l_0) - 1]. \quad (3.12)$$

In all this, the true novelty of our approach with respect to what proposed by Rozzi and coauthors [50] is the ex novo parameter l_0 , defined as $l_0 = \frac{l_c}{\exp(0.5)}$. This parameter carries out two crucial functions: (1) it enables the use of a dimensionless argument for the logarithm $\log(l_c / l_0)$ and (2) it sets the average potential over the unit cell to zero, i.e., $\bar{V}(\mathbf{G} = 0) = \bar{v}_c(\mathbf{G} = 0) = 0$, which is the conventional choice in QE for both 3D and 2D materials.

The final expression for our 1D Coulomb cutoff is:

$$\bar{v}_c(\mathbf{G}) = \begin{cases} \frac{4\pi}{\mathbf{G}_\perp^2 + G_z^2} [1 + G_\perp l_c J_1(G_\perp l_c) K_0(G_z l_c) - G_z l_c J_0(G_\perp l_c) K_1(G_z l_c)], & \mathbf{G}_\perp, G_z \neq 0 \\ \frac{4\pi}{\mathbf{G}_\perp^2} [1 - G_\perp l_c J_1(G_\perp l_c) \log(\frac{l_c}{l_0}) - J_0(G_\perp l_c)], & \mathbf{G}_\perp \neq 0, G_z = 0 \\ 0 & \mathbf{G} = 0 \end{cases} \quad (3.13)$$

Since the $K(x)$ functions damp the oscillations of the $J(x)$ functions very quickly, as pointed out in the original paper [50], the cutoff is expected to act only on the smallest values of \mathbf{G} , while the bulk behavior is soon recovered for larger values. Note that the cutoff l_c needs to be at least as large as the maximum distance between electrons belonging to the system, i.e. the effective thickness of the material $2t$, otherwise some physical interactions of the 1D system itself are erroneously cut. In turn, the size of the simulation cell in the non-periodic directions d should be such that electrons belonging to different periodic images are separated by at least l_c . In practice, the cutoff is chosen to be $l_c = d/2$, and the supercell built such that $d > 4t$.

In the following, we detail the implementation of the relevant physical ground-state (potentials, energies, forces, stresses) and linear-response (phonons and electron-phonon coupling) properties. For the sake of simplicity, we follow the same steps involved in the implementation for 2D systems [45], limiting the present discussion to what is different in 1D with respect to this previous case.

Potentials

The KS potential is the sum of the external (in this case simply ionic) the Hartree, and the exchange-correlation contributions:

$$V_{\text{KS}}(\mathbf{r}_\perp, z) = V_{\text{ext}}(\mathbf{r}_\perp, z) + V_{\text{H}}(\mathbf{r}_\perp, z) + V_{\text{XC}}(\mathbf{r}_\perp, z), \quad (3.14)$$

Here we are interested in modifying only the long-range part of these potentials and thus we can neglect the exchange-correlation term which is short-ranged. Note that this implementation holds for all types of pseudopotentials (i.e., norm-conserving, ultrasoft and projector augmented wave function). Following the conceptual steps proposed in the 2D paper [45], we proceed by modifying in the QE 3D code the Fourier transform of the local ionic potential and the Hartree potential by substitution the reciprocal expression of the truncated Coulomb kernel. Thus in our implementation with the 1D cutoff we define the local ionic potential as:

$$V_{\text{ion}}^{\text{loc}}(\mathbf{G}) = \sum_a e^{-i\mathbf{G} \cdot \mathbf{d}_a} (v_a^{\text{SR}}(\mathbf{G}) + v_a^{\text{LR}}(\mathbf{G})) \rightarrow \bar{V}_{\text{ion}}^{\text{loc}}(\mathbf{G}) = \sum_a e^{-i\mathbf{G} \cdot \mathbf{d}_a} (v_a^{\text{SR}}(\mathbf{G}) + \bar{v}_a^{\text{LR}}(\mathbf{G})), \quad (3.15)$$

where the relevant term, that is the LR part, transforms as

$$v_a^{\text{LR}}(\mathbf{G}) = -\frac{Z_a}{\Omega} v_c(\mathbf{G}) e^{-|\mathbf{G}|^2/4\eta} \rightarrow \bar{v}_a^{\text{LR}}(\mathbf{G}) = -\frac{Z_a}{\Omega} \bar{v}_c(\mathbf{G}) e^{-|\mathbf{G}|^2/4\eta}, \quad (3.16)$$

and for the Hartree term we have trivially

$$V_H(\mathbf{G}) = v_c(\mathbf{G}) n(\mathbf{G}) \rightarrow \bar{V}_H(\mathbf{G}) = \bar{v}_c(\mathbf{G}) n(\mathbf{G}). \quad (3.17)$$

As a first validation of our method, we check the modifications introduced so far by focusing

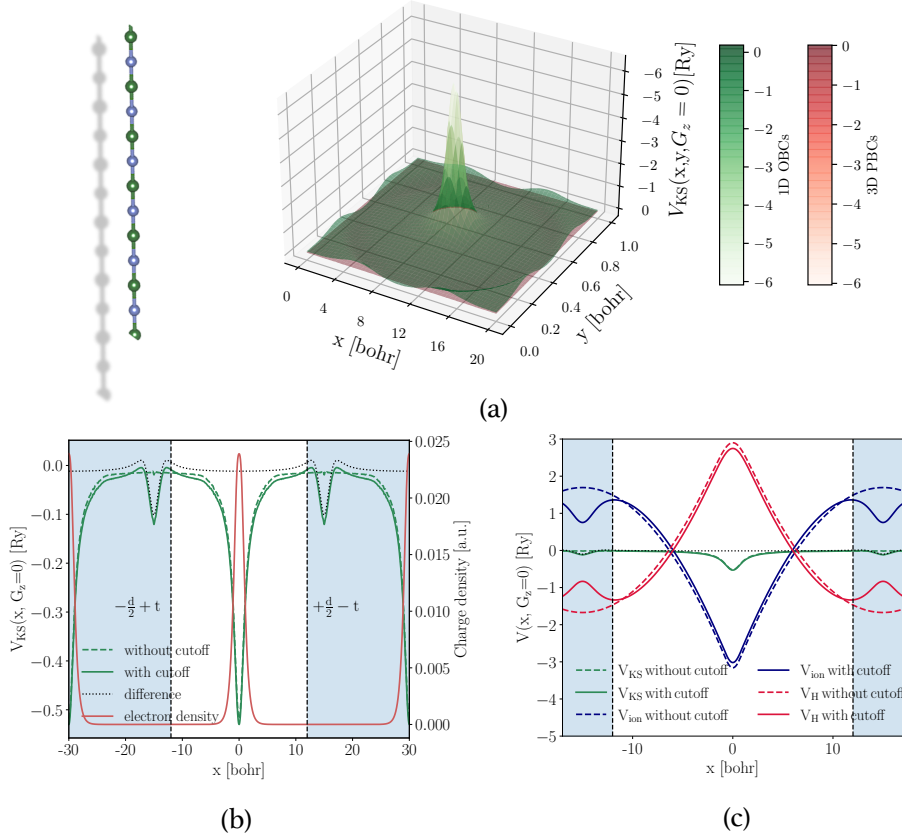


Figure 3.2: In the first panel (a) we show the KS potential (inverted y axis) averaged along the wire, with (green) and without (red) the inclusion of the cutoff. In the second panel (b) we focus on the x-axis cross-section of the KS potential and we highlight the physical region. Also the electronic charge density is reported for reference. In the last panel (c) we zoom on the physical region and we plot besides the KS potential also the ionic and Hartree terms, always comparing each potential with and without the 1D cutoff.

on the simplest system in our portfolio: an atomic chain of BN. Thus, we plot in Fig. 3.2 the total potential, as well as the single contributions, without the cutoff (3D PBCs) in red, and after its inclusion (1D OBCs) in green; this is shown in three different panels. The first panel offers a three-dimensional representation of the total KS potential averaged along the wire direction, \hat{z} , and plotted as a function of the two out-of chain directions, \hat{x} and \hat{y} (which in

this case are equivalent by symmetry). To better comprehend the effect of the cutoff, in the second panel of Fig. 3.2 we focus on the cross section of the total potential along one of the two equivalent out-of-chain directions. Together with the KS potential in this case we plot the electronic charge density, and we highlight the limits of the physical region defined by the 1D cutoff by shading the rest of the plot, i.e., for $x > +\frac{d}{2} - t$ or $x < -\frac{d}{2} + t$ with t being the radius of the 1D system (here estimated based on the charge density). Within this physical region, V_{KS} with and without the cutoff is expected to be the same up to a constant. This constant comes from the fact that both KS potentials average to zero but the one with the cutoff exhibits artifacts, i.e., ‘bumps’, outside the physical region, as already discussed for the 2D implementation [45]. Eventually, in the third panel we zoom on the physical region and we add to the picture also the ionic and Hartree potentials, with and without the 1D cutoff. Within 3D PBCs, the choice of setting the $\mathbf{G} = 0$ value of the ionic or Hartree potential to zero is equivalent to the inclusion of a compensating jellium background. At variance with the 2D case, in 1D the potential generated by a linear infinite distribution of charge in the surrounding is logarithmic instead of linear, while the jellium bath adds a quadratic contribution to the potential between periodic images. The correct 1D behavior is restored once the cutoff is applied, however the effects observed on the cutoff are more subtle with respect to what observed in 2D systems when applying the cutoff[29].

Energies

The total energy per unit cell is:

$$E_{\text{tot}} = E_{kin} + E_{\text{ext}} + E_H + E_{XC} + E_{i-i} \quad (3.18)$$

the sum of, respectively, the electronic kinetic energy, the energy of the electronic in the external potential created by the ions, the Hartree energy, the exchange-correlation energy and the ion-ion interaction energy. Similarly to what we did for the potentials, for the energy we only need to modify the LR contributions. These modifications are straightforward: we simply need to propagate consistently throughout the code the modification of the truncated kernel by substituting $v_c(\mathbf{r}) \rightarrow \bar{v}_c(\mathbf{r})$.

Forces

Once the 1D potentials and energies are known, the forces acting on each ion a are obtained by the derivative of the total energy with respect to the displacement $\mathbf{u}_{a,i}$ along a given cartesian direction i :

$$\mathbf{F}_{a,i} = -\frac{\partial E_{\text{tot}}}{\partial \mathbf{u}_{a,i}} = -\int_{\Omega} n(\mathbf{r}) \frac{\partial \bar{V}_{\text{ion}}}{\partial \mathbf{u}_{a,i}} d\mathbf{r} - \frac{\partial E_{i-i}}{\partial \mathbf{u}_{a,i}} \quad (3.19)$$

where all the terms which do not involve explicitly interaction with ions have been dropped

and we always imply derivatives at zero displacement $\mathbf{u}_{a,i}$. Thus, for neutral systems we are left with only two terms: the force on the ion from the electrons and the contribution given by the interaction with the other ions. Both terms can be obtained as detailed in Ref. [45] for the 2D case, simply taking care of substituting the truncated potential consistently within the code.

Stresses

In addition to atomic forces, another important quantity for structural optimization is the stress. Stresses are computed as derivatives of the total energy with respect to the strain tensor:

$$\sigma_{i,j} = -\frac{1}{\Omega} \frac{\partial E_{\text{tot}}}{\partial \epsilon_{i,j}} \quad (3.20)$$

where i and j represents Cartesian coordinates. Once again, we need to modify only the terms derived from the LR potentials which may be affected by the periodic images, this is the case for the Hartree term $\sigma_{i,j}^H$ and for the contribution coming from the LR part of the local ionic potential, $\sigma_{i,j}^{\text{loc,LR}}$. In this case the formula is different with respect to the 2D case and is specific of the 1D implementation. In fact, modifying the kernel and potentials is not enough, we also need the derivative of the Coulomb kernel with respect to the strain tensor appearing in the energy terms respectively:

$$E_H = \frac{\Omega}{2} \sum_{\mathbf{G} \neq \mathbf{0}} n^*(\mathbf{G}) V_H(\mathbf{G}) \quad (3.21)$$

and

$$E_{\text{ion}}^{\text{loc,LR}} = \Omega \sum_{\mathbf{G} \neq \mathbf{0}} n^*(\mathbf{G}) \sum_a e^{i\mathbf{G} \cdot \mathbf{d}_a} v_a^{\text{LR}}(\mathbf{G}) \quad (3.22)$$

Thus, we need to compute $\partial v_c(\mathbf{G}) / \partial \epsilon_{i,j}$. It follows:

$$\frac{\partial v_c(\mathbf{G})}{\partial \epsilon_{i,j}} = -\frac{\partial v_c(\mathbf{G})}{\partial G_i} G_j \quad (3.23)$$

and in the 1D case we have, based on Eq. 3.13:

$$\frac{\partial \bar{v}_c(\mathbf{G})}{\partial G_z} = -\frac{\bar{v}_c(\mathbf{G})}{\mathbf{G}_{\perp}^2 + G_z^2} 2G_z \left[1 - \beta_z(\mathbf{G}_{\perp}, G_z) \right], \quad (3.24)$$

$$\frac{\partial \bar{v}_c(\mathbf{G})}{\partial |\mathbf{G}_{\perp}|} = -\frac{\bar{v}_c(\mathbf{G})}{\mathbf{G}_{\perp}^2 + G_z^2} 2G_{\perp} \left[1 - \beta_{\perp}(\mathbf{G}_{\perp}, G_z) \right], \quad (3.25)$$

with β_z and β_\perp defined as follows:

$$\beta_z = \frac{|\mathbf{G}|^2}{2G_z \bar{v}_c} \left[-G_\perp l_c^2 J_1(G_\perp l_c) K_1(G_z l_c) - l_c J_0(G_\perp l_c) K_1(G_z l_c) + \frac{G_z l_c^2}{2} J_1(G_\perp l_c) (K_0(G_z l_c) + K_2(G_z l_c)) \right], \quad (3.26)$$

$$\beta_\perp = \frac{|\mathbf{G}|^2}{2G_\perp \bar{v}_c} \left[\frac{G_\perp l_c^2}{2} K_0(G_z l_c) [J_0(G_\perp l_c) - J_2(G_\perp l_c)] + l_c J_0(G_\perp l_c) K_1(G_z l_c) + G_z l_c^2 J_1(G_\perp l_c) K_1(G_z l_c) \right]. \quad (3.27)$$

Phonons and EPC

The key-ingredient to compute phonon dispersion relations and electron-phonon interactions is the response of the electronic density to a phonon perturbation. This is obtained in DFPT by solving self-consistently a system of equations in which the unknown is the lattice periodic part (in italics) of the perturbed KS potential $\frac{\partial \tilde{V}_{KS}(\mathbf{r}_\perp, z)}{\partial \mathbf{u}_{a,i}(\mathbf{q}_z)}$. In practice, what is needed to compute linear-response properties are the derivatives of the previously defined potentials and energies, already modified, consistently, via the Coulomb cutoff. Once again we are interested in modifying only the LR terms of the perturbed KS potential, that is the local ionic $\tilde{V}_{ion}^{loc}(\mathbf{q} + \mathbf{G})$ and Hartree $\tilde{V}_H(\mathbf{q} + \mathbf{G})$ contributions. The truncated response is thus obtained by propagating the truncation of these potentials consistently. Once this is done, the implementation of the dynamical matrix, from which we get the phonon dispersion relations, and the EPC matrix elements are straightforward. The crucial consequence of the cutoff implementation on these quantities will be at the center of the discussion in the following section. For more details about how these are effectively implemented within QE, the reader can refer to Ref. [45].

3.2.2 Phonon interpolation and non-analytical corrections

Besides the implementation of the 1D Coulomb cutoff, another relevant modification in the code concerns the Fourier interpolation of phonon dispersions. This scheme enables to efficiently compute the full phonon dispersion on a dense momentum grid, first computing the dynamical matrix on a coarse momentum grid, Fourier transforming it into finite-ranged interatomic force constants (IFCs), and finally Fourier transforming the IFCs back in reciprocal space on a finer momentum grid. However, in most of semiconductors and insulators, non-vanishing BECs drive LR dipole-dipole interactions, as we have seen in Section 2.1.3. These are dimensionality dependent and lead to IFCs slowly decaying in real-space [56, 41, 51, 57, 42, 40]. The Fourier interpolation scheme is then not able to fully capture these non-analytic terms

since it is based, instead, on the real-space localization of the IFCs [27, 26, 58, 25, 59, 41]. This prevents us from getting accurate phonon interpolation when dealing with polar-optical phonons in a generic n -dimensional material. The standard solution is to build a reciprocal space model for these dipolar interactions and separate the dynamical matrix into a short-range and long-range component,

$$D_{ai,bj}(\mathbf{q}) = D_{ai,bj}^{\text{SR}}(\mathbf{q}) + D_{ai,bj}^{\text{LR}}(\mathbf{q}) \quad (3.28)$$

such that the correct long-ranged contribution to the dynamical matrix can be excluded and then re-added in the interpolation procedure [25, 41, 57]. This contribution $D_{ai,bj}^{\text{LR}}(\mathbf{q})$ in 1D corresponds to the one already presented in Ref. [57] and will be at the center of the following chapter of this thesis. It is worth mentioning that the dipole-dipole terms considered here are the leading contribution to the long-range IFCs, but higher orders may be present as well with, in general, minor consequences on the phonon dispersion relations [51, 60].

The implementation of $D_{ai,bj}^{\text{LR}}(\mathbf{q})$ requires the explicit analytical form (which will be given in the following chapter) and the knowledge of several physical quantities. Masses, eigenvectors, eigenvalues and BECs are directly obtained from the underlying DFT and DFPT calculations. What need to be parametrized are instead the effective radius t of the 1D system and its macroscopic dielectric tensor ϵ^{1D} , as will be explained in i.e., Chapter 4. This 1D dielectric tensor differs from the one computed in QE ϵ^{QE} , which strongly depends on the size of the simulation cell. We will come back to this point in the following chapter, Section 4.4. In practice, in implementing the correction to the dynamical matrix, we automatize the choice of the effective radius as $t = d/4$, where in the most general case d is the size of the cell in the non-periodic direction. This choice is reasonable assuming that d has been chosen as the minimum size to satisfy the cutoff requirements as explained in Sec. 3.2.1.

3.3 Summary

In summary, in this chapter we presented a novel DFT and DFPT framework to simulate ground-state and linear-response properties of 1D systems from first-principles. This is achieved by implementing our modified version of the Coulomb cutoff technique for 1D systems in the QE distribution package (namely, pw.x and ph.x codes). Our implementation [61] starts from modifying the Coulomb kernel and thus the relevant potentials; this eventually unlocks the possibility to compute energies, forces, stresses, phonons and electron-phonon properties for any kind of system with 1D periodicity (chains, wires, tubes, polymers...). We then apply our developments to a simple yet representative portfolio of neutral systems with no net spontaneous polarization. These results will be presented in the following chapter, cross-validated and supported by novel theoretical developments. There we will focus on polar-optical phonons, their dispersion relations and their coupling to electrons and the related electronic lifetimes, showing how these are dramatically affected by materials dimensionality. All this will demonstrate the fundamental role of the 1D cutoff here presented in restoring the

true physical response of 1D systems and its physical signatures.

4 Infrared-active phonons in one-dimensional materials, their coupling to electrons and spectroscopic signatures

Vibrations are key to understanding materials -their thermodynamic and transport properties as well as their spectroscopic signatures. The microscopic understanding of polar-optical, infrared-active, phonons in 3D materials is a pillar of solid-state physics. However, the same understanding breaks down in lower dimensions, with profound consequences for physical properties and spectroscopic characterization; both of which are key to the future of nanotechnology. To date, we have reached a well established understanding of these vibrations in 2D materials based on theoretical models, describing the long-wavelength details of the related dielectric shift, and tailored algorithmic developments. In contrast, the same understanding in 1D is still missing and calls for further investigation. In this chapter, we answer this challenge by unveiling the character of vibrational excitations and their coupling to electrons in 1D systems, including nanotubes, nanowires, atomic chains and polymers –systems extensively discussed in the literature. We accomplish this aim by developing a novel theory for the 1D case and validating it through first-principles simulations using the newly implemented 1D DFT-DFPT framework introduced in the previous Chapter 3. After reviewing the state of the art in the field and the motivations behind this work (see Section 4.1), we fully detail our analytical derivation in Section 4.2, and we discuss the central results in terms of polar-optical phonons, their dispersion relations, and their coupling to electrons. Finally, Section 4.4 is devoted to the application of our developments to a portfolio of prototypical 1D systems: BN atomic-chains and nanotubes, and GaAs nanowires. To conclude, we discuss the experimental relevance of this work in Section 4.5, showing that the proposed model not only offers a clear and unprecedented understanding but also represents a practical tool for the experimental community to aid in the spectroscopic characterization of nanostructures. The chapter is closed by a summary of the key concepts in Section 4.6.

4.1 State of the art and motivation

Phonons and their interactions with electrons and photons are key ingredients in determining the thermodynamic, transport, and optical properties of materials, to name a few [34, 30]. Notably, as described in Chapter 2, long-wavelength optical phonons in semiconductors and insulators can give rise to electric fields which strongly affect not only their dispersion relations [41, 51, 62, 63, 64, 64, 65] but also the physics of Fröhlich electron-phonon interactions [45, 66, 67] and phonon polaritronics [68].

To summarize the content of section 2.1.3, when atoms in the lattice have non-vanishing BECs, optical phonons can generate a polarization density and couple with electric fields. Those modes are then termed polar and are infrared active. In addition, for longitudinal atomic displacement patterns, and in particular for purely longitudinal optical (LO) modes, a long-range electric field is generated that becomes macroscopic in the long-wavelength limit [39, 69, 42]. Creating an additional electric energy density in the material is more costly, and thus the frequency of the LO mode is usually blue-shifted. While the strength of this effect is well-known to depend on the dielectric properties of the material, i.e., BECs and macroscopic dielectric tensor, its dependency on phonon momenta and size is ruled solely by dimensionality and is still poorly understood.

In 3D bulk materials, the energy shift of the LO mode is constant around the BZ center as a function of the norm of the momentum (i.e., the famous LO-TO splitting). At variance, in 2D, it has been shown to depend linearly on momentum and to vanish at Γ exactly [41, 51, 70]. This breakdown can be expected in 1D systems as well [71, 72, 73, 62, 74]; nonetheless, its actual behavior remains an open question. So far, several theoretical and experimental studies have addressed polar-optical phonons in 1D. It is generally claimed that the polar contribution to the LO energy should vanish at $q_z = 0$ in low-dimensional materials [71, 72, 73, 62, 74]. Despite this, to the best of our knowledge, the peculiarity of this polar shift at finite \mathbf{q}_z in 1D is still debated, since the long-range dipole-dipole interactions and their screening have not yet been fully derived. In the Raman spectra of these materials, a general red-shift and asymmetric broadening of the main peaks is found with respect to their bulk counterpart, as well as the appearance of new modes such as surface optical phonons (SO) and radial breathing modes (RBM) [75, 76, 77, 78, 79, 80, 71, 70, 81, 63, 82, 73, 72]. However, these features are shared with non-polar phonons and are generally argued to depend on quantum confinement, curvature effects, and relaxation of the $\mathbf{q} = 0$ selection rule.

While the initial motivation behind this work was to fill this theoretical gap, our inspiration was fueled by the experimental work described in Ref. [1]. In that paper, Kim Wonjong and coauthors presented a novel self-assisted technique to grow GaAs nanowires of reduced size and controlled shape. Following the proposed strategy, they were able to grow arrays of nanowires characterized by a bulkier nanowire (NW) structure at the base (≈ 100 nm in radius) while terminating with quantum-thin nanoneedles (NN) on top (≈ 10 nm). Raman investigation showed a downshift of 2.5 cm^{-1} in the position of the LO peak towards the TO one

as the radius of the wires was shrunk. The fact that the TO peak remained unchanged suggests that this shift is dictated by the discussed dielectric effect. Unfortunately, the lack of a theory to support this hypothesis hampered a more in-depth understanding of the phenomenon. Thus, the goal here is to provide such a theory that links the unique dimensionality fingerprint on the dispersion relations, and hence the information of the 1D radius, to Raman and infrared shifts in real experiments on single isolated 1D systems.

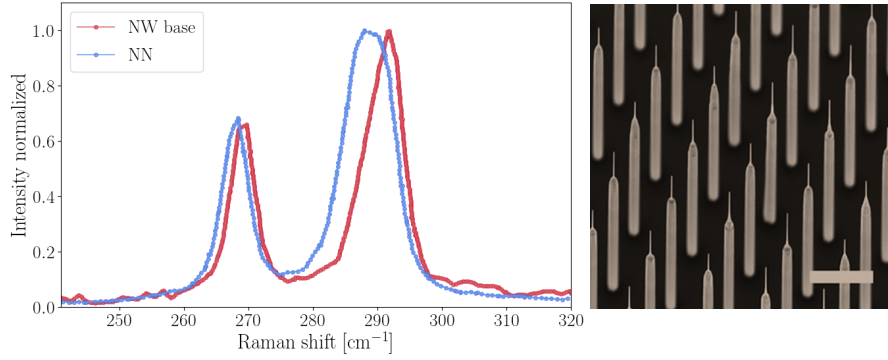


Figure 4.1: Figure readapted from Ref. [1]. In the first panel, the Raman spectra of the NW stems (red) and the NNs (blue) are shown, obtained in the backscattering geometry at room temperature. On the right, a scanning electron microscopy (SEM) image of the regular array of NNs on top of NWs is reported.

4.2 Analytical model

In the following we will have in mind, for the sake of simplicity, the limit case of the ultimate 1D system: a linear chain of atoms. However, the derivation proposed here still holds for any 1D materials, including nanowires, nanotubes, and polymers. Let us start by framing the discussion, setting the nomenclature, and introducing the electrostatic model at the center of this chapter. The 1D system can be described as a charge distribution periodic along the \hat{z} direction, aligned with the chain axis in this case, and homogeneous in the two radial directions within an effective radius t . We consider vacuum outside, but the generalization to other surrounding media is straightforward, as will be highlighted in the following. As a consequence of the cylindrical symmetry of our problem, it comes naturally to separate the variables both in real and reciprocal space as follows:

$$\mathbf{r} \rightarrow (\mathbf{r}_\perp, z) \quad \mathbf{q} \rightarrow (\mathbf{q}_\perp, q_z), \quad (4.1)$$

where \perp stands for transverse to the chain axis, i.e., out-of-chain, while z indexes the in-chain components. We then model the dielectric properties of the system with

$$\epsilon^m = \begin{pmatrix} \epsilon_\perp^m & 0 & 0 \\ 0 & \epsilon_\perp^m & 0 \\ 0 & 0 & \epsilon_z^m \end{pmatrix} \quad Z^a = \begin{pmatrix} Z_\perp^a & 0 & 0 \\ 0 & Z_\perp^a & 0 \\ 0 & 0 & Z_z^a \end{pmatrix},$$

Chapter 4. Infrared-active phonons in one-dimensional materials, their coupling to electrons and spectroscopic signatures

being respectively the macroscopic dielectric tensor inside the material (i.e., the high frequency limit of the dielectric permittivity ϵ^∞) and the BECs tensor associated to each atom a . Both tensors are here considered to be diagonal, namely isotropic in the out of chain directions, $\hat{\mathbf{x}}$ and $\hat{\mathbf{y}}$, while the properties differ in the periodic direction $\hat{\mathbf{z}}$. Thus, ϵ_\perp^m accounts for the dielectric properties of the material around the wire axis, supposed to be uniform and homogeneous, while along the chain ϵ_z^m is the quantity we are interested in. The same happens for the BECs tensor, for which we expect to find values significantly different from zero just along the chain direction (this is strictly true only for the ultimate 1D chain).

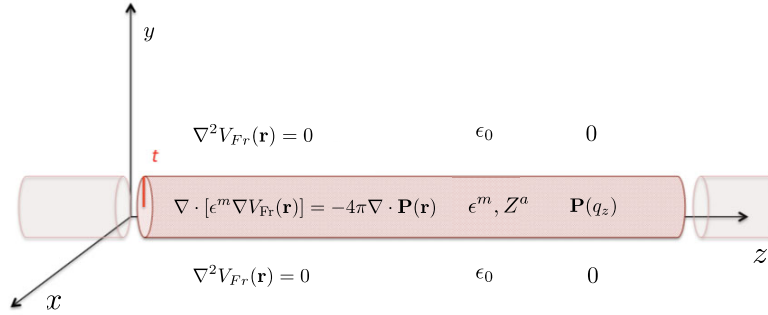


Figure 4.2: Schematic representation of the 1D system within our model, i.e., filled cylinder of radius t . The dielectric properties (ϵ^m , Z^a) are summarized both inside and outside the cylinder. The equations to be solved in each region are reported.

In our model, the polarization density induced by phonons, i.e., atomic displacement patterns, plays a critical role. This polarization density leads to electrostatic effects, which in turn modify the phonons themselves and their coupling to electrons. Within the dipolar approximation, and in the absence of any external field, this polarization reads as:

$$\mathbf{P}(\mathbf{r}) = \frac{e^2}{L} \sum_a Z^a \cdot \mathbf{u}_a(\mathbf{r}) \quad (4.2)$$

where e is the elementary electron charge, L is the linear dimension which characterizes the unit cell of the 1D system, and \mathbf{u}_a indicates the displacement of a given atom a in the unit cell. The polarization density can originate a potential, sharing its same periodicity, which describes the interactions between electrons and the LO phonons. This potential is termed Fröhlich, V_{Fr} , being related to the famous EPC, and is obtained by solving the following Poisson equation:

$$\nabla \cdot [\epsilon \nabla V_{\text{Fr}}(\mathbf{r})] = -4\pi \nabla \cdot \mathbf{P}(\mathbf{r}). \quad (4.3)$$

Note that the charge density on the right-hand side of Eq. 4.3 Fourier-transforms in reciprocal space as $\mathbf{q} \cdot \mathbf{P}(q_z)$; this charge is the source of the potential on the left-hand side, and thus of the electric field, and vanishes as soon as the phonon propagation (along momentum $\mathbf{q} = q_z \hat{\mathbf{z}}$) and the polarization (along displacements \mathbf{u}_a^q) are orthogonal. Therefore, within this model, only phonons labeled as LO in the long-wavelength limit (i.e., characterized by $\mathbf{u}_v^a \parallel \mathbf{q}$) generate a

sizable electric field and experience the dielectric shift we want to investigate. Thus, in the following, we will focus on strictly in-chain atomic displacements $\mathbf{u}_V^a \rightarrow \mathbf{u}_{LO}^a$. The potential in Eq. 4.3 needs to fulfill the proper electrostatic boundary conditions (i.e., continuity of the potential and its derivatives at the interfaces, and no divergences):

1. Continuity of the parallel electric field E_{\parallel} (from Maxwell's equation $\nabla \times \mathbf{E} = 0$);
2. Continuity of the orthogonal dielectric displacement D_{\perp} (from Maxwell's equation $\nabla \cdot \mathbf{D} = 0$);
3. No divergences in V_{Fr} ;
4. Continuity of V_{Fr} ,

where parallel and orthogonal are defined with respect to the chain axis. It is worth noticing that the continuity of the parallel component of the electric field guarantees also the potential to be continuous. At this point, our problem reduces to solve a second order non-homogeneous linear partial differential equation. Thus, the most general solution of the potential can be expressed as sum of the homogeneous solution, V_h , and a particular one, V_p :

$$V_{Fr} = V_p + V_h, \quad (4.4)$$

where V_h actually corresponds to a family of possible solutions of the homogeneous equation defined up to one or more constants; these constants are determined by enforcing the desired boundary conditions. Note that it is the complete solution V_{Fr} which has to satisfy the boundary conditions enumerated above, not the single V_p and V_h . Once the Poisson equation is solved, the knowledge about the electrostatic potential gives access to the long-wavelength dispersion relations of polar-optical phonons. This interaction potential, integrated in the non-periodic directions, that is $V_{Fr}(q_z)$, is related to the Coulomb screened interaction, $W_c(q_z)$. In this context:

$$W_c(q_z) = \frac{V_{Fr}(q_z)}{q_z P(q_z)}, \quad (4.5)$$

where $q_z P(q_z)$ corresponds to the real-space divergence of the polarization density, i.e., the perturbing charge density within our problem. Once we obtain the screened Coulomb interaction, the electric field and the forces acting on each ion a can be computed, being respectively:

$$\mathbf{E}(\mathbf{q}) = -\nabla V(q_z) = -W_c(q_z) P(q_z) q_z^2 \hat{\mathbf{z}}, \quad (4.6)$$

and

$$\mathbf{F}_a(\mathbf{q}) = \mathbf{E}(\mathbf{q}) \cdot Z^a. \quad (4.7)$$

Eventually, this new contribution to the atomic forces turn into a LR and non-analytical term

Chapter 4. Infrared-active phonons in one-dimensional materials, their coupling to electrons and spectroscopic signatures

in the dynamical matrix:

$$D_{ai,bj} = -\frac{1}{\sqrt{M_a M_b}} \frac{\partial F_{a,i}}{\partial u_{b,j}} = \frac{e^2}{L} W_c(q_z) \frac{(\mathbf{q} \cdot \mathbf{Z}^a)_i (\mathbf{q} \cdot \mathbf{Z}^b)_j}{\sqrt{M_a M_b}}, \quad (4.8)$$

which is ultimately responsible for the dielectric shift we are interested in. Here a and b indicate the atoms, while i and j the Cartesian directions. In the following, we will solve the Poisson equation, as described in this section, in the attempt of answering fundamental questions such as: what is the dimensionality signatures on polar-optical phonons in 1D materials? How does it compare to the 3D and 2D cases? Are we able to shed light on the transition between different materials dimensionalities?

4.2.1 Solving the Poisson equation

To solve the Poisson equation we exploit the periodicity of the 1D system along the z -axis and its cylindrical symmetry. First, we will look for the particular solution V_p and then we will proceed to compute the homogeneous one V_h . Before diving into the details of the analytical derivation, we apply the separation of variables to our definition of the polarization density in Eq. 4.2 and we write the LO atomic displacement pattern as a superposition of phonon waves of momenta q_z :

$$\mathbf{P}(\mathbf{r}_\perp, z) = \frac{e^2}{L} \sum_a \mathbf{Z}^a \cdot \mathbf{u}_a(\mathbf{r}_\perp, z) = \frac{e^2}{L} \sum_a \sum_{q_z} \frac{\mathbf{e}_a(q_z)}{\sqrt{M_a}} e^{i z q_z} f(\mathbf{r}_\perp). \quad (4.9)$$

Here $\{\mathbf{e}_a^q(q_z)\}$ are the eigenvectors of the dynamical matrix scaled by the nuclear masses M_a and $f(\mathbf{r}_\perp)$ models the out-of-chain profile of the polarization density. One can adopt several functional forms for this profile $f(\mathbf{r})$ (such as Delta, Gaussian or Lorentzian distribution functions). Here we choose a Heaviside step function in the radial coordinate, \mathbf{r}_\perp ,

$$f(\mathbf{r}_\perp) = \frac{h(t - |\mathbf{r}_\perp|)}{\pi t^2}, \quad (4.10)$$

normalized to unity over the cross-sectional area, that is

$$\int_0^\infty \text{const.} \times h(t - |\mathbf{r}_\perp|) 2\pi r_\perp dr_\perp = 1 \rightarrow \text{const.} = \frac{1}{\pi t^2},$$

where we have integrated in radial coordinates. Note that here the same effective radius t is used to define the extent of the dielectric medium (ions and electrons) and the polarization density: this is an approximation of the model.

(I) Particular solution

We can now start computing the particular solution of Eq. 4.3. Thus, similarly to what we did for the polarization density in Eq. 4.9, we write down $V_p(r_\perp, z)$ by exploiting the periodicity

along the z-axis and the radial symmetry:

$$V_p(\mathbf{r}_\perp, \mathbf{z}) = \int_{\mathbb{R}^2} \sum_{\mathbf{q}_z} V(q_\perp, q_z) e^{i\mathbf{q}_\perp \cdot \mathbf{r}_\perp} e^{iq_z z} d\mathbf{q}_\perp, \quad (4.11)$$

and we substitute it in the left-hand side of Eq. 4.11:¹

$$\begin{aligned} \nabla \cdot [\epsilon^m \nabla V_p(\mathbf{r}_\perp, z)] &= \nabla \cdot [\epsilon^m \nabla \int_{\mathbb{R}^2} \sum_{\mathbf{q}_z} V(q_\perp, q_z) e^{i\mathbf{q} \cdot \mathbf{r}} d\mathbf{q}_\perp] = \\ &= \nabla \cdot [\epsilon^m \sum_{\mathbf{q}_z} \int_{\mathbb{R}^2} V(q_\perp, q_z) i\mathbf{q} e^{i\mathbf{q} \cdot \mathbf{r}} d\mathbf{q}_\perp] = \\ &= - \sum_{\mathbf{q}_z} \int_{\mathbb{R}^2} V(q_\perp, q_z) [\epsilon_\perp^m |\mathbf{q}_\perp|^2 + \epsilon_z^m |q_z|^2] d\mathbf{q}_\perp. \end{aligned} \quad (4.12)$$

Similarly, the right-hand side of the Poisson equation can be written as:

$$\nabla \cdot \mathbf{P}(\mathbf{r}_\perp, z) = \frac{e^2}{L} \int_{\mathbb{R}^2} \sum_{q_z} \left[\sum_a i\mathbf{q} \frac{Z^a \cdot \mathbf{e}_{LO}^a(q_z)}{\sqrt{2M_a \omega_{\mathbf{q}_z LO}}} f(\mathbf{q}_\perp) \right] e^{i\mathbf{q} \cdot \mathbf{r}} d\mathbf{q}_\perp. \quad (4.13)$$

The Fourier transform² of the radial profile is:

$$\begin{aligned} f(\mathbf{q}_\perp) &= \frac{1}{4\pi^2} \int_{\mathbb{R}^2} f(\mathbf{r}_\perp) e^{i\mathbf{q}_\perp \cdot \mathbf{r}_\perp} d\mathbf{q}_\perp = \\ &= \frac{1}{4\pi^2} \int_0^\infty \int_0^{2\pi} r_\perp \frac{h(t - |\mathbf{r}|)}{\pi t^2} e^{i|\mathbf{q}_\perp||\mathbf{r}_\perp| \cos(\theta + \phi)} d\theta dr \\ &= \frac{1}{4\pi^2} \int_0^\infty \frac{h(t - |\mathbf{r}|)}{\pi t^2} 2\pi r_\perp J_0(q_\perp r_\perp) dr_\perp, \end{aligned} \quad (4.14)$$

where we manipulate the argument of the exponential function in order to solve the integral over the angle θ :

$$q_x \cos\theta + q_y \sin\theta = \sqrt{q_x^2 + q_y^2} \cos(\theta + \phi) = |\mathbf{q}_\perp| \cos(\theta + \phi). \quad (4.15)$$

It follows that

$$f(\mathbf{q}_\perp) = \frac{1}{2\pi^2 t} \frac{J_1(t|\mathbf{q}_\perp|)}{|\mathbf{q}_\perp|}. \quad (4.16)$$

Finally we can insert the radial profile in the second term of the Poisson equation (Eq. 4.13), and we get:

$$\nabla \cdot \mathbf{P}(\mathbf{r}_\perp, z) = \left[\frac{e^2}{2\pi^2 t L} \int_{\mathbb{R}^2} \sum_{q_z} \sum_a i\mathbf{q} \frac{Z^a \cdot \mathbf{e}_{LO}^a(q_z)}{\sqrt{2M_a \omega_{\mathbf{q}_z LO}}} \frac{J_1(t|\mathbf{q}_\perp|)}{|\mathbf{q}_\perp|} e^{i\mathbf{q} \cdot \mathbf{r}} d\mathbf{q}_\perp \right]. \quad (4.17)$$

¹Note that in the following we drop the index m in the components of the dielectric tensor for the sake of simplicity.

²Note that in the current work we are systematically inserting a factor of $4\pi^2$ when we use the Fourier transform ($r \rightarrow q$) and no prefactor for the inverse transform ($q \rightarrow r$).

Chapter 4. Infrared-active phonons in one-dimensional materials, their coupling to electrons and spectroscopic signatures

Substituting 4.12 and 4.17 in Eq. 4.3, we obtain the particular solution inside the cylinder (i.e., the 1D system) we were looking for

$$V_p(\mathbf{q}_\perp, q_z) = \frac{2e^2}{\pi tL} \frac{J_1(t|\mathbf{q}_\perp|)}{|\mathbf{q}_\perp|} \frac{\sum_a (i\mathbf{q}Z^a \cdot \mathbf{e}_{LO}^a(q_z)) / \sqrt{2M_a\omega_{\mathbf{q}_zLO}}}{(\epsilon_\perp |\mathbf{q}_\perp|^2 + \epsilon_z |\mathbf{q}_z|^2)}. \quad (4.18)$$

Outside the cylinder, we can simply choose a solution of the corresponding equation, i.e. $\nabla^2 V_p(\mathbf{r}_\perp, \mathbf{z}) = 0$, such that the out-of-plane component of the electric field is continuous at the interface.

(II) Homogeneous solution

It is now possible to proceed to find the homogeneous solution V_h . This solution has to solve the homogeneous Poisson equation:

$$\nabla \cdot [\epsilon \nabla V_h(\mathbf{r})] = 0. \quad (4.19)$$

Once again, exploiting the periodicity of the potential along the 1D axis, we can write:

$$V_h(\mathbf{r}_\perp, z) = \sum_{q_z} V_h(\mathbf{r}_\perp, q_z) e^{iq_z z} \quad (4.20)$$

where the dielectric tensor is the usual one, ϵ^m , inside the material, while outside it reduces to the vacuum dielectric constant, i.e., $\epsilon_0 = 1$ (identity matrix). Substituting into the homogeneous equation written before, we obtain:

$$\frac{\partial^2 V_h(\mathbf{r}_\perp, q_z)}{\partial r_\perp^2} + \frac{1}{r_\perp} \frac{\partial V_h(\mathbf{r}_\perp, q_z)}{\partial r_\perp} = \begin{cases} \frac{\epsilon_z^m}{\epsilon_\perp^m} |\mathbf{q}_z|^2 V_h(\mathbf{r}_\perp, q_z) & \text{if } |\mathbf{r}_\perp| < t \\ |\mathbf{q}_z|^2 V_h(\mathbf{r}_\perp, q_z) & \text{if } |\mathbf{r}_\perp| > t, \end{cases}$$

and the solution is:

$$V_h(\mathbf{r}_\perp, q_z) = \begin{cases} c_1 J_0\left(i\sqrt{\frac{\epsilon_z^m}{\epsilon_\perp^m}} r_\perp q_z\right) + c_2 Y_0\left(-i\sqrt{\frac{\epsilon_z^m}{\epsilon_\perp^m}} r_\perp q_z\right) & \text{if } |\mathbf{r}_\perp| < t \\ c_3 J_0(ir_\perp q_z) + c_4 Y_0(-ir_\perp q_z) & \text{if } |\mathbf{r}_\perp| > t. \end{cases} \quad (4.21)$$

We have now four different constants which we can fix in order to fulfill the electrostatic boundary conditions enumerated above. We can already apply the third enumerated condition (i.e., no divergences in the potential) by considering the asymptotic behavior of Eq. 4.21. Namely, we notice a divergent behavior for $r_\perp \rightarrow 0$ for the solution inside the wire, and for $r_\perp \rightarrow \infty$ as far as the external solution is concerned; both related to the Bessel function of the second kind $Y_0(ir_\perp q_z)$. To constrain the constants, we can exploit the properties of the canonical and modified Bessel functions, that is

$$\begin{aligned} Y_0(-ix) &= iI_0(-x) - \frac{2}{\pi} K_0(-x) \\ J_0(ix) &= J_0(-ix) = I_0(x) = I_0(-x). \end{aligned} \quad (4.22)$$

Thus, the homogeneous solution inside the wire becomes

$$c_1 J_0 \left(i \sqrt{\frac{\epsilon_z^m}{\epsilon_\perp^m}} r_\perp q_z \right) + c_2 Y_0 \left(-i \sqrt{\frac{\epsilon_z^m}{\epsilon_\perp^m}} r_\perp q_z \right) = (c_1 + i c_2) I_0 \left(\sqrt{\frac{\epsilon_z^m}{\epsilon_\perp^m}} r_\perp q_z \right) - c_2 \frac{2}{\pi} K_0 \left(-\sqrt{\frac{\epsilon_z^m}{\epsilon_\perp^m}} r_\perp q_z \right) \quad (4.23)$$

and the only way to avoid the divergent behavior ($K_0(0) = \infty$) is to set $c_2 = 0$. Outside the wire instead we have :

$$c_3 J_0(i r_\perp q_z) + c_4 Y_0(-i r_\perp q_z) = (c_3 + i c_4) I_0(r_\perp q_z) - c_4 \frac{2}{\pi} K_0(-r_\perp q_z) \quad (4.24)$$

and thus we set $c_4 = i c_3$. The final homogeneous solution to the Poisson problem, Eq. 4.3, is:

$$V_h(\mathbf{r}_\perp, q_z) = \begin{cases} c_1 I_0 \left(\sqrt{\frac{\epsilon_z^m}{\epsilon_\perp^m}} r_\perp q_z \right) & \text{if } |\mathbf{r}_\perp| < t \\ -\frac{i2}{\pi} c_3 K_0(r_\perp q_z) & \text{if } |\mathbf{r}_\perp| > t \end{cases} . \quad (4.25)$$

For the sake of simplicity, in the following, we rename $c_3 \rightarrow c_2$.

(III) Electrostatic boundary conditions

In the previous section we treated the divergent behavior of the total interaction potential inside and outside the material, that is the cylinder in our model. We are then left with two more constants (i.e., c_1 and c_3 in Eq. 4.25) which have to be fixed in order to satisfy the remaining boundary conditions: continuity of E_\parallel and of D_\perp . The orthogonal component of the dielectric displacement reads:

$$D_\perp(\mathbf{r}_\perp, z) = \begin{cases} -\epsilon_\perp^m \frac{\partial V_{\text{Fr}}(\mathbf{r}_\perp, z)}{\partial r_\perp} & \text{if } |\mathbf{r}_\perp| < t \\ -\epsilon_0 \frac{\partial V_{\text{Fr}}(\mathbf{r}_\perp, z)}{\partial r_\perp} & \text{if } |\mathbf{r}_\perp| > t \end{cases} , \quad (4.26)$$

while the condition on the the electric field is simply equivalent to impose the continuity of the Fröhlich potential. The two boundary conditions are thus imposed by means of the following set of equations:

$$\begin{cases} V_p^-(t, q_z) + V_h^-(t, q_z) = 0 + V_h^+(t, q_z) \\ -\epsilon_\perp^m \frac{dV_p^-}{dr_\perp}(t, q_z) - \epsilon_\perp^m \frac{dV_h^-}{dr_\perp}(t, q_z) = 0 - \epsilon_0 \frac{dV_h^+}{dr_\perp}(t, q_z). \end{cases} \quad (4.27)$$

This set of equations can be conveniently written in matrix form:

$$\begin{pmatrix} -I_0 \left(\sqrt{\frac{\epsilon_z^m}{\epsilon_\perp^m}} t q_z \right) & K_0(t q_z) \\ -\epsilon_\perp^m \sqrt{\frac{\epsilon_z^m}{\epsilon_\perp^m}} q_z I_1 \left(\sqrt{\frac{\epsilon_z^m}{\epsilon_\perp^m}} t q_z \right) & -\epsilon_0 q_z K_1(t q_z) \end{pmatrix} \begin{pmatrix} c_1 \\ c_2 \end{pmatrix} = \begin{pmatrix} V_p^-(t, q_z) \\ \epsilon_\perp^m \frac{dV_p^-}{dr_\perp}(t, q_z) \end{pmatrix}. \quad (4.28)$$

To solve such system, one needs to Fourier anti-transform with respect to q_\perp the particular solution in Eq. 4.18; this has to be done in order to compare it with the homogeneous one in

Chapter 4. Infrared-active phonons in one-dimensional materials, their coupling to electrons and spectroscopic signatures

Eq. 4.25. The particular solution, Eq. 4.18, once anti-transformed, reads:

$$\begin{aligned} V_p(\mathbf{r}_\perp, q_z) &= \frac{2e^2}{\pi t L} \int \frac{\sum_a (i\mathbf{q} Z^a \cdot \mathbf{e}_{LO}^a(q_z))}{\sqrt{2M_a \omega_{\mathbf{q}_z LO}}} \frac{J_1(t|\mathbf{q}_\perp|)}{|\mathbf{q}_\perp|} \frac{1}{(\epsilon_\perp^m |\mathbf{q}_\perp|^2 + \epsilon_z^m |\mathbf{q}_z|^2)} 2\pi |\mathbf{q}_\perp| J_0(q_\perp r_\perp) d\mathbf{q}_\perp = \\ &= \frac{4e^2}{tL} \int \frac{\sum_a (i\mathbf{q} Z^a \cdot \mathbf{e}_{LO}^a(q_z))}{\sqrt{2M_a \omega_{\mathbf{q}_z LO}}} \frac{J_1(t|\mathbf{q}_\perp|) J_0(r_\perp |\mathbf{q}_\perp|)}{(\epsilon_\perp^m |\mathbf{q}_\perp|^2 + \epsilon_z^m |\mathbf{q}_z|^2)} d\mathbf{q}_\perp. \end{aligned} \quad (4.29)$$

Let us note that the two Bessel functions, $J_1(x)$ and $J_0(x)$, have different arguments (depending respectively on t and r). However, for the specific task of solving the system and setting the constants, we only need to impose the boundary conditions on the specific surface given by $r_\perp = t$. Thus, we compute the value of $V_p(r, q_z)$, and its derivative with respect to the radial coordinate, at $r_\perp = t$. We then get the following result:

$$V_p(t, q_z) = A q_z \frac{1}{2\sqrt{\pi} \frac{\epsilon_z^m}{\epsilon_\perp^m} q_z^2 t} G_{24}^{22} \left(\frac{\epsilon_z^m}{\epsilon_\perp^m} q_z^2 t^2 \left| \begin{matrix} \frac{1}{2} & 1 & - \\ 1 & 1 & 0 \end{matrix} \right. \right), \quad (4.30)$$

where $G_{pq}^{mn} \left(\begin{matrix} a_1, \dots, a_p \\ b_1, \dots, b_q \end{matrix} \middle| x \right)$ is the Meijer G-function, and the constant A in the prefactor of the particular solution reads:

$$A = \frac{4e^2}{L t \epsilon_\perp^m} \sum_a \frac{Z^a \cdot \mathbf{e}_{LO}^a(q_z)}{\sqrt{2M_a \omega_{\mathbf{q}_z LO}}}. \quad (4.31)$$

Then, the derivative of the potential is instead computed as follows:

$$\begin{aligned} \frac{dV_p}{dr}(t, q_z) &= \frac{4e^2}{tL} \int \frac{\sum_a (i\mathbf{q} Z^a \cdot \mathbf{e}_{LO}^a(q_z))}{\sqrt{2M_a \omega_{\mathbf{q}_z LO}}} \frac{J_1(t|\mathbf{q}_\perp|) \frac{dJ_0(r_\perp |\mathbf{q}_\perp|)}{dr_\perp} \big|_{(r_\perp=t)}}{(\epsilon_\perp^m |\mathbf{q}_\perp|^2 + \epsilon_z^m |\mathbf{q}_z|^2)} d\mathbf{q}_\perp \\ &= -q_z A \int \frac{q_\perp J_1(t|\mathbf{q}_\perp|) J_1(t|\mathbf{q}_\perp|)}{(|\mathbf{q}_\perp|^2 + \frac{\epsilon_z^m}{\epsilon_\perp^m} |\mathbf{q}_z|^2)} d\mathbf{q}_\perp = -q_z A I_1 \left(\sqrt{\frac{\epsilon_z^m}{\epsilon_\perp^m}} q_z t \right) K_1 \left(\sqrt{\frac{\epsilon_z^m}{\epsilon_\perp^m}} q_z t \right). \end{aligned} \quad (4.32)$$

Substituting these expressions (i.e., Eq. 4.30 and Eq. 4.32) in the system of equations 4.28 one gets:

$$c_1 = \frac{A}{2 \frac{\epsilon_z^m}{\epsilon_\perp^m} \sqrt{\pi} q_z t} \frac{2\sqrt{\pi} q_z t \sqrt{\epsilon_z^m \epsilon_\perp^m} I_1 \left(\sqrt{\frac{\epsilon_z^m}{\epsilon_\perp^m}} q_z t \right) K_0(q_z t) K_1 \left(\sqrt{\frac{\epsilon_z^m}{\epsilon_\perp^m}} q_z t \right) - K_1(q_z t) G_{24}^{22} \left(\frac{\epsilon_z^m}{\epsilon_\perp^m} q_z^2 t^2 \right)}{\sqrt{\epsilon_z^m \epsilon_\perp^m} I_1 \left(\sqrt{\frac{\epsilon_z^m}{\epsilon_\perp^m}} q_z t \right) K_0(q_z t) + I_0 \left(\sqrt{\frac{\epsilon_z^m}{\epsilon_\perp^m}} q_z t \right) K_1(q_z t)}. \quad (4.33)$$

The constant c_2 is not reported since it is not relevant for the solution inside the wire, which is what we are ultimately interested in.

(IV) Computing phonons and EPIs

Once the system in Eq. 4.28 is solved, in principle we have the final total potential $V_{Fr} = V_p + V_h$

which is the solution to the Poisson equation 4.3. The last step we miss is its integrated value $V_{\text{Fr}}(q_z)$ in the out-of-chain direction. From this, we can finally determine the consequences on phonons and EPC. That said, we will first compute directly the $V_p(q_z)$ without passing through $V_p(r_\perp, q_z)$ (which we understood in Eq. 4.29 to be a far from trivial task) and then we will sum directly $V_p(q_z)$ to $V_h(q_z)$, both integrated separately. Let us start from the particular solution in Eq. 4.18:

$$\begin{aligned} V_p(q_z) &= \int V_p(r_\perp, q_z) \frac{h(t - |r_\perp|)}{\pi t^2} 2\pi r_\perp dr_\perp = \\ &= \frac{4e^2}{tL} \int \int \frac{\sum_a (i\mathbf{q}Z^a \cdot \mathbf{e}_{LO}^a(q_z))}{\sqrt{2M_a\omega_{\mathbf{q}_zLO}}} \frac{J_1(t|\mathbf{q}_\perp|)J_0(r|\mathbf{q}_\perp|)}{(\epsilon_\perp^m |\mathbf{q}_\perp|^2 + \epsilon_z^m |q_z|^2)} \frac{h(t - |r_\perp|)}{\pi t^2} 2\pi r_\perp dr_\perp dq_\perp = \\ &= \frac{4e^2}{tL} \int \frac{\sum_a (i\mathbf{q}Z^a \cdot \mathbf{e}_{LO}^a(q_z))}{\sqrt{2M_a\omega_{\mathbf{q}_zLO}}} \frac{J_1(t|\mathbf{q}_\perp|)}{(\epsilon_\perp^m |\mathbf{q}_\perp|^2 + \epsilon_z^m |q_z|^2)} \left(\int J_0(r|\mathbf{q}_\perp|) \frac{h(t - |r_\perp|)}{\pi t^2} 2\pi r_\perp dr_\perp \right) dq_\perp. \end{aligned} \quad (4.34)$$

The integral in the round bracket is the Fourier transform of the Heaviside step function, that is $\frac{2J_1(t|\mathbf{q}_\perp|)}{t|\mathbf{q}_\perp|}$ so we obtain

$$\begin{aligned} V_p(q_z) &= \frac{8e^2}{t^2L} \int \frac{\sum_a (i\mathbf{q}Z^a \cdot \mathbf{e}_{LO}^a(q_z))}{\sqrt{2M_a\omega_{\mathbf{q}_zLO}}} \frac{J_1(t|\mathbf{q}_\perp|)J_1(t|\mathbf{q}_\perp|)}{|\mathbf{q}_\perp|(\epsilon_\perp^m |\mathbf{q}_\perp|^2 + \epsilon_z^m |q_z|^2)} dq_\perp = \\ &= \frac{8e^2}{t^2L\epsilon_\perp^m} \frac{\sum_a (i\mathbf{q}Z^a \cdot \tilde{\mathbf{e}}_{LO}^a(q_z))}{\sqrt{2M_a\omega_{\mathbf{q}_zLO}}} \frac{1 - 2I_1\left(\sqrt{\frac{\epsilon_z^m}{\epsilon_\perp^m}} q_z t\right) K_1\left(\sqrt{\frac{\epsilon_z^m}{\epsilon_\perp^m}} q_z t\right)}{2\frac{\epsilon_z^m}{\epsilon_\perp^m} q_z^2}. \end{aligned} \quad (4.35)$$

In a similar way, we obtain the final homogeneous solution inside the wire as a function of q_z :

$$V_h(q_z) = c_1 \int I_0\left(\sqrt{\frac{\epsilon_z^m}{\epsilon_\perp^m}} q_z r_\perp\right) \frac{h(t - |r_\perp|)}{\pi t^2} 2\pi r_\perp dr_\perp = c_1 \frac{2}{t} \frac{I_1\left(\sqrt{\frac{\epsilon_z^m}{\epsilon_\perp^m}} q_z r_\perp\right)}{\sqrt{\frac{\epsilon_z^m}{\epsilon_\perp^m}} q_z}. \quad (4.36)$$

Eventually, by summing the particular and homogeneous solutions we get the total Fröhlich potential:

$$V_{\text{Fr}}(q_z) = \frac{2Aq_z}{t} \frac{1 - 2I_1\left(\sqrt{\frac{\epsilon_z^m}{\epsilon_\perp^m}} q_z t\right) K_1\left(\sqrt{\frac{\epsilon_z^m}{\epsilon_\perp^m}} q_z t\right)}{2\frac{\epsilon_z^m}{\epsilon_\perp^m} q_z^2} + c_1 \frac{2}{t} \frac{I_1\left(\sqrt{\frac{\epsilon_z^m}{\epsilon_\perp^m}} q_z r_\perp\right)}{\sqrt{\frac{\epsilon_z^m}{\epsilon_\perp^m}} q_z}. \quad (4.37)$$

By substituting the expression obtained for c_1 , and exploiting an isotropic assumption³ on the

³Note that a similar assumption was done also in the 2D derivation [45] and has been proven to be effective for our scopes.

Chapter 4. Infrared-active phonons in one-dimensional materials, their coupling to electrons and spectroscopic signatures

dielectric tensor ($\epsilon_{\perp}^m = \epsilon_z^m \rightarrow \epsilon_{1D}$), the final results is:

$$g_{\text{Fr}}(q_z) = \frac{4\pi e^2}{\epsilon_{1D}\pi t^2 L q_z} \left(\sum_a \frac{Z_a \cdot \mathbf{e}_{LO}^a(q_z)}{\sqrt{2M_a\omega_{q_z LO}}} \right) \left[1 - 2I_1(q_z t)K_1(q_z t) \right. \\ \left. \left(1 - \frac{2\epsilon_{1D}\sqrt{\pi}q_z t I_1(q_z t)K_0(q_z t) - G_{24}^{22}(q_z^2 t^2)}{2\sqrt{\pi}q_z t (\epsilon_{1D}I_1(q_z t)K_0(q_z t) + I_0(q_z t)K_1(q_z t))} \right) \right], \quad (4.38)$$

where we have termed V_{Fr} as g_{Fr} exactly to highlight that this potential is the one describing the interaction between LO phonons and electrons and thus leading to the Fröhlich EPC; we will come back to this in the following sections. From $g_{\text{Fr}}(q_z)$, in Eq. 4.38, we now have the possibility of obtaining a fully analytical expression for the dielectric shift experienced by the LO phonons. To this aim, following the prescriptions given at the beginning of this section, we compute the Coulomb screened interaction $W_c(q_z)$ as follows:

$$W_c(q_z) = \frac{g_{\text{Fr}}(q_z)}{q_z P(q_z)}. \quad (4.39)$$

From the Coulomb interaction we finally derive the associated dielectric contribution to the dynamical matrix, according to Eq. 4.8, and the final LO frequencies as a function of phonon momentum q_z and radius t :

$$\omega_{LO} = \sqrt{\omega_0^2 + W_c(\mathbf{q}_z) \frac{e^2 |q_z|^2}{L} \left(\sum_a \frac{Z_a \cdot \mathbf{e}_{LO}^a}{\sqrt{M_a}} \right)^2}. \quad (4.40)$$

4.3 Analytical results

So far, by solving the Poisson equation, we have derived two key analytical results: the interaction potential between LO phonons and electrons, and the dielectric shift experienced by LO phonons. After some algebraic manipulation, we managed to highlight a term, in the above expressions (i.e., Eq. 4.40 and Eq. 4.38), that depends on the dimensionality of the material. In other words, we will refer to it, in the following, as the dimensionality signature or fingerprint.

Let us focus first on the central object of the chapter, that is polar-optical phonons and their dispersion relations. In this case, the general expression for a n -dimensional material can be recast in the form

$$\omega_{LO} = \sqrt{\omega_0^2 + \Delta\omega_{\text{max}}^2 \left[1 - \Delta_{\text{nD}}(\mathbf{q}, t) \right]}, \quad (4.41)$$

where ω_0 is the reference value for the LO branch in the absence of any additional contribution from polarity (which can be or be not equal to the TO depending on dimensionality and symmetry considerations). To ease the comparison between dimensionalities, we have highlighted two main contributions: $\Delta\omega_{\text{max}}^2$ and Δ_{nD} . The prefactor $\Delta\omega_{\text{max}}^2 = \frac{4\pi e^2}{\epsilon_i^m \Omega} \left(\sum_a \frac{Z_a \cdot \mathbf{e}_{LO}^a}{\sqrt{M_a}} \right)^2$ corresponds to the maximum value of the shift set by the dielectric properties of the nD crystal. Here, Ω is the volume of material in a cell, i.e., the volume of the unit cell in 3D, or the cell

area times the thickness in 2D, or the cell length times the section in 1D. ϵ_z^m is the dielectric tensor component for the propagation direction $\hat{\mathbf{z}}$ and \mathbf{e}_{LO}^a is the LO eigenvector for an atom a scaled by its mass M_a . This prefactor is then modulated by Δ_{1D} , whose expression depends on dimensionality: it is zero in 3D [40] (corresponding thus to the maximum value of the shift), while dramatically dependent on phonon momenta (in-plane or in-chain) and size t (thickness or radius) in 2D and 1D. The 1D fingerprint is the true novelty provided by the model here presented. If we assume a diagonal and isotropic ϵ_∞ (i.e., $\epsilon^m \rightarrow \epsilon_{1D}\mathbb{I}$), this 1D fingerprint reads

$$\Delta_{1D}(q_z, t) = 2I_1(|q_z|t)K_1(|q_z|t) \left(1 - \frac{2\epsilon_{1D}\sqrt{\pi}q_z t I_1(|q_z|t)K_0(|q_z|t) - G_{24}^{22}(|q_z|^2 t^2)}{2\sqrt{\pi}q_z t (\epsilon_{1D}I_1(|q_z|t)K_0(|q_z|t) + I_0(|q_z|t)K_1(|q_z|t))} \right), \quad (4.42)$$

where $I_n(x)$, $K_n(x)$ are the n^{th} -order modified cylindrical Bessel functions, and $G_{pq}^{mn} \left(\begin{matrix} a_1, \dots, a_p \\ b_1, \dots, b_q \end{matrix} \middle| x \right)$ is the Meijer G-function. Here we mention the limit behaviors. By Taylor expanding $\Delta_{1D}(q_z, t)$ of Eq. 4.41 in the vicinity of Γ , we can extract a ‘logarithmic’ overbending, which goes as $q_z^2 \log(q_z)$, and the 3D limit (i.e., $q_z t \rightarrow \infty$):

$$\Delta_{1D}(q_z, t) = \begin{cases} 1 - q_z^2 t^2 (C(\epsilon_{1D}) - \epsilon_{1D} \log(q_z t)) & \text{for } q_z t \rightarrow 0 \\ 0 & \text{for } q_z t \rightarrow \infty \end{cases} \quad (4.43)$$

where $C(\epsilon_{1D})$ is constant with respect to $q_z t$ but it depends on the dielectric tensor and is equal to $-\frac{3}{4} + \frac{\gamma}{2}(1 - 2\epsilon_{1D}) + \frac{\psi(3/2)}{2} + \log(2)(\epsilon_{1D} + 1)$. Note that the equivalent in 2D would be [41]

$$\Delta_{2D}(\mathbf{q}_\perp, t) = 1 - \frac{\epsilon_{2D} t |\mathbf{q}_\perp|}{2 + \epsilon_{2D} t |\mathbf{q}_\perp|},$$

leading in that case to a linear collapse of the dielectric shift in terms of in-plane phonon momentum \mathbf{q}_\perp . It appears evident that the transition between the two limit behaviors is somehow more complex in 1D with respect to what shown in 2D [41], with $(q_z t)_{\text{critical}} \propto \frac{\text{const.}}{\epsilon_{1D}}$. Eqs. 4.41 and 4.42 are the central analytical result of the model here developed. In particular, Δ_{1D} dictates the transition from a momentum-dependent (1D-like) to a momentum-independent (3D-like) shift, similar to what is observed in 2D [41]. In the $q_z t \rightarrow 0$ limit, $\Delta_{1D} \rightarrow 1$ and the shift breaks down at Γ with an overbending at small but finite q_z [71, 72, 73, 62, 74]. Instead, if considering the opposite $q_z t \rightarrow \infty$ limit, the modulation typical of low-dimensionality vanishes and one is left with the well-known constant 3D shift. The reason behind this transition is intuitive. For small perturbing momenta (real-space long-range interactions), the electric-field lines associated with the polarization density spread far away in the surrounding medium, leading to vanishing dipole-dipole interactions and shift: the material perceives itself as an infinitely thin 1D system surrounded by vacuum. As the momentum increases (short range in real space), these lines get more and more confined within the material and the dipole-dipole interactions eventually resemble those of a bulk material, insensitive to the boundaries.

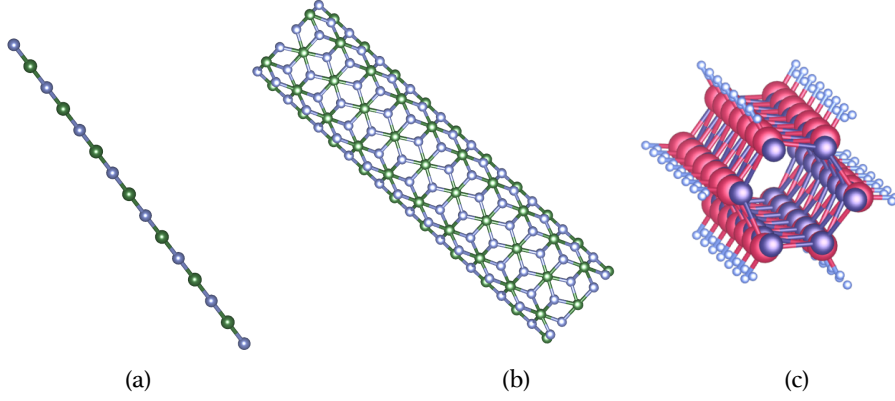


Figure 4.3: Crystal structure of BN atomic-chain (a), armchair BN armchair nanotube (4,4) (b), and GaAs nanowire (c).

Similar considerations are valid for the Fröhlich coupling:

$$g_{Fr}(q_i) = \frac{4\pi e^2}{\epsilon_i^m \Omega q_i} \left(\sum_a \frac{Z_a \cdot \mathbf{e}_{LO}^a}{\sqrt{M_a}} \right) \left[1 - \Delta_{nD}(q_i, t) \right]. \quad (4.44)$$

where, once we fix the direction, i , of the phonon propagation (and thus the relevant component of the dielectric tensor within our model), we find that the prefactor $\frac{4\pi e^2}{\epsilon_i^m \Omega q_i}$ is the same as in the 3D model [44]. Then, the Δ_{nD} carries the same dimensionality signature as for phonons, converging to the bulk 3D limit for $q_z t \rightarrow \infty$, while exhibiting a specific 1D asymptotic behavior in the opposite limit. When this dimensionality term goes to zero we are then left with the well-known 3D like prefactor from the Voigt model [44]. For a similar result and analytical expression for 2D materials, the reader can instead refer to Ref. [45]. The key message here is that this dimensionality contribution we highlighted can have relevant consequences on transport and polaritronics, among other applications, because of this coupling. In fact, the dimensionality term is responsible for a $|g_{Fr}^2|$ which in the long-wavelength limit is known to diverge in 3D, while it tends to a finite value in 2D. From this model we show that it goes to 0 in 1D with a peculiar behavior at small but finite q_z , as will be further discussed in the following section.

4.4 Application to chains, wires and tubes

In this section, we apply our analytical results and the newly implemented 1D-DFT and DFPT methods from Chapter 3 to the following systems: BN atomic chains, armchair BN nanotubes with increasing radii, and GaAs nanowires. Specifically, we demonstrate the impact of our developments on polar-optical phonons and their coupling to electrons, with a view towards understanding their significance in terms of charge transport.

Model parametrization

Before diving into the results, let us comment on the parametrization of the presented model. The analytical results rely on the *ab-initio* parameters obtained independently via DFPT in 1D open-boundary conditions. The implementation of Eq. 4.41, with the 1D signature in Eq. 4.42, requires several physical quantities.

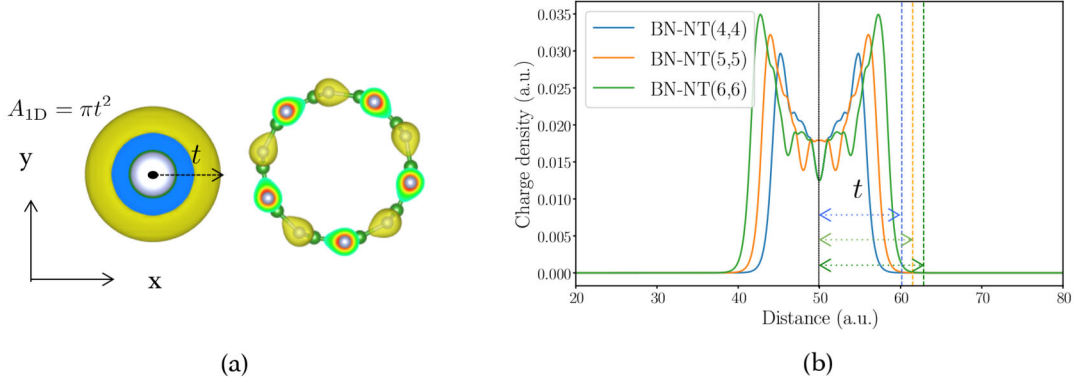


Figure 4.4: In the left panel (a) the radial charge density of, respectively, the BN atomic chain and one BN nanotube are shown. In the right panel (b) we report a schematic representation of how to extract the radius t from the charge density profile. The charge densities shown are obtained by averaging along the chain axis, and plotting in the radial direction. This is done for BN nanotubes of different sizes. A vertical dotted line, for each size, corresponds to the applied threshold.

As discussed also in Chapter 3, masses, eigenvectors, eigenvalues and BECS are directly obtained from the underlying DFT and DFPT calculations. The only exceptions are the effective radius t and the dielectric tensor ϵ^m which, at the end of our derivation, we trivially replaced by the dielectric z-component, and we call it ϵ_{1D} . As discussed in the literature [45, 83, 84, 13, 85, 86, 87, 88, 89, 90], the dielectric tensor concept is ill-defined in nanostructures. More advanced strategies have been proposed to model the response of two-dimensional materials [87, 88, 89, 90] based instead on the polarizability. A particularly fundamental and robust theory has recently been proposed in 2D [51]. In this work, however, modelling the material as a dielectric cylinder implies the presence of a 1D dielectric tensor in our model. It differs from the one computed in QE, ϵ_z^{QE} , which strongly depends on the size of the simulation cell. They are related via effective medium theory [91, 45] as follows. It is clear that the relevant physical quantity is the polarizability (longitudinal and transversal) which characterizes the response of the isolated 1D system per unit of length. This quantity should be preserved in an isolated 1D model and in calculation with periodic images:

$$A_{\text{QE}}(\epsilon_z^{\text{QE}} - 1) = A_{1D}(\epsilon_{1D} - 1), \quad (4.45)$$

where A_{QE} and A_{1D} stand for the cross-sectional area in the unit cell used by QE and in the 1D cylinder model, respectively. In this case, the cutoff is expected to take care of the

Chapter 4. Infrared-active phonons in one-dimensional materials, their coupling to electrons and spectroscopic signatures

depolarization fields coming from the periodic images [85]. The well defined physical quantity is the product $A_{1D}\epsilon_{1D}$. Taken individually, A_{1D} and ϵ_{1D} are just parameters of the model. There is thus a level of arbitrariness in choosing A_{1D} and ϵ_{1D} individually, keeping the product constant. Being mostly interested the long wavelength limit $q_z \rightarrow 0$, we use the $A_{1D} \rightarrow 0$ limit of this equation, while $A_{1D}\epsilon_{1D}$ is constant and determined by first-principles calculations. We then get:

$$\epsilon_{1D} = \frac{c^2}{\pi t^2} (\epsilon_z^{\text{QE}} - 1), \quad (4.46)$$

where c is the out-of-chain length characterizing the supercell geometry (assumed to be the same in the x and y directions). Within our model, t characterizes both the electronic charge density and the out-of-chain polarization density profile. Thus, a reasonable choice to determine this parameter would be to rely on the radial electronic charge density profile, averaged on the cross-sectional planes along the 1D-axis, and set a meaningful threshold (see Fig. 4.4).

An improved agreement of our model with DFPT could probably be obtained, in general, by replacing the isotropic approximation with the full dielectric tensor (i.e., $\epsilon_z^m \neq \epsilon_p^m$). Then, for nanotubes in particular, one could modify the choice made for the shape of the radial polarization density profile $f(\mathbf{r}_\perp)$ in Eq.4.13. In fact, we are here proposing a filled-cylinder model, while nanotubes are more likely hollow-cylinders. The reason why, despite this approximation, the model works so well may be linked to the p_z orbitals pointing inwards and thus filling the cavity of the tube. The smaller the nanotube, the more it should resemble, in this sense, a filled cylinder for our purposes. Nonetheless, since we are interested in the long-wavelength description of polar-optical phonons, the agreement we get in the first tenth of the Brillouin zone is more than satisfactory even for the larger materials, and a further improvement is beyond our scopes.

4.4.1 Polar-optical phonons

We now combine our analytical findings with first-principles calculations within the newly developed 1D framework.

In the following, we focus on BN atomic chains, BN armchair nanotubes, and GaAs nanowires. The scope is threefold: to show the relevance of the open-boundary conditions for linear response in 1D, to validate Eq. 4.42, and to discuss the underlying physics and the transition between dimensionalities. The details of the calculations and model parametrization (also independently obtained via 1D DFPT) are given in Appendix A. For each material we compute the phonon dispersions and we plot it in full in the left panel, zooming around the LO-TO splitting in the right panel (see Fig. 4.5). We focus on the modes similar to those of the bulk 3D or 2D parents, identifying the purest longitudinal mode (hLO), highest in energy and associated to the largest polarization density, as well as the corresponding tangential or bulk-like transverse modes. For clarity, colors are meant to highlight these phonon branches, while the others are left in gray in the background.

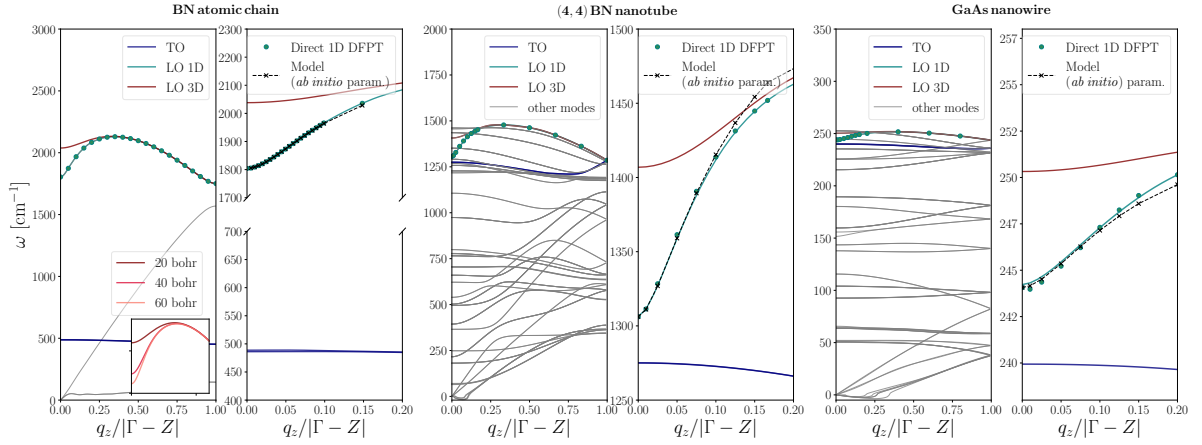


Figure 4.5: Phonon dispersion of BN atomic-chain, (4,4) nanotube, and wurtzite GaAs nanowire of 24 atoms including the hydrogen atoms saturating the surface dangling bonds. For each material, left panel compares 3D-PBC and 1D-OBC DFPT calculations, explicit for 1D (symbols) and interpolated for both (lines). Right panel shows the agreement of our model with 1D DFPT for the LO branch in the long-wavelength limit.

Fig. 4.5 shows the effect of the spurious interactions between periodic images. In 3D DFPT (i.e., 3D PBCs), we always recover a rather flat LO branch (red) with a finite dielectric shift at Γ , which possibly adds up to the splitting with respect to TO phonons (blue) due to crystal symmetries and dimensionality. This is the 3D response of an array of interacting 1D materials. On the contrary, with 1D DFPT (i.e., 1D open-boundary conditions), the amount of energy built by LO phonons (green) is shown to vanish at the zone center and the branch exhibits a logarithmic overbending in the long-wavelength limit: this is the response of the isolated 1D material given by Eq. 4.42. The correction introduced by the Coulomb cutoff is shown to be significant for small q_z , where low-dimensionality comes into play. The Brillouin zone range over which the discrepancy between 3D and 1D DFPT extends is determined by the amount of vacuum in the simulation cell. In PBCs, the larger the vacuum, the smaller the region affected by the stray fields, and the softer the LO branch; this latter asymptotically converges to the 1D limit. This is shown in the inset of the left panel for the BN atomic-chain, where different LO modes, obtained within 3D PBCs, are plotted corresponding to different vacuum choices. The true physical behavior is fully recovered only in the presence of the cutoff, since for momenta smaller than the inverse of the distance between periodic images there will always be the response of a 3D periodic system, i.e., a non vanishing polar shift.

In the right panels of Fig. 4.5 we present the comparison between 1D DFPT and the analytical model we have derived. For all materials, an excellent agreement is found at the very least within the first 10%-20% of the Brillouin zone, that is the long-wavelength limit targeted by the model. The strength of the effect, being the range of frequencies over which the overbending extends, is material dependent and ruled by the square of the screened effective charges, i.e.,

Chapter 4. Infrared-active phonons in one-dimensional materials, their coupling to electrons and spectroscopic signatures

$\frac{Z_a^2}{\epsilon_{1D}}$ (see Eq. 4.41). By comparing the materials in Fig. 4.5, the polar shift is obviously most pronounced in BN: around 200 cm^{-1} in the case of nanotubes, consistently with 2D and 3D hexagonal BN [41, 92, 93], and around 400 cm^{-1} for the chain.⁴ In the BN chain, the larger increase is due to the crystal structure differing from the hexagonal one common to the other allotropes. The effect is more subtle in GaAs, of about 10 cm^{-1} , because of the significantly smaller BECs⁵.

In low-dimensional materials, as a consequence of the vanishing polar shift, the remaining LO-TO splitting at the zone center is purely ‘mechanical’, i.e., due to structurally different atomic displacements because of symmetry and dimensionality. Among the selected materials, the chain represents the ultimate 1D system and exhibits the largest mechanical splitting (i.e., larger asymmetry between displacement directions). Instead, nanotubes and nanowires sit in between 1D and 2D and 3D, respectively, as a function of their diameter. The mechanical splitting at Γ is expected to decrease as $t \rightarrow \infty$, converging to the 2D or 3D case. Similarly, the polar shift asymptotically converges to its higher-dimensional limit. Here, ‘asymptotically’ is key, since the 1D nature of the material will always suppress the polarity-induced electric field at small enough momenta. Thus, the effect of the radius increase is visible in the long-wavelength regime: the range of momenta over which the shift vanishes shrinks and the discontinuity at Γ due to direction-dependent BECs is transferred from the prefactor of the logarithmic overbending (1D) to the slope [41] (2D) or the value [40, 42, 26, 39, 26, 27, 25] (3D) of the polar shift.

Focusing on nanotubes, Fig. 4.6 compares the first-principles results for (4,4), (5,5) and (6,6) BN tubes. In the right panel, decreasing the curvature is shown to stiffen the logarithmic LO behavior and approach the linear signature of 2D materials [41]. The left panel shows instead the absolute values of the optical frequencies for each tube and focuses on the mechanical size effects. There, one can observe two trends. On one hand, it is known throughout the literature that increasing the radius mechanically blue-shifts both TO and LO phonons at zone center [75, 76, 77, 78, 79, 80, 71, 70, 81, 63, 82, 73, 72]. On the other hand, the same radius increase progressively reduces the mechanical splitting, converging towards a finite or null gap depending on the symmetries of the 2D parent (as sketched in Fig. 4.6). Note that the mechanical shifting is much stronger for the TO mode, which can be understood by considering that the atoms are displaced in the non-periodic direction. Furthermore, since the mechanical contribution to the LO shift actually opens the LO-TO gap (pushing LO up), the closing of the gap can be attributed to the stronger increase of the TO frequency. A similar analysis holds for nanowires as well, but in this case the transition is from 1D to 3D. The

⁴The strength of the shift is estimated based on the green curve only (1D OBCs), by considering the difference between the maximum frequency (i.e., $q_z \approx 0.25\%$ of the BZ, where the transition towards a 3D regime happens) with respect to the Γ value (i.e., 1D null shift).

⁵As a consequence of the pseudopotentials used in this work, the GaAs frequencies of the nanowire are strongly underestimated. The actual range of the polar effect should be approximately 20 cm^{-1} . However, here the focus is mainly on the qualitative trend of the polar effect more than the exact frequencies. Note that different pseudopotentials are instead used for bulk GaAs to compare with experiments in the following section and these lead to phonon frequencies in agreement with the literature.

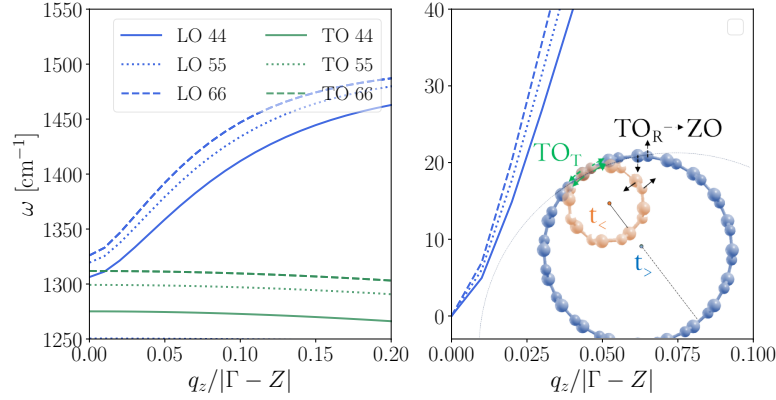


Figure 4.6: Size effects (mechanical and polar) on LO and TO modes for BN (6,6), (5,5) and (4,4) armchair nanotubes from 1D-DFPT. Right panel compares both modes. Left panel focuses on the polar shift for the LO branch by setting as common offset $\omega_0 = 0$. The sketch represents the mechanical evolution of tangential TO_T vs radial TO_R optical modes.

mechanical effects are shared with nanotubes, depending only on crystal symmetries. As regards the dielectric shift, the range of momenta over which the splitting goes from zero to its constant 3D value progressively shrinks around Γ , the dispersion becoming progressively steeper and only asymptotically approaching the well-known discontinuity in the bulk.

4.4.2 Electron-phonon interactions

The interaction of electrons with phonons is also dramatically shaped by materials dimensionality. In this regards, one major example is the Fröhlich interaction discussed in the previous section. Because of the LR nature of the Coulomb interaction, this coupling presents a clear dimensionality signature to simulate which our implantation Coulomb cutoff is crucial. The limit of $\mathbf{q} \rightarrow 0$ of the Fröhlich interaction is known to diverge in 3D [44], while it tends to a finite value in 2D [45]. To our knowledge, similarly to the case of polar-optical phonons, this effect, to date, had not been clarified in 1D systems yet. In this regards, our developments (both analytical and in terms of simulation) can provide novel physical insights.

Here we apply our developments to the simplest yet instructive system in our portfolio, the BN chain. The dispersion relations for small-momentum LO phonons were already shown in the second panel of Fig. 4.5. We focus on how this mode couples with electrons in the system by considering phonon-scattering of an electron from an initial state $|\mathbf{k}_i\rangle$ to a final state $|\mathbf{k}_i + \mathbf{q}\rangle$ within a given band n (i.e., intraband scattering only). Namely we restrict our analysis to the conduction and valence bands with initial states being at the Γ and Z points, that is respectively at the center and edge of the BZ. The EPC matrix elements are defined in DFPT as proportional to the potential perturbation induced by a phonon displacement of

Chapter 4. Infrared-active phonons in one-dimensional materials, their coupling to electrons and spectroscopic signatures

atom a in direction i :

$$g_v^{\text{DFPT}}(\mathbf{q}_z) = \sum_{a,i} \frac{\mathbf{e}_v^{a,i}(\mathbf{q}_z)}{\sqrt{2M_a\omega v(\mathbf{q}_z)}} \langle \mathbf{k}_i + \mathbf{q} | \Delta_{\mathbf{q}_z}^{a,i} \mathcal{V}_{\text{KS}}(\mathbf{r}) | \mathbf{k}_i \rangle, \quad (4.47)$$

where \mathcal{V}_{KS} is the lattice periodic part of the Kohn-Sham potential.

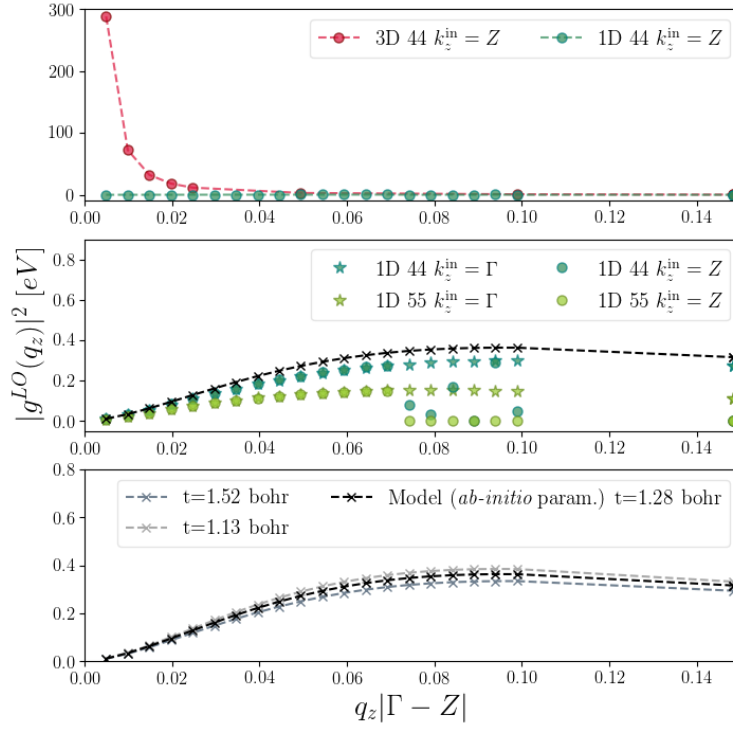


Figure 4.7: EPC matrix elements obtained from DFPT for LO phonons. We consider only intraband scattering within the valence or conduction band near Γ and Z . In red we report the results for the standard QE code, relying on 3D PBCs, and in green the ones obtained within 1D-DFPT. Last, we plot our analytical model on top of explicit DFPT results.

Our *ab-initio* results, specifically focusing on Fröhlich coupling, are presented in Fig. 4.7, where we compare, as we did for polar-optical phonons, the 3D PBCs with the novel 1D OBCs. The results obtained from the two codes show very different trends for the small momenta limit of $|g^{\text{LO}}(\mathbf{q})|^2$. When periodic images are included, that is in 3D PBCs, the Fröhlich interaction diverges as $\mathbf{q} \rightarrow 0$, which is exactly the behaviour expected in 3D bulk materials [44]. This divergence appears no matter the amount of vacuum in the simulation cell, i.e., the separation between the images, and is dictated by the non-vanishing spurious cross talks between the periodic copies. Once again, the larger the vacuum, the closer one asymptotically gets to the isolated case. This isolated case, that is the response from the isolated 1D system, is however recovered only thanks to the Coulomb cutoff. In this case the coupling with LO phonons exhibits a more complex and non-monotonic behavior with respect to both 3D and 2D materials. In particular, $|g^{\text{LO}}(\mathbf{q}_z)|^2$ goes to 0 at Γ while it reaches a maximum at small

momenta and then converge to the 3D limit for larger momenta, i.e., vanishing values.

This trend is confirmed by our analytical model as shown in the second panel of Fig. 4.7. Note that the $g^{LO}(q_z)$ from the model actually represents the average potential generated by LO phonons and felt by the electrons inside the material, thus losing the information about the dependence on the initial and final electronic states considered instead in DFPT calculations. In this sense, the comparison between first-principles calculations and our analytical results is not as quantitative as in the case of phonons, and depends in a more delicate way on the choice of the radius t with respect to what observed for phonons. However, this comparison is still enlightening in showing that the qualitative trend characterizing this coupling is confirmed, and the position of the peak, being at finite but small q_z is only slightly dependent on t . This information is crucial and can lead to key consequences for several technological application, including transport, where the longwavelength coupling of electrons to LO phonons is often the main limiting factor in polar semiconductors and insulators.

4.5 Experimental relevance

Once the relevant parameters in Eqs. 4.41, 4.42 are known, empirically or from first-principles, our model provides us with a one-to-one relationship between first-order LO Raman/infrared lines (i.e., frequencies) and radius t of the 1D material. In other words, the model promises to become a valuable tool for spectroscopic characterization. Notice that the phonons probed in experiments are those characterized by small but finite momentum q_z , depending primarily on the laser wavelength λ by momentum conservation law ($q_z = 2\pi/\lambda$). Thus, the larger the λ , the closer to Γ is the q_z probed. On top of this, it is well known that when the crystals size is reduced to the nanoscale, the momentum selection rule of the first-order Raman spectrum is relaxed, thus allowing additional phonon scattering away from the zone center and an overall broadening of the spectrum. In addition, the non perfectly mono-chromatic nature of the laser (dependent on the type of source used) affects the set of q_z phonons effectively excited and thus contributing to the final spectrum. Temperature and laser heating are also crucial parameters affecting the final spectra. As a consequence of all these factor, the long-wavelength behavior of the LO mode, which in 1D dramatically depends on momentum at variance with the 3D case, joint with the relaxation of Raman selection rules, makes extremely delicate yet crucial to account for this finite q_z contributions when investigating experimental spectra of nanomaterials. In this respects, the proposed model could be an important ally to support and complement these kinds of experiments. It is important to specify that the comparison between theory and experiments is justified only if the nanostructures are isolated. In fact, isolated materials are needed to avoid cross-talks between the systems in the array. This happens if the spot size of the laser is comparable to the inter-systems distance, and/or for every phonon q_z smaller than the inverse of this distance.

Now we would like to explain how the analytical model can be turned into a tool to complement and interpret photon scattering experiments on a variety of 1D systems. To this aim, we

Chapter 4. Infrared-active phonons in one-dimensional materials, their coupling to electrons and spectroscopic signatures

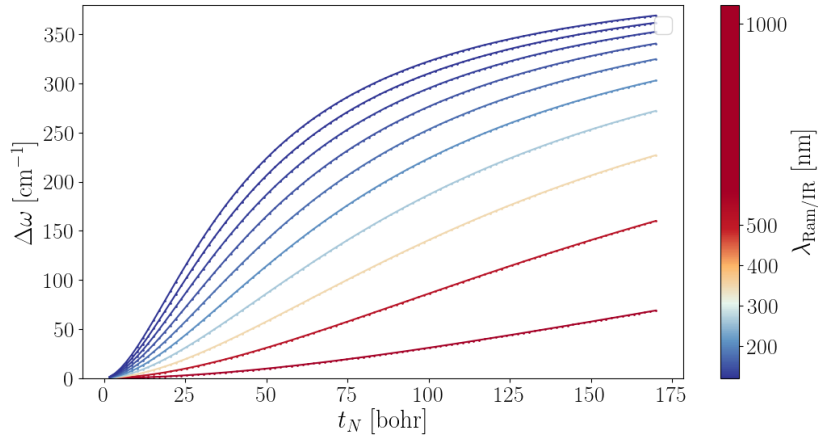


Figure 4.8: Evolution of the LO branch as a function of the radius of the BN chain (toy model) obtained by the model. The color bar indicates different Raman/infrared wavelengths in experiments.

consider first a toy model, a sort of *gedankenexperiment*, and then we compare to the actual experiment which inspired this work in the first place [1]. Let us start from an instructive toy model. Fig. 4.8 shows the evolution of the hLO mode with size for the BN atomic chain, modified by progressive addition of atomic shells around its axis. This evolution is given by Eq. 4.41, where size effects are conveyed by the radius explicitly appearing in the $\Delta_{1D}(q_z, t, \epsilon_{1D})$ term. Note that the dielectric properties and the absolute positions of LO/TO modes may actually change with size due to mechanical reasons, as well as the q -dependency of the eigenvectors. We emphasize that the roles of t and q_z in Δ_{1D} are symmetric (i.e., Δ_{1D} depends on the product $q_z t$). Thus, the behavior of the frequency versus size $\omega_{LO}(t)$ at fixed phonon momenta is the same as the phonon dispersion $\omega_{LO}(q_z)$ at fixed radii and the presented plot is indeed similar to the standard phonon dispersion with the difference that, instead of the phonon momentum q_z across the Brillouin zone, on the x-axis we have a possible range of radii. The color-bar corresponds to the experimental laser wavelength λ which is related to the probed phonons by momentum conservation law (i.e., $q_z = 2\pi/\lambda$). The larger the λ , the closer to Γ is the momentum probed. By increasing t , the logarithmic overbending gradually stiffens and tends to align parallel to the energy-axis, while the short-wavelength part of the ‘branch’ becomes progressively flatter and wider, asymptotically converging to the 3D limit given by $\Delta\omega_{3D}$. These considerations are fully in agreement with what we found for nanotubes from DFPT, as shown in Section 4.4.

As a general comment, in Section 4.4 the model has been shown to perform remarkably well for different 1D prototypes (chains/tubes/wires) and different sizes. In this sense, the only caveat if one wants to use it as a complementary tool for Raman and infrared experiments is the accuracy of the parametrization: radius, BECs, dielectric tensor, eigenvectors and reference frequency ω_0 . Depending on the size of the system, two possible strategies are viable. When dealing with small radii (such as for the BN chain above), whose dielectric and

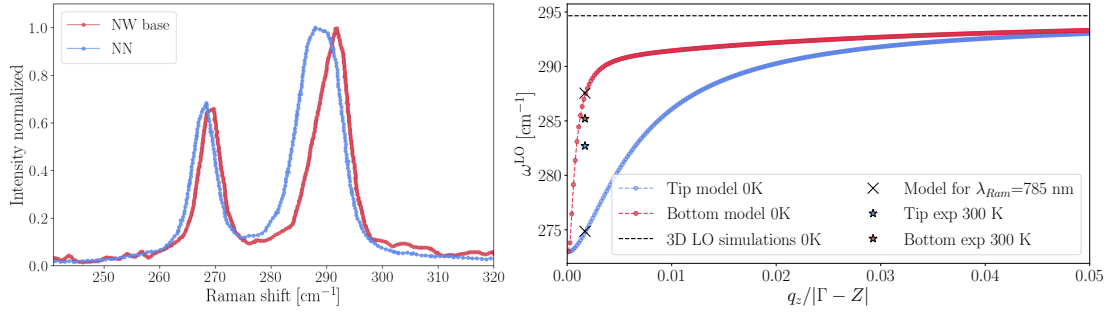


Figure 4.9: Evolution of the LO branch in the long-wavelength limit for the two GaAs nanowires from Ref. [1] (10 and 100 nm in radius) obtained by the model. The comparison with experiments [1] is reported.

mechanical properties are expected to differ significantly from the ones of the bulk parent, the parametrization is more delicate and computationally expensive. In fact, DFPT gives access to the above parameters at the cost of a single Γ calculation except for the q -dependency of the eigenvectors. These eigenvectors, away from Γ , lose more or less rapidly their LO character depending on the size; thus additional DFPT calculations for all the needed q -points involved in the spectrum are in principle needed, and in practice this is crucial for smaller systems. On the other hand, for larger systems closer to bulk conditions, e.g., the nanowires from Ref. [1] a different approach can be more convenient. This basically consists in assuming that the mechanical and dielectric properties required by the model are the same with respect to the bulk 3D or 2D parent and can be extracted from a single phonon calculation at the zone center. In this case, as commented in the main text, the mechanical size-effects are only ruled by the symmetries, and the dielectric effects are fully conveyed by the radius explicitly appearing in the long-wavelength modulation $\Delta_{ID}(q_z, t)$.

In order to validate the model, we would need Raman/infrared experiments on single, isolated and semiconducting wires/tubes. Unfortunately these are mostly missing, and closest to the conditions discussed here is the already cited work of Ref. [1], where the authors propose a new strategy to grow ultrathin GaAs nanoneedles with atomically sharp tips ($t \approx 10$ nm, mostly wurtzite) on top of thicker bases ($t \approx 100$ nm, zincblend). The nanowires are arranged in regular arrays with a spacing of 1000 nm. This distance, compared with the laser spot, is large enough to avoid significant inter-wire cross-talks hindering the response of the single wire. Then, size effects are investigated with room-temperature Raman spectroscopy by pointing a semiconducting laser probe at 785 nm on either the tip or the base. The observed spectra are composed of two peaks each. For the base, the TO and LO modes are found at 268 cm^{-1} and 285 cm^{-1} (LO-TO splitting $\approx 17 \text{ cm}^{-1}$), respectively. The tip spectrum, instead, systematically exhibits, besides broadening, a stable TO mode and a down shift of about 3 cm^{-1} for the LO mode. The observed change in the LO-TO separation, switching from the base to the tip, appears to be almost entirely due to the change in LO position. A mechanical red shift is expected to affect equally the two modes or mostly the TO, which is instead stable. This

Chapter 4. Infrared-active phonons in one-dimensional materials, their coupling to electrons and spectroscopic signatures

points to the dielectric nature of the phenomenon, i.e., the vanishing polar shift and its size dependence. In Fig. 4.9 the hLO mode for the two nanowires as given by the present model is compared with the data from Ref. [1]. We assume both systems to be large enough that we can parameterize (*ab-initio* at $T = 0$ K) Eq. 4.41 using the bulk ϵ^m and BECs, and purely longitudinal and constant eigenvectors. This results in an upper limit in terms of frequencies for each q_z and t . Shrinking the size corresponds to a decrease in the branch steepness close to Γ and to the observed blue shift. The agreement between experiments and the model is very good for the thicker base of the nanowire and semiquantitative with respect to the measured blue shift for the tip. There are multiple plausible reasons behind the discrepancy, such as temperature effects and mechanical contributions (not accounted for in this parametrization), but especially the uncertainty on the phonon momenta probed experimentally. For instance, as regards the temperature impact, the LO (TO) Raman peak at 12 K is reported in the literature to be $293 \pm 1 \text{ cm}^{-1}$ ($271 \pm 1 \text{ cm}^{-1}$) [94] which is in agreement with our predictions at 0 K, while at 296 K is $285 \pm 7 \text{ cm}^{-1}$ ($267 \pm 3 \text{ cm}^{-1}$) [95], closer to Ref. [1]. This could help explaining the few cm^{-1} in excess which separate theory and experiments for the larger base. An additional positive note in this case is that the branch is extremely steep and the steepness seems to match well with the experimental value reported, that is the experimental data lies on the line of the model even if for slightly different q_z . As regards the smaller nanowire (i.e., the tip), the difficulty to focus exactly the laser spot seems to be the most evident explanation behind the discrepancy. In other words, base and tip signals are not fully decoupled. Thus experiments probe effectively a mixture of base and tip phonons and fall in between theoretical predictions for the two nanowires' size. In this regards, further comparison with experiments on single (that is isolated) wires/tubes with constant radius will serve to validate the details of the proposed model.

4.6 Summary

Dimensionality provides a clear fingerprint on the dispersion of infrared-active, polar-optical phonons. For these phonons, the local dipoles parametrized by the Born effective charges drive the LO-TO splitting of bulk materials; this splitting actually breaks down in 2D while up to date has not been addressed in 1D materials yet. In this chapter we developed the missing theory for 1D systems -nanowires, nanotubes, and atomic and polymeric chains. Namely, we detailed the derivation of an analytical model which describes the interplay between the phonon-induced polarization and electronic screening. This model consists in solving an electrostatic problem and its solution requires to account for the correct dimensionality of the system, its reduced periodicity and cylindrical symmetry, as well as to apply the proper electrostatic boundary conditions. From such model, we eventually obtained a fully analytic expression for the long-wavelength dispersion relations of LO modes as a function of both phonon momenta and material size. The key result is thus a logarithmic collapse (symmetric in terms of momentum and size) of the dielectric shift at the zone center. In addition, the same model leads to an other analytic result, the Fröhlich electron phonon coupling, playing a crucial role in transport

as well as polaritronics and several other fields. To support and complement these analytical results, we validate them by comparison with the newly implemented 1D density-functional perturbation theory. Our theoretical developments, presented in this chapter, are available in Ref. [57]. To put this in perspective, the developed implementation gives access to both ground-state and linear-response properties for any kind of 1D systems. Notably, the dielectric properties and the radius of the 1D materials are linked by the present work to these red shifts, opening novel infrared and Raman characterization avenues.

5 Charge transport in 2D gated semiconductors

After having faced some of the challenges, theoretical and methodological, posed by 1D systems, we now shift our attention to the rich realm of 2D materials, the so-called Flatland. As a natural continuation of the 1D effort, our interest in this chapter lies on phonon-limited charge transport. Namely, we focus on electrostatically doped semiconductors, that is materials having an electronic band gap and charged by field effect via planar counter-charges, as it happens in common field-effect setup in experiments. Our ambition here is twofold. On one side, we are drawn to the computational quest for high mobility candidates by exploring large databases of materials. On the other hand, we focus on single materials and we are interested in tuning, or engineering, their transport properties. To pursue these goals, we combine accurate first-principles calculations (i.e., DFT and DFPT, accounting for materials dimensionality and electrostatic doping) with Boltzmann transport theory and an automated discovery workflow powered by the AiiDA materials informatics infrastructure. The ultimate goal of this study goes well beyond pinpointing outstanding candidates for transport applications and optimize their properties; it aims to investigate the role of dimensionality in shaping the electron-phonon dynamics, and identify original and reliable descriptors for these interactions. This could be of particular interest for several applications beyond transport (e.g., thermoelectricity, superconductivity), as well as for future machine learning developments. The chapter starts with a general introduction and the main motivations in Section 5.1. Then it follows a summary of the key theoretical and methodological aspects at the center of the present study, Section 5.2. Major attention is devoted to the actual search for outstanding candidates within the selected database of materials, that is the Materials Cloud 2D database. The details of the database, the screening strategy adopted, and the computational methods are presented in Section 5.3.1. The results follow in Section 5.3.2. The present chapter represents a work in progress, and is part of the future developments following the research presented in this thesis.

5.1 Motivation

After the successful production of graphene in 2004 [96, 97, 98], a significant effort has been devoted over the last two decades to the discovery, synthesis and characterization of novel 2D materials targeting specific technological applications at the nanoscale [20, 17, 99, 100, 101, 102, 103, 104, 105]. This eagerness for discovery has been nourished by the semiconductor industry on one side, and a more general fundamental interest on the other. The Moore's law (1965) [106] initially inspired the race towards downscaling in the attempt of increasing the attainable number of transistors into a single chip by reducing their size. The achieved miniaturization has led to higher performance devices with increased functionality, but also to a major challenge: how to dissipate the heat generated by the electronic components. The accumulated heat can indeed negatively impact the performance and reliability of the devices and is largely attributed to the basic building-block of every modern circuit: the field-effect transistor (FET) [96, 20]. FETs work on the principle of controlling the flow of current in a channel by applying an electric field through a gate voltage. As the channel length decreases and reaches a few tens of nm, the so-called short-channel effects (SCEs) arise. In short, when shrinking the size, the gate control over the channel becomes more difficult, leading to various undesirable effects and mainly to a great amount of dissipated heat. To overcome these undesired effects, one of the most promising strategies is to focus on low-dimensional materials [107, 108, 109, 110, 111]. In particular, after the discovery of graphene, 2D materials have received great attention since they offer several advantages over 3D bulk materials, such as high carrier mobilities (resulting in high switching speed and output current), enhanced tunability, high mechanical strength and, most importantly, an improved electrostatic control. In fact, the reduced thickness of these materials allows a better control of the gate over the channel, reducing the SCEs, the amount of heat dissipated, and improving the overall performance of the devices. At first, graphene held the stage thanks to its novelty and exceptional properties, namely its outstanding mobility [112, 113, 21]. However, it soon became clear that graphene is not ideal as a channel material in FETs. This is mainly due to the absence of a bandgap which makes it difficult to achieve a high on/off ratio in FET and is linked to poor tunability. As a consequence, despite the fact that the potential use of graphene in FETs is still researched, novel alternative materials have also been explored, and particular attention has been drawn to the family of transition metal dichalcogenides (TMDs) [20, 97]. Nowadays, the interest in 2D materials has become more general, that is not restricted simply to FETs, and is linked to the potential benefits deriving from the reduced dimensionality. Besides the small size, materials dimensionality brings indeed the role of an additional degree of freedom dramatically shaping materials properties and often leading to new physics and outstanding electrical, mechanical and optical properties. Moreover, the sensitivity of these properties to external stimulation (e.g., electric and magnetic fields, light, temperature, strain) is relevant for many practical applications whenever a switching mechanism is desirable. Our interest in the discovery and design of novel atomic-thin materials stems from these exciting properties and prospective applications.

5.2 Mobilities from first principles and from Fermiology

Given the excitement and relevance of 2D materials in terms of technological applications, it follows that accurate methods to compute intrinsic (i.e., phonon-limited) mobilities from first principles are vital to the microscopic understanding and engineering of these properties, as well as to find the best candidates for specific applications, including transport. Nevertheless, the computation of transport coefficients is not straightforward; it requires first the description of the electron-phonon interactions (EPIs) and then the solution of the transport equation. In particular, the computation of EPC matrix elements represents a true bottleneck in terms of computational costs. As such, various degrees of approximations are often used at different stages when computing transport coefficients. In this work, our method of choice is the BTE for electrons and holes [34, 114, 48] (see Chapter 1). There, the main ingredients are the EPC matrix elements entering the expression for the scattering rates [34, 115, 116]. These can be computed from first principles within linear response, that is DFPT [26], or with finite-differences schemes [117, 118]. However, similarly to the case of 1D systems discussed in Chapter 3, 3D PBCs used in plane-waves codes introduce spurious interactions in calculations due to the presence of periodic images, thus posing some challenges in dealing with dimensionality and doping. These critical points are yet often neglected in the literature leading to an erroneous description of the long-wavelength electron-phonon dynamics (in particular Fröhlich and piezoelectric scattering) and the inclusion of doping as a mere post-processing step, i.e., frozen band approximation. The latter one is a strong approximation motivated only in the limit of low-doping. A more realistic description has been proposed in the past and consists in a 2D-DFPT framework for gated materials [29]. In terms of BTE, its general formulation does not have a closed-form solution and thus various simplifications have been put forward, consisting in different flavours of the relaxation-time approximation (RTA) [48, 34, 30]. One of the most rudimentary approximation is the constant relaxation-time approximation (CRTA) [119, 120], but there are also intermediate approaches such as the electron-phonon averaged (EPA) approximation [121]. Alternatively, in the attempt of going beyond RTA, more expensive, yet accurate, schemes have been proposed based on either iterative [122, 123, 124] or variational approaches [125, 126] as well as direct diagonalization [127, 128] of the scattering matrix, each with specific drawbacks and advantages.¹

At the macroscopic level, the proportionality coefficient between the measured current density \mathbf{J} in a given material and the applied field \mathbf{E} is the conductivity tensor σ , as described by the famous Ohm law

$$\mathbf{J} = \sigma \mathbf{E}.$$

In the attempt of providing a microscopic description of σ , let us consider a generic 2D material lying in the x-y plane with an applied in-plane electric field $\mathbf{E} = E\hat{\mathbf{u}}_E$. The solution of the BTE that we adopt in the following is detailed in Ref. [48] and relies on a minimum set of approximations (i.e., first order in the electric field, steady state, equilibrium phonon

¹Note that the similarity between electron and phonon BTEs implies that the same solvers can actually be applied generically to either the electron or phonon transport.

distribution and mean free path displacements along the band velocity). Within this formalism, the conductivity –and its inverse, the resistivity ρ – is computed as follows:

$$\sigma = \frac{1}{\rho} = -2e^2 \int \frac{d\mathbf{k}}{(2\pi)^2} (\mathbf{v}(\mathbf{k}) \cdot \mathbf{u}_E)^2 \tau(\mathbf{k}) \frac{\partial f^0(\epsilon_{\mathbf{k}})}{\partial \epsilon} \quad (5.1)$$

where each electronic state is labeled by the band index n (here contracted) and the momentum \mathbf{k} , corresponding to a given $\epsilon_{\mathbf{k}}$ energy and $\mathbf{v}(\mathbf{k})$ velocity. Then, \mathbf{u}_E is the unit vector in the direction of the applied electric field, e is the electronic charge, and $\tau(\mathbf{k})$ represents the scattering time for a carrier from an initial state labeled by \mathbf{k} towards all the possible final states \mathbf{k}' . Finally, f^0 is the Fermi Dirac distribution. The derivative of such distribution plays the role of weighting the electronic states and thus selecting only those within an energy window centered around the chemical level (dependent on temperature and doping conditions, in the following commonly referred to as Fermi level) and few $k_B T$ wide, the so-called thermal layer. In this sense the integral in Eq. 5.1 reduces to a sum over the electronic states identifying the relevant pockets or valleys, α , within the BZ, that is $\int_{BZ} \rightarrow \sum_{\alpha}$. Being ultimately interested in the mobility, in addition to the conductivity, we recall the following relationship from the Drude model [30]:

$$\mu = \sigma / n \quad (5.2)$$

where $n(p)$ is the electron (hole) density as induced by different kinds of doping; in our case moderate or high doping ($10^{12} - 10^{13} \text{ cm}^{-2}$) via field effects, thus turning our pristine material in a system with screening and transport properties intermediate between semiconducting and metallic. Despite being derived within a specific formalism [48], the integral of Eq. 5.1 is instructive in showing what are the main ingredients behind transport. Namely, we can identify two main contributions: carrier velocity and scattering times (in this work related only to electron-phonon interactions). To maximize the conductivity, we need to optimize, that is maximize, both quantities. The velocities projections are uniquely determined by band-structure properties and thus we generally look for small effective masses for the electronic states around Fermi level. On the other hand, the scattering times τ are inversely proportional to the electron-phonon interactions (EPIs) and to the amount of states available for scattering, density of states (DOS). However, the DOS contribution in terms of τ is essentially compensated when summing over the electronic states when performing the integral in Eq. 5.1. For this reason, to maximize τ the most effective strategy is ‘simply’ to minimize the EPI strength.

Based on the position of the Fermi level and the morphology of the valleys, materials can be generally distinguished in two macro categories: single-valley and multi-valley materials. The nomenclature is based on whether one or more valleys lie within the thermal layer relevant for transport. As shown in Fig. 5.1, a zoology of possible situations exists, ranging from single valleys well separated in energy from the others (that is, single-valley materials), to cases in which multiple valley are comparable in energy, thus all contributing to transport. On top of this, the valleys can be shallow or deep, isotropic or anisotropic, and can mix in the k -pace more or less frequently. All these features influence transport, not only in terms of the carrier velocity involved, but also, and in a more subtle way, tuning the type and strength of

the interactions between electrons and phonons. In this respect, it is useful to recall a rather simple and general consideration that will be used as a guideline in the next sections dedicated to the high mobility quest. The reason of the net distinction between single and multi-valley materials reside in the observation that whenever multiple valleys are available for transport across the BZ, one has to consider both intravalley scattering (within each of the valley) and intervalley (between different valleys). Intervalley scattering is one of the most detrimental mechanisms for transport, both because of its intrinsic observed strength and also because it is not affected by screening from the free carriers. In this sense, single-valley materials provide a straightforward prototype of promising candidates for high-mobility applications.

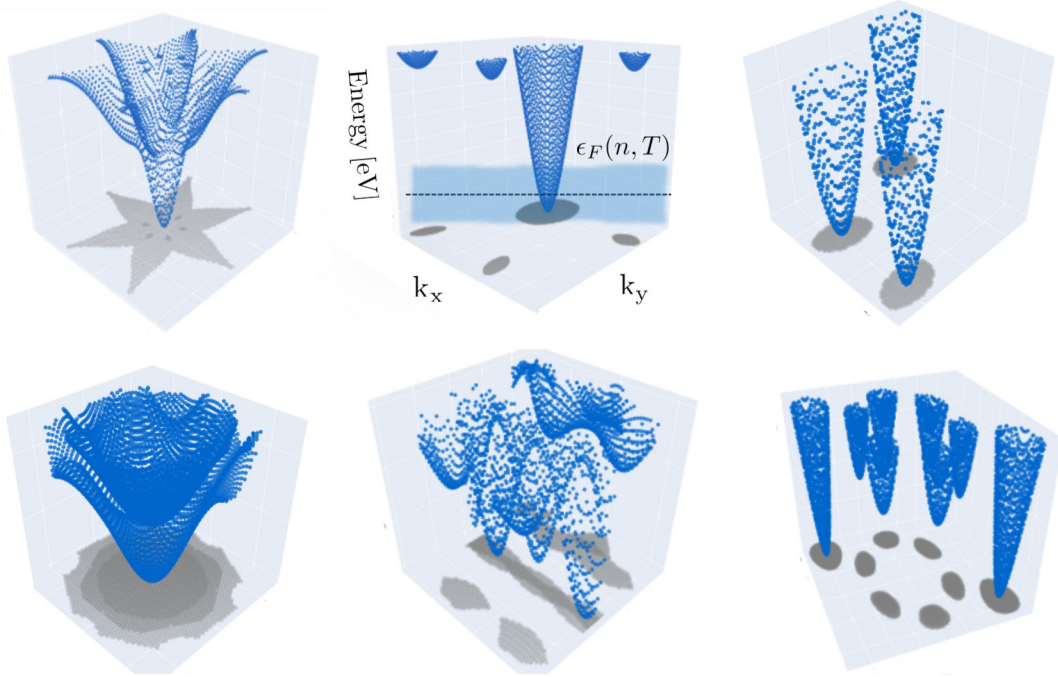


Figure 5.1: Some of the existing valley profiles, differentiated based on the number of valleys, their relative distance in energy (y-axis), their steepness, depth, and degree of anisotropy. These parameters provide crucial information for targeting specific applications.

5.3 The high-throughput quest

Our initial steps in the field of 2D transport focus on the discovery of new materials for high-mobility applications. The general idea behind materials discovery is to combine accurate first-principles simulations, high-throughput (HT) computational approaches, and machine learning algorithms to explore, identify, and design novel materials for a variety of applications.

Here, we combine the former two approaches and focus on phonon-limited charge transport in gated 2D semiconductors, both electron and hole doped. To this end, we improve and extend a previous study [2], exploring the expanded version of our curated portfolio of

2D structures (Materials Cloud 2D database) [17, 129]. This gives us 1205 easily exfoliable candidates to start our new quest. After further restricting the number of candidates, as will be discussed in the following, we combine DFT and DFPT for gated 2D materials [29] with a previously implemented solution, the BTE, beyond the relaxation-time approximation [48]. In the following, we present and discuss the most interesting candidates found so far, as well as the entire discovery workflow powered by the AiiDA materials informatics infrastructure [130, 131, 132].

5.3.1 Database, method and screening strategy

The starting point of our search is the expanded version of a curated set of 2D exfoliable materials derived from the 3D parents (mostly experimentally known) collected in ICSD [133], COD [134], and MPDS [135] databases using vdW correction [17, 129]. This database already contains useful information at the PBE-DFT level, such as the band structure along the high-symmetry path, valley structure across the BZ, and phonon bands. All of this is computed for neutral materials at 0 K temperature, using the 2D-FET version of the QE distribution [29].

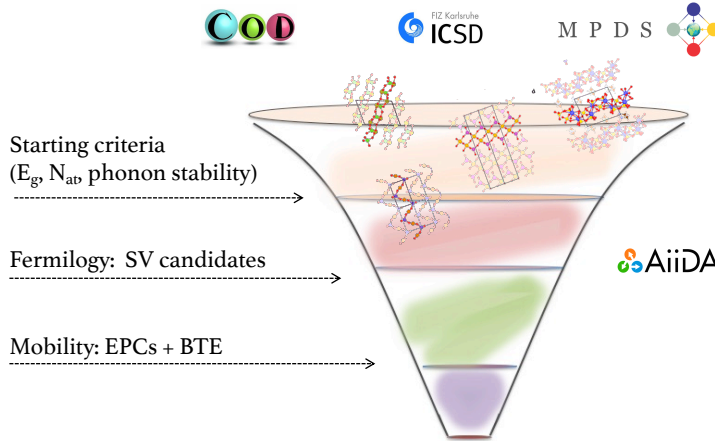


Figure 5.2: Sketch of the computational protocol for the screening of high-mobility single-valley (SV) candidates.

Having in mind the ultimate goal of (i) finding materials characterized by high electron/hole mobilities, and (ii) providing a robust and automated way of screening the database and computing the transport coefficients, we have decided to first focus on single-valley materials. This choice offers the twofold advantage of pinpointing a large portion of the best conductive materials in our database, and at the same time testing and improving the full protocol on a restricted, and thus computationally less expensive, dataset of materials. As briefly discussed in the previous section, selecting only single-valley materials does not automatically guarantee finding the best candidates, but it is a simple yet effective starting point. In fact, even within single-valley materials, there are different and often competing mechanisms that can strongly reduce (or enhance) the electron-phonon EPC and mobility. Similarly, there exist multi-valley

materials that are known to exhibit excellent transport properties for the same reasons. All of this relies on a fragile and delicate balance between valley structures, bare EPC (i.e., not screened), screening, and available electronic states, which are tuned by temperature and doping conditions.

From the original database, we focus on the new additions that are absent in previous studies [2]. We then select only non-magnetic semiconductors (or at least identified as such at PBE level) with a DFT-PBE energy gap $E_g \leq 3$ eV and a number of atoms in the unit cell $n_{\text{at}} \leq 6$. Then, we further reduce the number of candidates for the full mobility calculation² based on fermiology analysis. To this aim, we scan the full dataset and construct a dictionary of relevant properties for each material to identify the most promising candidates. We classify materials based on the Fermi level, the number and degeneracy of the valleys in the relevant energy window, the relative energy position of these valleys (i.e., the depth of the main valley), effective masses, Fermi velocities, and electronic DOS at the Fermi level. This classification is done considering room temperature and high doping conditions, that is 10^{13} electrons/cm², and is based on the valley structure of the neutral candidate already present in the database, thus rigidly shifting the Fermi level across the bands as a preliminary indication. One could, in principle, easily customize these dictionaries by adding the desired information depending on the target. Based on the previous step, we select only single-valley materials for the reasons explained above. For these materials, we further assess their dynamical stability by computing the full phonon dispersion by means of 2D DFPT in both neutral and FET doped cases. Finally, we compute the electron or hole mobilities (depending on the material) by exploiting a workflow powered by the AiiDA infrastructure. A schematic representation of the screening process is reported in Fig. 5.2. Note that relativistic effects due to spin-orbit coupling are neglected here but could actually be relevant for transport depending on the atomic numbers in the compounds. However, this is beyond the scope of the present study.

For a more detailed explanation of the code and tools used to calculate transport coefficients, we refer the reader to Ref. [48]. Here, we briefly review the key aspects of the applied method that has already been developed and the general workflow that we aim to improve. To solve the BTE and obtain the mobilities based on Eq. 5.1, the electronic structure and electron-phonon couplings need to be computed. Therefore, the proposed workflow is divided into two parts: linear response calculation and solution of the BTE. In the first part, the linear response of the system is computed with respect to a given set of phonon momenta selected in such a way as to sample the whole valley. The derived electron-phonon coupling matrix elements, originally reduced by symmetry, are then projected onto the full set of initial states and interpolated on the relevant final ones. These, together with band properties, are the essential ingredients to solve the LBTE, which is the second part of the workflow. To date, the only step that is not automated yet is the sampling of the valleys. The user can choose a grid to select initial and final states across the valleys. The code automatically identifies all the phonons \mathbf{q} that

²Note that at this level of theory and within the proposed computational framework, accurate mobilities require approximately the phonon calculation for 50 momenta \mathbf{q} . If multiple valleys are present, the sampling is more delicate and the number of calculations, and thus the computational cost, increases further.

connect the initial and final states and reduces them by symmetry. However, the choice of the final and initial states depends on the specifics of the valley structure and its single- or multi-valley nature. As a future perspective, we would like to establish a standard protocol such that there is a default choice for the sampling, and no human intervention is required anymore. An example of the sampling procedure is shown in Fig. 5.3 for a multivalley material. The second step, once again interfaced with AiiDA, is the solution of the BTE, which, within this framework, is solved iteratively, accounting for the full dependence of the scattering rates in terms of the energy and momentum of the carriers and without the need for smearing or other computational parameters requiring further convergence tests.

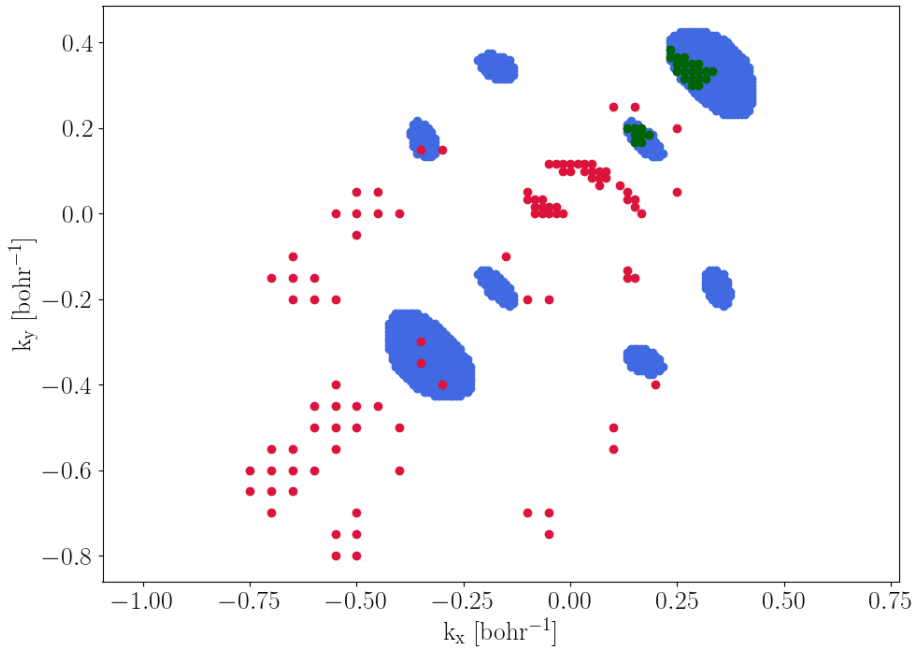


Figure 5.3: Representation of the sampling grid used for transport calculation. The initial electronic states are represented in green, while the final ones in blue, and the phonons which enable these scattering processes in red.

Finally, we would like to acknowledge the existence of numerous HT studies exploring high-mobility materials in both 3D [136] and 2D forms [137]. It should be noted that these studies differ from the one presented here in terms of the materials databases, screening methods, and overall strategies employed.

5.3.2 Results and discussion

We began our screening process with a set of 1205 new 2D structures, which we reduced to 42 semiconductors, while adhering to the aforementioned criteria for the energy gap and the number of atoms in the unit cell. Compared to the original version of the Materials Cloud 2D database [17], our new unexplored additions mainly consist of large materials (i.e., those with a high number of atoms in the unit cell) and metals. As a result, our screening parameters, although not overly stringent, have left us with a relatively small database of materials. Among these, we have identified all the single-valley candidates, including 11 electron-doped and 4 hole-doped materials. Overall, this indicates that single-valley materials are a minority within the database compared to multivalley materials, accounting for approximately 30% of electron doped and less than 20% of hole doped candidates. Note that in this case, the definition of a single-valley material is based on high-doping conditions, i.e., a fixed carrier density of 10^{13} electrons/cm² and room temperature ($T = 300$ K). For higher temperatures or doping levels, more valleys may become populated, thereby transforming the material from single to multiple-valley and activating new scattering mechanisms and channels. For all the selected materials, we conducted a thorough literature search to determine which are already known in the field and which are novel. In the following section, we will review our results and discuss the most interesting candidates.

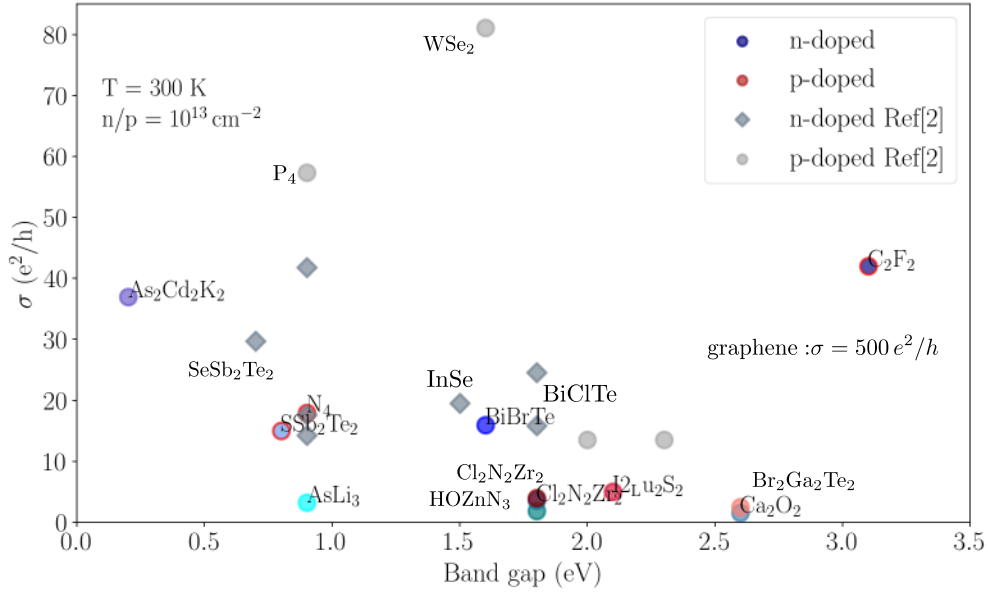


Figure 5.4: Conductivity versus band gap (computed at DFT-PBE/PBEsol level) for the 2D materials selected by our screening. The electron-doped candidates are denoted by blue circles, while the hole-doped ones are shown in red. We also report for comparison the candidates previously selected within the original version of the database as discussed in Ref [2], grey symbols.

As a general overview, we present in Fig. 5.4 the conductivities calculated thus far as a function of the energy gap for both electron-doped (shown in blue shades) and hole-doped (shown in

red shades) candidates. Additionally, we also include, in the background, the results from a previous study [2] in grey. Please note that different screening criteria were used in the previous study. It is important to note that a conductivity value of approximately $10, e^2/h$ is considered to be of interest for practical applications. Unfortunately, graphene, a semimetal, still remains the best material with a reported mobility value of up to $500, e^2/h$ in the best devices. The 11 electron-doped single-valley candidates are: C_2F_2 , $AsLi_3$, $Cl_2N_2Zr_2$, $As_2Cd_2K_2$, SSb_2Te_2 , $BiBrTe$, Ca_2O_2 , $Cu_2Rb_2Te_2$, $Br_2F_2Yb_2$, $I_2F_2Yb_2$ and $OHZnN_3$. The 4 hole-doped single-valley candidates are instead: N_4 , $Cl_2N_2Zr_2$, $Br_2Ga_2Te_2$ and $I_2Lu_2S_2$. Among this small data-set, the most promising ones are found to be C_2F_2 , SSb_2Te_2 , N_4 and $BiBrTe$, while $Cu_2Rb_2Te_2$, $Br_2F_2Yb_2$ and $I_2F_2Yb_2$ are still under ongoing investigation. In the following we focus on C_2F_2 , SSb_2Te_2 and N_4 , highlighted with red circles in Fig. 5.1, to discuss how different ingredients can combine to give high mobility/conductivity (see Tab. A.1 for a summary of the relevant properties computed). The case of $BiBrTe$ also deserves attention, however, despite being more known and discussed in the literature, a full accurate treatment in this case would require the inclusion of SOC which is computationally expensive and thus is still an ongoing effort.

The top candidate we found so far is electron-doped C_2F_2 , also known as fully fluorinated graphene. This structure comes from computational exfoliation of the 3D parent, with the same chemical formula, hosted in the MPDS (Materials Platform for Data Science) database [135] and derived from an experimental structure. The conductivity we found is $42 e^2/h$ with a corresponding mobility above $1000 \text{ cm}^2/Vs$ in the high-doping regime we are exploring here. This material is not new to the literature neither to the field of transport [138, 139, 140, 141, 142, 143, 144]. It has already attracted great attention since chemical functionalization is one of the main strategies proposed to achieve a gap in graphene in the attempt of preserving some of the exceptional properties of the pristine semimetallic material. However, to the best of our knowledge, no ab-initio studies at this level of theory have been reported so far. In this work, fluorinated graphene is found to exhibit an outstanding electron-mobility, which in conjunction with the wide band-gap (3.1 eV at PBE-DFT level) and its tunability, is extremely attractive for electronic devices as well as many other relevant applications. The secret behind such outstanding transport properties lies in the weak electron-phonon coupling characterizing this material. In fact, effective masses and Fermi velocities are among the most important features, in terms of band properties, hinting to high mobilities. Their anisotropy could also play a beneficial role. However, in this case we have relatively large effective masses, moderate velocities at the Fermi level, and a rather isotropic valley-structure, as one can observe from Fig. 5.5, especially if compared with InSe [2] which is the prototypical single-valley candidate for transport, with a steep and deep isotropic valley. Thus, there is no reason a priori to expect exciting transport performances based on fermiology arguments. The reason behind the exceptional results runs deeper and leads to the peculiarity of its electron-phonon coupling. To investigate further, in Fig. 5.6 we plot the interpolated EPC matrix elements across the single-valley in the conduction band. We have one plot for each phonon mode of the system, energetically ordered; this means that modes are not decoupled and thus whenever they mix or cross this reflects into the EPC plots shown. The color bar

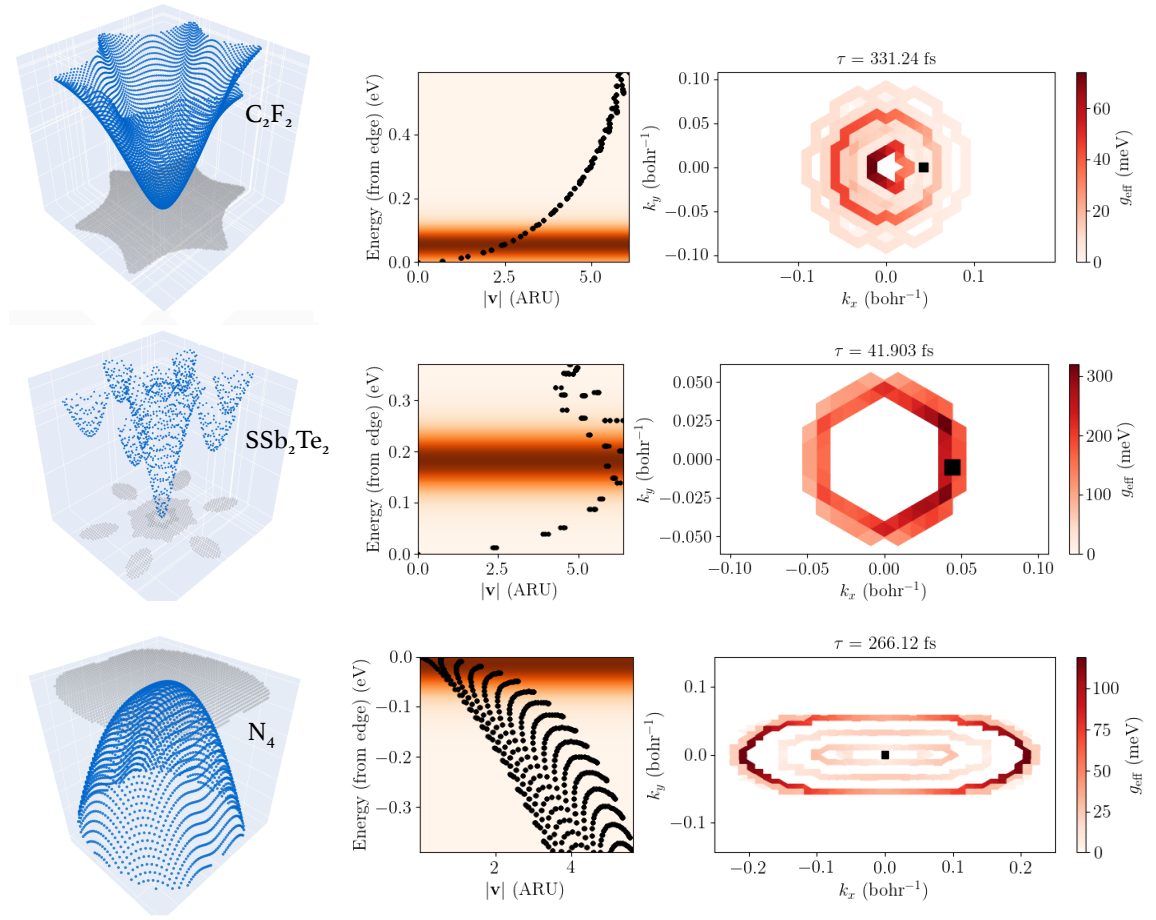


Figure 5.5: We report three plots for each of the selected candidates (C_2F_2 , SSb_2Te_2 , N_4 respectively). In order, we first show (left panel) the structure of the valley relevant for transport. Then, we report (central panel) the ‘velocity plot’ which shows for each \mathbf{k} state in the valley the energy from the band edge versus the norm of the velocity. The red-shaded region identifies the states within the transport energy window ($\partial f^0 / \partial \epsilon$). Last, we show (right panel) the ‘scattering plot’, showing the probability, given by the red color-map, for the initial state (black square) at the Fermi level to be scattered in any other final state within the valley.

represents the strength of the coupling across the valley given an initial state at the bottom of the conduction band at Γ , here represented by a white star. In this case, and for all other candidates presented here, the Fermi level is situated just below the bottom of the valley, near the degenerate regime. As a result, the mobility is expected to be close to its peak with respect to doping. It is a well-established fact that mobility increases with doping and then peaks around the degenerate regime, i.e., when the Fermi level hits the band edge [145]. The existence of a mobility peak with respect to doping is linked to the fact that the enhancement of conductivity σ due to screening and the increased number of electronic states available for transport is eventually outweighed by the inverse dependency of mobility on carrier density,

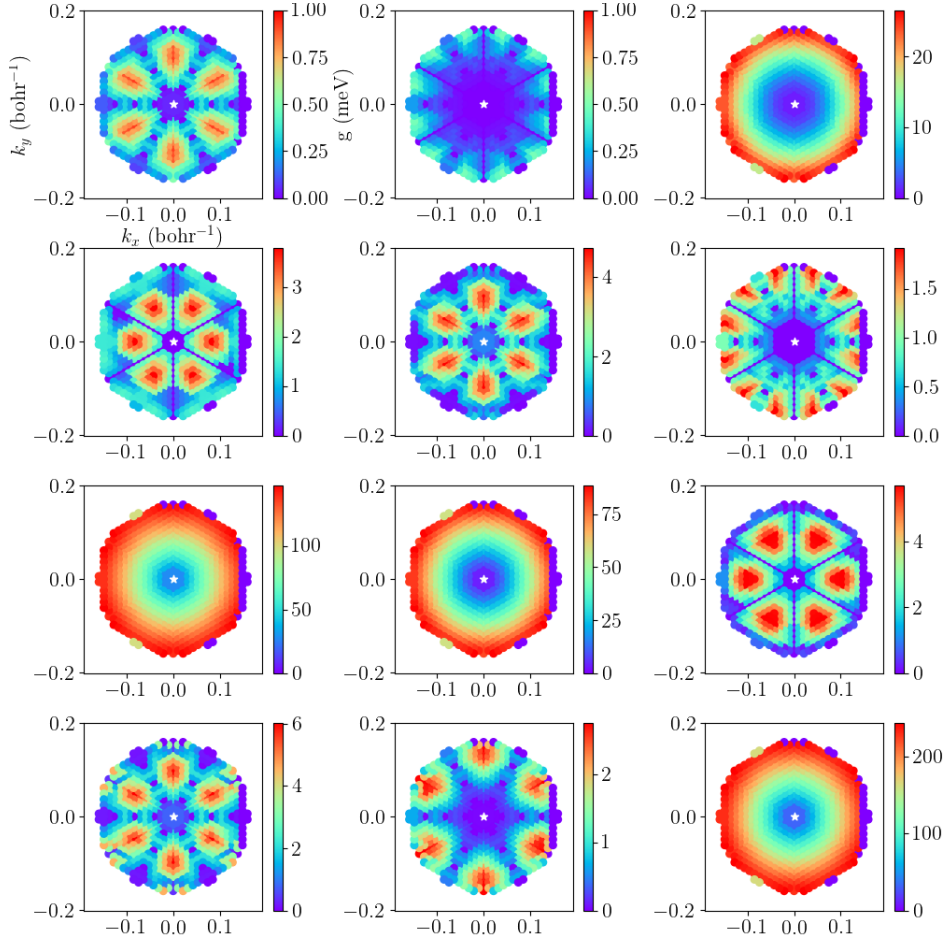


Figure 5.6: Interpolated EPC in C_2F_2 . The color plot show the strength of the coupling by considering an initial electronic state (white star) and all the possible final states covering the full extent of the valley. Each plot represents a different phonon mode considered for the coupling. Phonon modes are ordered based on their energy associated to each transition: from left to right, from top to the bottom. Note that the color scale is different for each plot.

$\mu = \sigma/n$. However, the position of the peak depends on the details of the scattering processes involved. Here we are considering only intravalley transitions, given the single and deep valley structure of C_2F_2 . By looking at the plots it appears that scattering via acoustic phonons is rather weak in this material, while optical modes play a major role as summarized by the 7th and 8th mode. The 12th mode would be the most deleterious for transport but we do not expect it to be populated at room temperature. In a nutshell, we may conclude that, besides its single-valley nature suppressing intravalley scattering, the ingredients behind the high mobility of C_2F_2 are the weak electron-phonon coupling from the acoustic modes, and high-energy optical phonons, thus not significantly populated at the room temperature we are interested in this work.

An other successful output of our quest is electron-doped SSb_2Te_2 , whose 3D parent comes

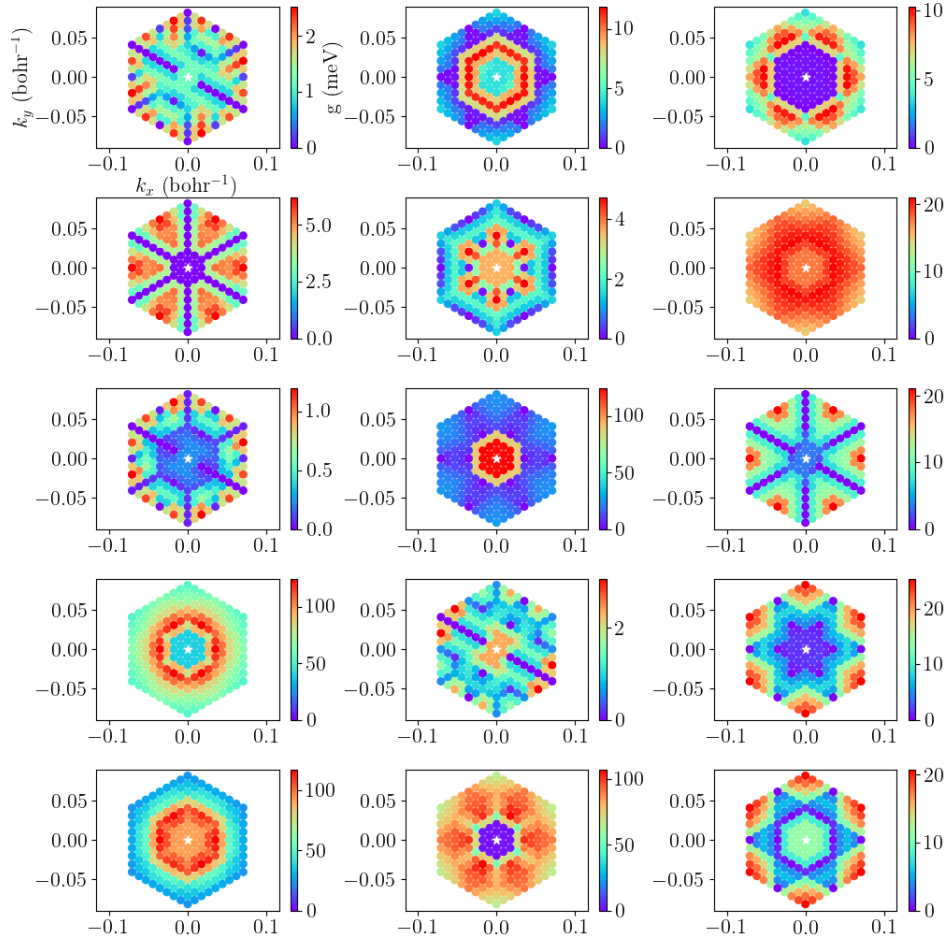


Figure 5.7: Interpolated EPC in SSb₂Te₂. The color plot show the strength of the coupling by considering an initial electronic state (white star) and all the possible final states covering the full extent of the valley. Each plot represents a dieffernt phonon mode considered for the coupling. Phonon modes are ordered based on their energy associated to each transition: from left to right, from top to the bottom. Note that the color scale is different for each plot.

from MPDS as well. In this case the high mobility is the combined result of a promising valley structure on one side and moderate electron-phonon coupling on the other. In terms of valley analysis, this material is characterized by a single and deep valley, leading to moderately high velocities at the bottom of the conduction band, and relatively small effective masses. Similarly to the previous case, the valley is isotropic and the main contribution to scattering comes from center and edge zone optical phonons. Similar considerations are also valid for an other champion identified in this work, As₂Cd₂K₂: outstanding band properties (isotropic and deep, $m^* \approx 0.09 m_e$ combined with moderate EPCs on average to give a significantly high mobility. For this material some refinement calculations are ongoing, thus we do not discuss it here. An interesting observation lies in the fact that in Ref. [2], as shown in Fig. 5.4, e-SeSb₂Te₂ was identified among the interesting candidates. The two materials, belonging to the same family, share strong similarities in terms of both electron and phonon band structures and

EPIs. However, the simple substitution of the heavier selenium atom with the lighter sulfur leads to a decrease of a factor of two on the mobility, and thus on the conductivity. This simple fact raised the question of the role of chemistry in shaping EPC as a results of electron and phonon modifications. We are thus inspired, as a future perspective, to investigate further the key factors for this interaction and link them to chemical and structural properties of materials.

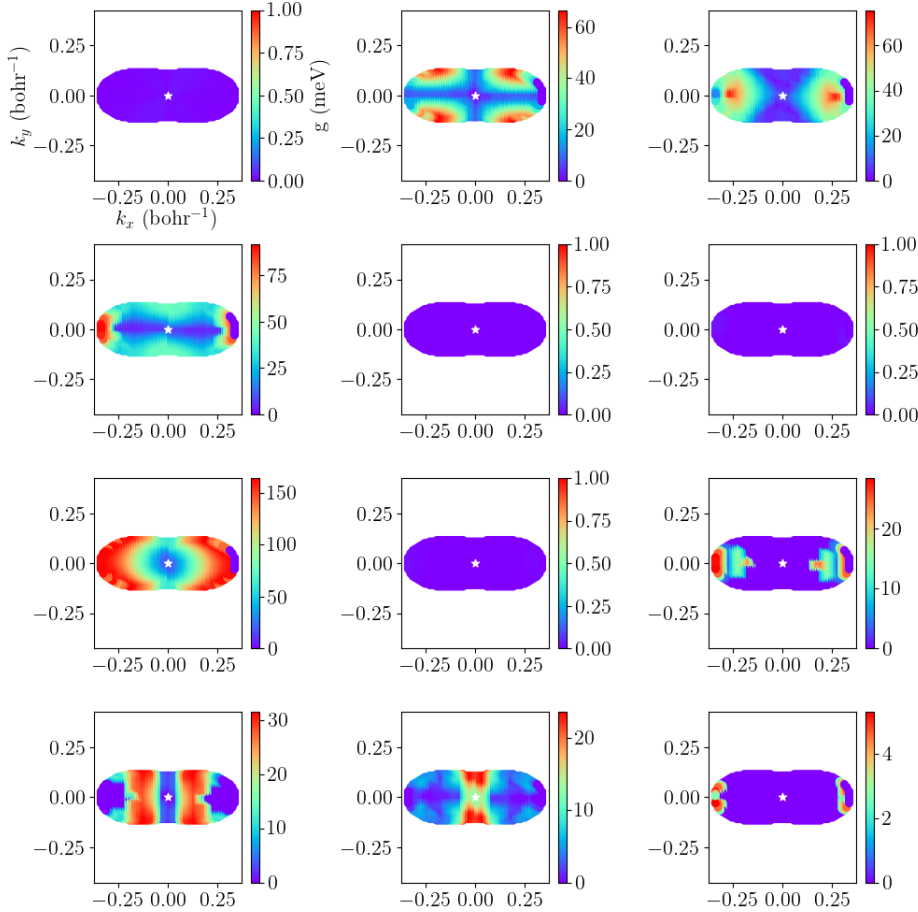


Figure 5.8: Interpolated EPC in N_4 . The color plot show the strength of the coupling by considering an initial electronic state (white star) and all the possible final states covering the full extent of the valley. Each plot represents a different phonon mode considered for the coupling. Phonon modes are ordered based on their energy associated to each transition: from left to right, from top to the bottom. Note that the color scale is different for each plot.

The last candidate represents a different case with respect to the ones previously proposed: N_4 . To start, this material is hole-doped and we focus on the valence rather than conduction bands. Moreover, it is still a single valley material but in this case the valence valley is deep yet anisotropic, reminiscent of the case of hole-doped phosphorene P_4 [2]. Since its discovery, phosphorene has attracted significant attention due to its unique properties, such as bandgap tunability and the anisotropy of its lattice, ductile along one in-plane crystal direction but

stiff along the other. This results in promising mechanical, electronic, optical and transport properties reflecting the same anisotropy. On top of this, besides graphene, P_4 is one of the few monoelemental 2D materials, and this makes it of great relevance for bio-inspired applications besides standard electronics and optoelectronics. Similar structures are known and have partially been investigated, such as antimonene, arsenene, silicene, and germanene; none of them comparable to phosphorene in terms of transport yet. The N_4 structure hosted in the Materials Cloud database comes from a 3D structure in the ICSD database and derives from a theoretical [146] rather than experimental study. Moreover, it is not exactly an analogous of black phosphorene; it is very similar both in the structural and in the electronic properties, though it possess a different point group. Despite experimental studies available for similar structures in the literature [147], it appears to not have been investigated in terms of transport yet, not even theoretically. Thus, given the outstanding conductivity we obtain from our calculations, this material certainly deserves some attention. The key feature that made phosphorene the champion of the previous study[2] is exactly the high degree of anisotropy of its valence valley. This is shared with our structure. The valley anisotropy provides a mechanism to exploit moderate or large velocities along one direction. This direction can then be used for transport, while the large DOS in the opposite direction allows for a high number of electronic states contributing to transport without the risk of filling the valley and possibly activating intervalley scattering. In addition, the other crucial similarity between the two structures, which lies at the origin of their success, is their monoelemental nature. This feature kills the Fröhlich and piezoelectric coupling due to vanishing BECs, mechanisms well known to play a crucial role. If we further explore the EPC plot in Fig. 5.8, we can indeed assess the main contribution to the overall coupling comes from the last two acoustic modes and the first and fourth optical mode, which are scarcely populated at room temperature once again. In addition, the anisotropy of the valley, similarly to phosphorene, reflects in mostly side-scattering, which is not detrimental for transport [2].

2D system	E_g (eV)	ΔE (eV)	v_{e_F} (ARU)	m^* (m_e)	ω^{\max} (cm^{-1})	τ_{av} (fs)	σ (e^2/h)	μ (cm^2/Vs)
$\text{C}_2\text{F}_2 - e$	3.1	4.0	2.3	0.47	1300	331	42	1016
$\text{SSb}_2\text{Te}_2 - e$	0.8	0.407	6.4	0.13	250	41.9	15	360
$\text{N}_4 - h$	0.9	2.6	1.3	-10.38,-0.37	1000	266	17	419

Table 5.1: *Ab-initio* properties computed in this work for three of the best candidates discussed (electron or hole doped). In order, we list the energy gap, the energy separation with respect to the next available valley, the highest carrier velocities at the Fermi level, the effective masses (x and y components, explicitly indicated when non isotropic), the maximum phonon frequency, the average computed electronic lifetime, conductivity and mobility.

5.4 Summary

In this chapter we entered into the realm of 2D materials. We focused on the HT search for semiconducting 2D candidates to target high-mobility applications. To this purpose,

we exploited the Materials Cloud 2D database curated within our group. We focused on the new additions to this database, complementing a previous study. This part of the work had a threefold goal: (i) finding outstanding candidates, (ii) test the machinery and setting protocols and useful guidelines for future studies, and (iii) understanding the physics and design new descriptors. Refinement mobility calculations are still ongoing on the set of selected candidates. We here focused on the most promising candidates identified so far $-C_2F_2$, SSb_2Te_2 and N_4 – and we discussed the key ingredients responsible for their predicted outstanding performances. In doing this, we emphasize the fragile balance and interplay between band properties, phonons and EPIs, competing to determine the mobilities in these materials. The study presented here [148] is only the prelude to a future and larger investigation aiming to scan the whole database of 2D materials in a robust and automated way. Besides the methodological and discovery purposes, the idea is to identify trends and descriptors which could be relevant, besides fundamental science, for several technological application beyond transport. In this regard, the construction of databases of key-properties associated to each material can be a powerful tool at the disposal of the whole scientific community.

6 Engineering mobility by permanent strain: the MoS₂ case

Besides the HT quest for high-mobility candidates, which broadly focuses on the concepts of materials discovery and automation, we are also interested in learning how to engineer the transport properties of a given material. Within this context, it is framed a collaboration with the group of Microsystem Laboratory, led by Professor Jürgen Brugger here at EPFL, aimed at designing and engineering MoS₂ channels for FETs. The basic idea is to induce a permanent strain in the material by depositing it on a corrugated substrate. This is the first time, to our knowledge, that MoS₂ channels have been realized by inducing a permanent strain, paving the way for further developments in the field. On the theoretical side, the complex multi-valley and spin-textured nature of the transition metal dichalcogenides family, to which MoS₂ belongs, calls for tight interactions between the experimental and theoretical communities. The final goal is thus to understand and master the delicate competing mechanisms shaping electron mobility, as well as the ways in which this is affected by the applied strain. This brief chapter begins with an introduction in Section 6.1, while in Section 6.2 we focus on our theoretical contributions. The summary, including key conclusions and future perspectives, follows in Section 6.3.

6.1 Introduction

Transition metal dichalcogenides (TMDs) are a family of layered materials characterized by the formula MX₂, where M indicates a transition metal element from group IV, V, or VI of the periodic table, while X stands for a chalcogen atom. Similarly to graphite, these materials are characterized by atomic bonds that are strong within the plane, while weak in the out-of-plane direction. This is a crucial requirement for exfoliation into 2D crystals. Although they have been known and researched for a long time, recent advances in nanoscale characterization and device fabrication, inspired by graphene, have renewed interest and opened new perspectives. Besides their atomic thickness, TMDs offer a plethora of relevant and intriguing properties – electronic, optical, and mechanical [149, 138, 20, 108, 150]. Among this broad family, MoS₂, MoSe₂, WS₂, and WSe₂ have attracted special attention because they have sizable bandgaps (1-2 eV) that change from indirect to direct when isolating single layers from the bulk structure

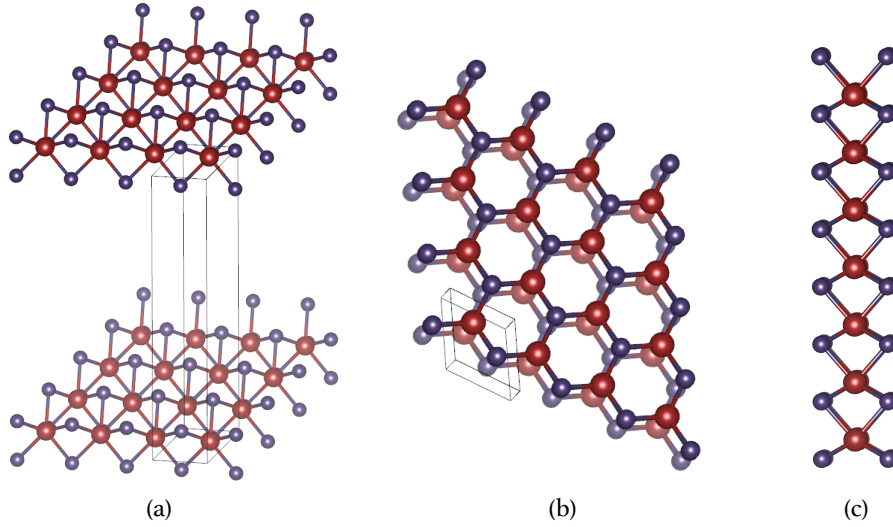


Figure 6.1: Crystal structure of MoS₂, top (a and b panels) and lateral (c panel) views. Mo atoms are depicted in red and S atoms in blue.

[151, 109]. Furthermore, these materials are characterized by the lack of dangling bonds and high mobilities [152, 153, 154, 155, 156, 157] comparable to those of silicon, on which the entire modern semiconductor industry is still based. These features are relevant for many applications, particularly for optoelectronic devices and as channel materials in FETs. In this latter field, TMDs offer an exciting alternative to graphene.

Strain engineering is recognized as a valuable method for tuning the electrical properties of semiconductors and is currently used to improve the performance of silicon-based technology. Inspired by this, the idea behind this project is first to experimentally investigate strain effects on the performance of monolayer MoS₂ channels in transistors, and then to fabricate FETs in which the induced strain is permanent and can thus be fully exploited. Recently, our experimental colleagues succeeded in developing strained monolayer MoS₂ transistors with a nanoscale corrugated surface which features permanent strain and enhanced performance. This is achieved thanks to a newly developed technique in which the 2D channel varies along with substrate topography, and the corrugated substrate is fabricated by thermal scanning probe lithography [158, 159]. So far, the reported measurements show an increase in the electron mobility upon strain. The range of tensile (uniform) strain associated with the corrugations, based on Raman analysis, varies between 0 and approximately 2%, leading to an overall factor 10 of improvement in terms of mobility, up to $\approx 100, \text{cm}^2/\text{Vs}$ in the best devices.

On the theoretical side, our goal is to support the experiments by investigating, from first principles, the effect of strain on the electron mobility of MoS₂ and provide useful insights into the mechanisms responsible for the observed enhancement. To reach such an understanding, we exploit the same computational tools and methodologies introduced in the previous chapter. In short, we combine 2D-DFT and DFPT for gated materials, as implemented within the QE

package, with Boltzmann transport theory. All of this is wrapped into an automated workflow handled by the AiiDA infrastructure (see Chapter 5, and Appendix A) for the computational details). Let us stress once again that in our *ab initio* calculations, we explicitly include the effect of electrostatic doping. The latter is of crucial importance since it allows us to get as close as we can to the experimental conditions in which the material properties and FET performances are investigated.

6.2 Theoretical analysis

Our aim here is to support and complement experiments by shedding light on the microscopic mechanisms governing transport and the role of strain. In fact, straining a generic material is expected to affect its electronic band structure, which could result in alterations of the relative energy positions of the valleys, as well as phonons and electron-phonon dynamics. Therefore, the question arises as to whether the observed improvement in terms of mobility is primarily driven by strain-induced changes in the valley profile or if the effect is more complex and depends on the details of the interaction between electrons and phonons. To answer this, we focused on a systematic comparison of these properties for the strained system (up to 2% tensile strain) with respect to the unstrained structure. Since many factors hinder a quantitative comparison between theory and experiments (as further discussed below), our ambition is to show the qualitative trend of EPC and mobility with respect to the applied strain. Lastly, we set a target electrostatic n-doping of $n = 5 \cdot 10^{12} \text{cm}^{-2}$ and room temperature conditions (i.e., $T=300 \text{ K}$) in agreement with the experiments. Since we are interested in electron doping (n), we focus here on the low-energy valley structure of the conduction band of MoS_2 (two examples for different strain values are shown in Fig. 6.2). This is common to several TMDs and consists of an almost spin-degenerate valley at K/K' (twice degenerate) and a six-fold degenerate spin-split Q valley situated between the K and Γ high-symmetry points. Note that the time-reversal-related valleys (K/K' or Q/Q') have opposite out-of-plane spin polarization, which is captured in our simulations by explicitly including spin-orbit effects.

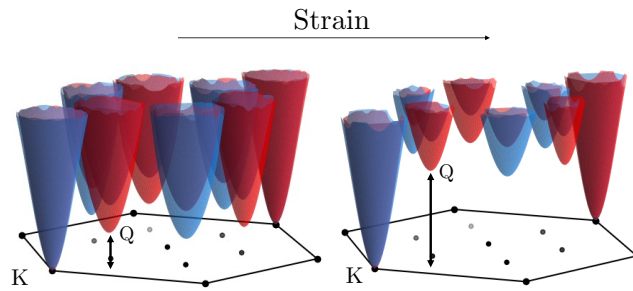


Figure 6.2: Valley profile of MoS_2 unstrained in the first panel (blue), and after applying a tensile strain (red) in the second panel. The arrows indicate the relative energy distances between the K and Q valleys.

It is widely discussed in the literature that charge mobilities in TMDs, including MoS_2 , are

strongly dependent on the details of their complex multi-valley nature and spin texture [145, 160, 161]. Namely, the EPIs are expected to be influenced by the number of valleys that are populated, which ultimately depends on the relative positions of the K and Q valleys and can be further tuned by doping and temperature. The closer the two valleys, the more contributions from intervalley scattering one can expect at fixed conditions. This is known to degrade the mobility of the free carriers as a general trend, both because more states are available for scattering and because the coupling between different valleys is usually rather strong. In this respect, tensile strain is expected to increase the energy separation and eventually isolate the K(K') valleys in such a way that these are the only ones contributing to transport; the Q valleys are not populated and lie too high in energy with respect to the bottom of the conduction band.

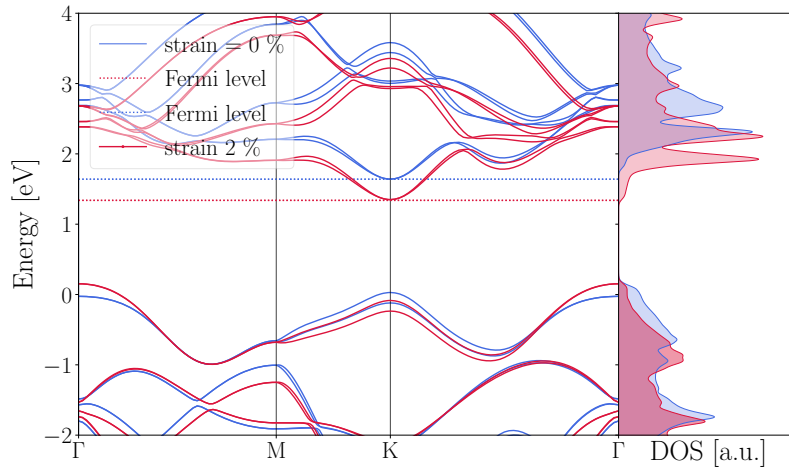


Figure 6.3: Electronic band structure and density of electronic states for the unstrained system (blue) and the 2% tensile strain (red). The zero of energy is set at the top of the valence band for each case: the Fermi level, accounting for doping and electronic temperature, is shown.

Figure 6.2 illustrates exactly the shift mechanism induced by a generic tensile strain in terms of the 3D valley profile. In our calculations, we observe an increase in energy separation ΔE_{KQ} of approximately 200 meV after a 2% strain is applied. This energy shift is large enough to push the Q valleys outside (up) the thermal layer relevant for transport. The same variation can be observed by looking at the band structures in Fig. 6.5. Here, the two band structures are aligned with respect to the bottom of their valence band, and we observe a marked downward shift of the K valley towards the valence band in the strained case, responsible for the above-mentioned ΔE_{KQ} . Also, note that the Fermi level is reported, being located in both cases just below the bottom of the conduction band and thus close to the degenerate case. This hints at the fact that the computed mobility is probably close to its peaked value (see discussion in Chapter 5). Another modification, which has to be taken with care, is the switch from a direct gap in the unstrained material to an indirect one in the strained case. However, this relies on subtle differences in the energetic of the Γ , K, and Q valleys, and strongly depends on the equilibrium structure used in the simulations.

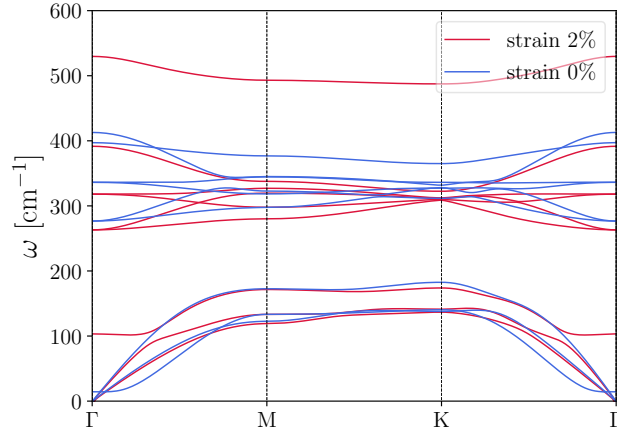


Figure 6.4: Phonon dispersion curves for unstrained MoS_2 (blue) in comparison with the strained case, 2% tensile uniform strain (red).

Similarly to the electronic band structure, phonons are also considerably affected by the applied strain, as shown in Fig. 6.4. The major modifications in this case concern the out-of-plane acoustic mode (ZA) and the optical homopolar mode, which are characteristic for layered structures and correspond to a change in the layer thickness. This is given by the sulfur layers vibrating in counterphase in the direction normal to the layer plane, while the Mo layer remains fixed in its position. Regarding the acoustic modes, the major change concerns center or edge zone phonons, thus mainly affecting intravalley scattering. On the contrary, the optical homopolar mode experiences a drastic rigid blue shift of approximately 100 cm^{-1} across the whole BZ, which is expected to significantly affect intravalley scattering as well.

In terms of EPC, the analysis becomes more complex. However, it is well-established [145, 162, 156, 157], and confirmed by our present results, that acoustic phonons are the main contributors to transport. Not only is their coupling with electrons among the most relevant, but, at room temperature, they are also the only ones significantly populated. To confirm this, we solve the BTE by including only the three low-energy modes corresponding to the acoustic displacements, and we find that these modes contribute almost 80% of the total value of the mobility. Of course, this is just a qualitative check, since the overall BTE solution cannot be trivially decoupled as a sum of contributions from each mode. Motivated by this, we further focus on the EPC plots only for the three acoustic modes (which are well separated in energy from the others and thus we can isolate the plots), shown in Fig. 6.7. By looking at these plots, it seems that the largest variation concerns the third phonon mode which, after strain, couples to electrons up to one order less strongly (this depends if we consider the initial electronic state to be in the K or K' valley). By looking at these plots, it seems that the largest variation concerns the third phonon mode, which, after strain, couples to electrons up to one order less strongly (this is the case if we consider the initial electronic state to be in the lowest K valley). This mode corresponds to the shifted ZA under strain. The other variations are subtle and non-intuitive due to the crossing of low-energy phonon modes. In general, we can

observe that intervalley scattering is suppressed in the strained system, as expected, where mainly long-wavelength and zone edge phonons still couple with electrons, thus potentially hindering transport. The reduction in ZA coupling is finally reflected in an overall increase in mobility from the unstrained to the strained case of about 15%, i.e., from 450 cm²/Vs to 520 cm²/Vs.

Overall, we conclude that the increase in the computed mobility in the strained material is mainly due to variations in phonons and EPC, dictated by ZA phonons and their coupling to electrons. However this does not lead to dramatic consequences in terms of transport, i.e., only 15% increase in mobility for the higher strain considered. The fact that we do not get an increase significant as the one in experiments can be explained since, even in the pristine unstrained system, the DFT equilibrium structure corresponds to a large energy separation between K and Q valleys of 220 meV. This means that, even if the Q valleys fall in the thermal layer, they are not expected to be significantly populated, and thus they will contribute scarcely to transport in either case, strained or unstrained. In this respect, it is important to highlight that the exact energy of the valleys, in TMDs in particular, is extremely sensitive to a number of parameters in *ab-initio* simulations (pseudopotentials, exchange-correlation functional), and namely on the details of the equilibrium structure, as well as the characteristics and details of the experimental setup (substrate, contacts...). Experiments on the energetic of the K and Q valleys in MoS₂ are rare, but it is commonly understood that ΔE_{KQ} is smaller with respect to what we obtain in DFT and in the present work. Such a smaller energy difference between the valleys, to start, could explain the exceptional increase found by our colleagues. In that case, the pristine mobility would be much lower due to the important effect of intervalley scattering, which is underestimated in this work as a consequence of the erroneous energy. This is in agreement with what is suggested in a recent work [145], providing a tool to estimate, based on doping and thickness (which could easily be substituted with strain), the relative position of the valleys, and as a function of such position, the final mobility.

To push our theoretical analysis further and support the experimental results, we perform the same calculations presented above, but taking as a reference structure the experimental one [163], which corresponds to the the correct ΔE_{KQ} . The idea is to first quantify the shift of the position of the Q valley with strain. For this, we use the experimental structure [163] and we determine a reference value for the unstrained case: $\Delta E_{KQ} = 340$ meV. We then evaluate the evolution of ΔE_{KQ} with strain. Unfortunately, the relaxation of out-of-plane atomic positions, which is essential for strain calculations, leads to an increase of ΔE_{KQ} even before applying any strain to the structure. Thus, we evaluate the *variation* of ΔE_{KQ} with respect to the *relaxed* unstrained case (the starting point is the experimental structure), and apply this to the Q-valley position of the *unrelaxed* experimental structure. We apply a tensile uniform tensile strain from 0% up to 2%. In Fig. 6.5 we report the electronic band structure and density of states for different strain values, i.e., 0, 0.5, 0.8, 1, 2%. There, all structures are relaxed. The bands structures, in this case, are aligned with respect to the bottom of the conduction bands, that is the K valley, and we observe a marked upward shift of the Q valley upon strain (with a linear trend), responsible for the mentioned ΔE_{KQ} increase of approximately 300 meV for

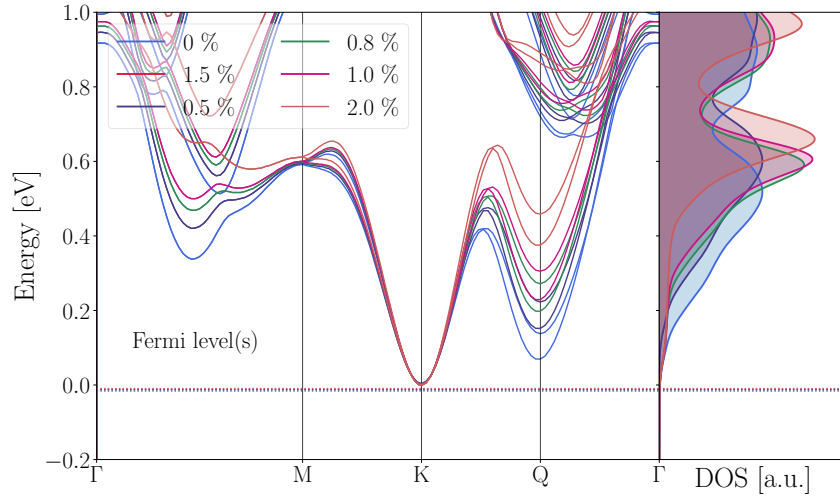


Figure 6.5: Electronic band structure and density of electronic states for the unstrained system (blue) and the 2% tensile strain (red). The zero of energy is set at the top of the valence band for each case: the Fermi level, accounting for doping and electronic temperature, is shown.

the highest strain. Since we have observed minimal variations to the phonons and electron-phonon interactions between the unstrained and strained setups at similar valley occupations, we can claim that the main strain-induced variations of mobility are thus due to the changes in valley occupations occurring due to the shift in the valley positions. We then use the model of Ref. [145] to obtain the mobility as a function of strain (via ΔE_{KQ}). We start from the difference in the valley position in the experimental structure and shift the Q valley according to the strain. The electron-phonon interactions are corrected and the Boltzmann transport equation is solved at each value of the shift to get the mobility as a function on the valley positions, following the model of Ref. [145], which is parametrized *ab initio*. Our results are summarized in Fig. 6.6 and show an increase up to a factor of 10 with respect to the unstained structure, which is in agreement with the experimental findings. In addition, the mobility increase is found to quickly saturate for relatively small strain, i.e., 0.8% as a consequence of the shift of the Q valley away from the thermal layer, i.e., energy window significant for scattering.

Nevertheless, in general, quantitative agreement between experiments and theory is often difficult to achieve. In fact, the measured and computed mobilities can differ by an order of magnitude, and this is probably linked to the presence of defects in real experiments, which we neglect here. Further improvements and insights could be achieved by measuring the experimental mobility at different temperatures to extrapolate the overall dependence on defect scattering and adding it as post-processing on top of our *ab initio* results. Thus far, this indicates the resistance to defect formation as a crucial parameter to incorporate in future screening, being one of the most important sources of discrepancies between computational and experimental studies in the literature.

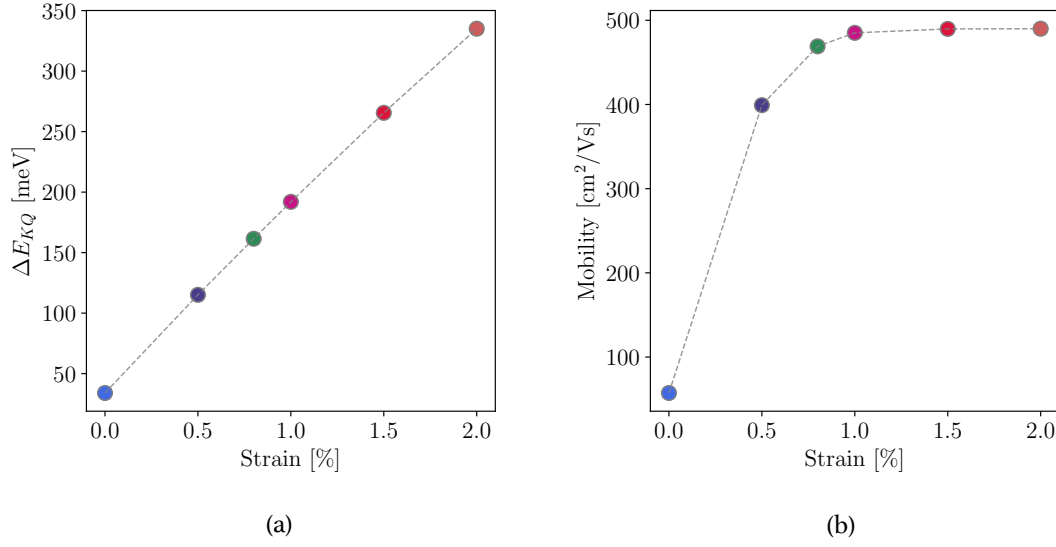


Figure 6.6: Variation of (a) valley energy separation, ΔE_{KQ} , and (b) room-temperature electron mobility as a function of the applied strain.

6.3 Summary

In this chapter, our focus shifted from materials discovery to engineering, and we focused on an experimental collaboration aimed at tuning the mobility of MoS₂ channels for FETs using permanent strain. The experimental approach involves depositing the channel on a corrugated substrate. On the theoretical side, we investigated the effect of strain on the electronic band structure, phonon dispersion, EPC, and electron mobilities. Our aim was to support and complement the experimental evidence. However, our results have highlighted that the main mechanism in tuning FET performance is the energetics of the K and Q valleys as a function of strain. This knowledge is essential for further comparison with experimental results and accessing the expected increase in the mobility ratio.

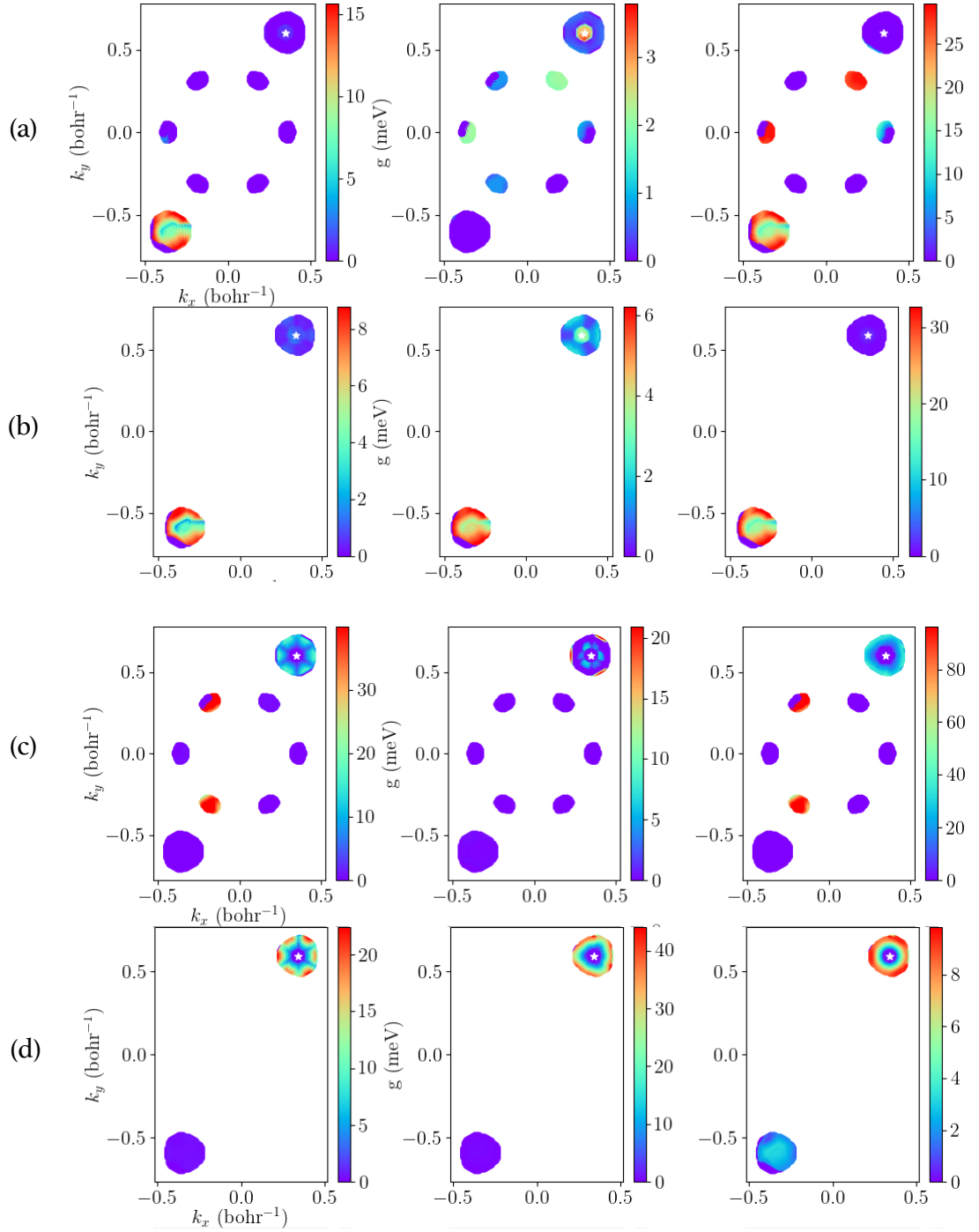


Figure 6.7: Interpolated EPC for three acoustic modes (i.e., LA, TA, ZA) in MoS₂. The first and third panels (a, c) refer to the unstrained material and differ in the initial electronic state (white star), with one being in the lowest K (a) or K' valley (c). The second and fourth panels (b, d) show the corresponding cases for the 2% strained system, with the Q valleys absent and lying outside the thermal layer. The color plot shows the strength of the coupling to all possible final states for each phonon mode (energetically ordered from left to right).

7 Conclusions

This thesis represents an effort to further the interest in both fundamental and technological research on nanostructures, namely 1D and 2D materials. Here, we attempted to emphasize the role of dimensionality in shaping materials properties – such as phonons, electron-phonon coupling, and transport – suggesting how these dimensionality signatures could be exploited for practical applications and potentially engineered. To this aim, we combined analytical and algorithmic developments along with automation strategies aiming to accelerate materials discovery.

First we discussed a novel implementation of DFT and DFPT tailored for 1D systems. The key ingredient in this case is the inclusion of the Coulomb cutoff, a reciprocal space technique designed to correct for the spurious interactions between periodic images in periodic-boundary conditions. We thus implemented a modified version of the cutoff, tailored for 1D materials, within our *ab-initio* code of reference, Quantum ESPRESSO. In short, the described implementation consists in modifying the Coulomb kernel on which all the relevant potentials are built. This eventually unlocks the possibility to compute energies, forces, stresses, phonons and electron-phonon properties for any kind of system with 1D periodicity, including chains, wires, tubes, and polymers. Our work thus aims to restore the proper open-boundary conditions, unveiling the true response of the this changes do no isolated 1D system.

Supported by the presented first-principles developments, we focused on the theoretical challenge of developing the missing theory for polar-optical, infrared-active phonons in 1D systems. We discussed in detail the derivation of the proposed analytical model, describing the interplay between the phonon-induced polarization and electronic screening. From such model, we eventually obtained a fully analytic expression for the long-wavelength dispersion relations of LO modes, as well as for the induced interaction potential felt by the electrons. Based on these results, we argued for a breakdown of the dielectric shift experienced by LO phonons in 1D and showed its logarithmic asymptotic behavior in terms of phonon momenta and material size, thus highlighting the peculiarity of this dimensionality signature. This

signature also affects the electron-phonon interactions, leading to a peaked long-wavelength behavior that promises to be relevant for many applications, including transport. This novel understanding is supported by the accurate first-principles description provided by the implemented open-boundary conditions, which are shown to be fundamental in restoring the true physical response of 1D systems. Notably, the dielectric properties and the radius of the 1D material are linked by the present model to the red shifts observed in infrared and Raman spectra, opening new characterization avenues. Overall, our effort revolving around 1D materials unlocked the possibility to accurately compute linear response in these systems, shed light on the transition between dimensionalities, and paved the way for similar developments in the field of charge transport, optical coupling and polaritronics.

In the last part of this thesis, we focused on 2D materials, namely gated semiconductors. In this case, the tools at our disposal already allowed for an accurate microscopic investigation of charge transport, which was the application we had in mind. Thus, we devoted ourselves to the hunt for high-mobility candidates, which involves materials discovery and engineering. We first focused on the computational quest for high-mobility candidates by exploring the Materials Cloud 2D database. In this respect, we discussed the workflow exploited, the main results in terms of promising materials, and the future perspectives. In the context of materials engineering, we presented an ongoing project that involves both theory and experiments. The idea is to tune the mobility of MoS₂ channels for FETs by permanent strain. This is achieved experimentally by depositing the channel on a corrugated substrate. On the theoretical side, we investigated the effect of strain on electronic band structure, phonon dispersion, EPC and electron mobility to support and complement the experimental evidences. Besides a qualitative explanation of the measured mobility enhancement upon strain, we discussed the difficulties and possible solutions to reach a quantitative agreement between simulations and experiments. In both projects, our methodological approach consisted in combining accurate first-principles calculations (i.e., DFT and DFPT, accounting for materials dimensionality and electrostatic doping) with state-of-the-art Boltzmann transport theory; all of this is handled by a workflow powered by the AiiDA materials informatics infrastructure.

A Computational details

A.1 One-dimensional materials: model and first-principles calculations

The analytical and first-principles developments of this work are applied to the following systems: BN atomic-chain, armchair BN nanotubes of increasing radius (i.e., (4,4), (5,5), (6,6)), and a small wurtzite GaAs nanowire passivated with H atoms to saturate the dangling bonds on the surface (24 atoms in total).

Here, we report fully in Fig. A.1 the phonon dispersion relations for BN-nanotubes (5,5) and (6,6), which are used for comparison to the (4,4) tube in the main text. Also, in Tab. A.1 we summarize the key parameter of the model (i.e., the radius) and the LO and TO frequencies at Γ to support the discussion on mechanical effects. Referring also to Fig. 4.5 from the main text, it is worth mentioning that the dispersion of the acoustic phonons in the proximity of Γ are slightly negative and exhibit a characteristic ‘wing’. These wings stem from violation of the invariance and equilibrium conditions on the lattice potential. In fact, DFPT derived interatomic force constants satisfy the proper conditions (depending on the dimensionality of the system) only approximately due to numerical convergence issues such as insufficient k -sampling or incomplete basis sets. The customary approach is then to enforce them, as a post-processing, via a specific set of relations called acoustic sum rules [39, 164, 165]. During the elaboration of this work, the suitable acoustic sum rules, restoring the correct quadratic dispersion for flexural phonons in 1D, has been implemented as described in Ref. [166].

First-principles calculations of structural properties and phonons are performed with the Quantum ESPRESSO package [167, 37, 49], by combining DFT and DFPT. We use the PBE exchange-correlation functionals for all materials, with the exception of bulk wurtzite GaAs for which we use norm-conserving pseudopotentials within the local density approximation from the Original QE PS Library [168]. For 1D-DFT/DFPT calculations, newly implemented 1D periodic-boundary conditions (i.e., the 1D cutoff and the 1D phonon Fourier-interpolation based on the analytical model) are applied to properly describe linear response to a phonon

Appendix A. Computational details

1D system	t (bohr)	ω_{LO} (cm^{-1})	ω_{TO} (cm^{-1})	$\Delta\omega_{\text{mech}}$ (cm^{-1})
BN-chain	1.70	1804	489	1315
BN-NNT (4,4)	10.15	1306	1275	31
BN-NNT (5,5)	11.49	1319	1299	20
BN-NNT (6,6)	12.84	1326	1312	14
GaAs-NW 24	10.41	244	240	4

Table A.1: *Ab-initio* zone-center values for ω_{LO} , ω_{TO} and the mechanical splitting $\Delta\omega_{\text{mech}}$, and the effective radius t . This is computed by averaging the electronic density profile in the out-of-wire directions and performing a gaussian fitting for the chain ($t=2\sigma$), while setting a meaningful threshold for the other systems.

perturbation [61]. The pseudopotentials (except for the ones used for bulk GaAs) are taken from the Standard Solid-State Pseudopotentials (SSSP) library (precision version 1.1) [169] and the wave-function and charge density energy cutoff have been selected accordingly: 110 and 440 Ry for the chain, 80 and 440 Ry for nanotubes, and 90 and 720 Ry for the GaAs nanowire. For bulk GaAs, we selected instead a wave-function cutoff of 80 Ry. We treated all the materials under study as non-magnetic insulators (i.e., fixed occupations) and a fine electron-momenta distance of approximately 0.2 \AA^{-1} (unshifted mesh) has been used to sample the Brillouin zone. The convergence of all the relevant parameters have been performed aiming to an accuracy on the final phonon frequencies of few cm^{-1} .

A.2 Two-dimensional materials: mobility calculations

First-principles calculation of structures, electronic properties, phonons and EPCs are performed within the Quantum ESPRESSO (QE) package [37] in the framework of 2D-DFT and DFPT [29] within the PBE or PBEsol approximations (depending on the material). Here by ‘2D-DFT/DFPT’ we mean that the 2D open-boundary conditions are applied: this is essential to capture the dimensionality signature of polar-optical phonons, screening and thus the long-wavelength electron-phonon dynamics in case of Fröhlich or piezoelectric coupling. To explicitly include doping in our calculations, and thus mimic the common experimental FET setup, we exploit the electrostatics of a symmetry double-gate field-effect setup. This is implemented in QE according to Ref.[29] and we use it to induce an electron or hole density of $n/p = 10^{13} \text{ cm}^{-2}$, corresponding to a high-doping regime in 2D systems. These calculations are handled and interfaced via the AiiDA material informatics infrastructure [130, 131] which also keeps trace of the provenance of calculations and data by storing all the information concerning our transport calculations in a database: this will be soon available in the Archive section of the Materials Cloud [170]. The standard protocol consists in using a $32 \times 32 \times 1$ Monkhorst-Pack k-point grids to sample the BZ, 0.02 Ry Marzari-Vanderbilt cold smearing and the SSSP Pseudopotentials (efficiency version 0.7) with the suggested cutoffs. PAW pseudopotentials are incompatible with the use of symmetry set in place to minimize the number of EPCs to be explicitly computed, for this reason, when present in the selected library, they are substituted with pseudopotentials selected from the pseudodojo [171] or PS libraries [168].

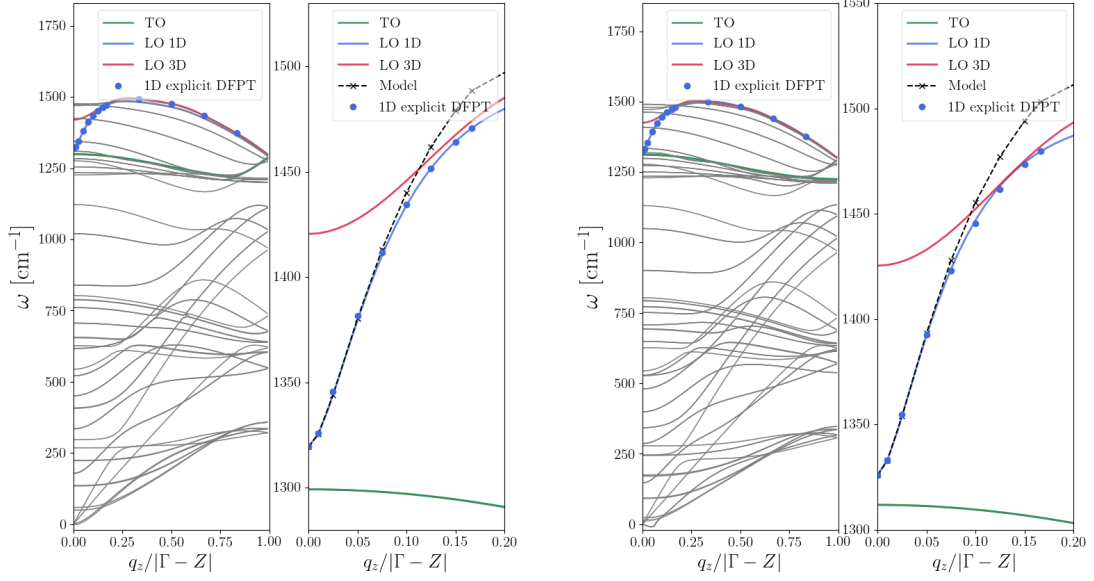


Figure A.1: Phonon dispersion relations of (5,5) and (6,6) BN nanotubes, respectively. On the left panels, we compare the *ab-initio* results using DFPT in 3D (no cutoff between period copies and 3D long-ranged electrostatic dipole-dipole long-range interactions) and using 1D-DFPT (1D Coulomb cutoff and 1D long-range interactions). On the right panels, the interpolated and explicit DFPT results are shown for long-wavelength polar-optical phonons and compared with the analytical model.

These details along as the related minor changes in the calculation parameters will be soon accessible on the Materials Cloud archive, as mentioned. Finally, the initial valley structure is computed non-self-consistently in the neutral material on very fine grids 90x90-120x120 for the preliminary screening analysis. The same grids are then used when doping is included to establish the proper sampling of the relevant valleys to compute EPIs. After symmetry reduction, the number of phonons necessary to compute the needed EPIs is approximately 50 for our single-valley materials. Spin-orbit coupling is not included and all materials are considered non-magnetic herein.

A.3 Theoretical methods and computational details for MoS₂

First-principles calculations are performed also in this case within the Quantum ESPRESSO (QE) package [37, 116] in the framework of 2D-DFT and DFPT [29], including a cutoff on the Coulomb interaction to implement the correct 2D boundary conditions and gates to simulate electrostatic doping as induced in common FET setups. The exchange-correlation functional is approximated using the Perdew-Burke-Ernzerhof (PBE) formulation of the generalized-

Appendix A. Computational details

gradient approximation [172]. We explicitly include in our simulations spin-orbit coupling by using fully-relativistic norm-conserving pseudopotentials [173] from the Pseudo-Dojo library [171]. To ensure fine sampling close to the Fermi level, we use a non-uniform grid [145] with the equivalent of a $96 \times 96 \times 1$ grid for electron momenta and Fermi-Dirac smearing corresponding to room temperature (0.002 Ry). A denser grid of $120 \times 120 \times 1$ is used for the non-self-consistent calculation of the valley structure. The mobility is simulated by considering electron scattering with phonons within a full energy- and momentum-dependent Boltzmann transport equation [48, 2]. We start from the position in the experimental structure and shift the Q valley according to the strain. The electron-phonon interactions are corrected and the Boltzmann transport equation is solved at each value of the shift to get the mobility as a function on the valley positions, following the model of Ref. [145], which is parametrized ab initio. The mobility is simulated by considering electron scattering with phonons within a full energy- and momentum-dependent Boltzmann transport equation [48, 2].

Bibliography

- [1] W. Kim, V. G. Dubrovskii, J. Vukajlovic-Plestina, G. Tütüncüoglu, L. Francaviglia, L. Güniat, H. Potts, M. Friedl, J.-B. Leran, and A. Fontcuberta i Morral, “Bistability of Contact Angle and Its Role in Achieving Quantum-Thin Self-Assisted GaAs nanowires,” *Nano Letters*, vol. 18, no. 1, pp. 49–57, 2018.
- [2] T. Sohler, M. Gibertini, and N. Marzari, “Profiling novel high-conductivity 2D semiconductors,” *2D Materials*, vol. 8, no. 1, p. 015025, 2020.
- [3] R. P. Feynman, “Plenty of room at the bottom,” in *APS annual meeting*, 1959.
- [4] M. S. Dresselhaus, G. Dresselhaus, and P. C. Eklund, *Science of fullerenes and carbon nanotubes: their properties and applications*. Elsevier, 1996.
- [5] M. S. Dresselhaus, G. Dresselhaus, R. Saito, and A. Jorio, “Raman spectroscopy of carbon nanotubes,” *Physics reports*, vol. 409, no. 2, pp. 47–99, 2005.
- [6] M. S. Dresselhaus, G. Chen, M. Y. Tang, R. Yang, H. Lee, D. Wang, Z. Ren, J.-P. Fleurial, and P. Gogna, “New directions for low-dimensional thermoelectric materials,” *Advanced materials*, vol. 19, no. 8, pp. 1043–1053, 2007.
- [7] L. D. Hicks and M. S. Dresselhaus, “Effect of quantum-well structures on the thermoelectric figure of merit,” *Physical Review B*, vol. 47, no. 19, p. 12727, 1993.
- [8] L. D. Hicks and M. S. Dresselhaus, “Thermoelectric figure of merit of a one-dimensional conductor,” *Physical review B*, vol. 47, no. 24, p. 16631, 1993.
- [9] A. K. Geim and K. S. Novoselov, “The rise of graphene,” *Nature materials*, vol. 6, no. 3, pp. 183–191, 2007.
- [10] H. W. Kroto, J. R. Heath, S. C. O’Brien, R. E. Curl, and R. E. Smalley, “C60: Buckminsterfullerene,” *Nature*, vol. 318, no. 6042, pp. 162–163, 1985.
- [11] N. Taniguchi, “On the basic concept of nanotechnology,” *Proceeding of the ICPE*, 1974.
- [12] K. E. Drexler, “Nanotechnology: from Feynman to funding,” *Bulletin of Science, Technology & Society*, vol. 24, no. 1, pp. 21–27, 2004.

- [13] F. Libbi, N. Bonini, and N. Marzari, "Thermomechanical properties of honeycomb lattices from internal-coordinates potentials: the case of graphene and hexagonal boron nitride," *2D Materials*, vol. 8, p. 015026, dec 2020.
- [14] D. G. Papageorgiou, I. A. Kinloch, and R. J. Young, "Mechanical properties of graphene and graphene-based nanocomposites," *Progress in materials science*, vol. 90, pp. 75–127, 2017.
- [15] K. I. Bolotin, K. Sikes, Z. Jiang, M. Klima, G. Fudenberg, J. Hone, P. Kim, and H. L. Stormer, "Ultrahigh electron mobility in suspended graphene," *Solid state communications*, vol. 146, no. 9-10, pp. 351–355, 2008.
- [16] Q. H. Wang, K. Kalantar-Zadeh, A. Kis, J. N. Coleman, and M. S. Strano, "Electronics and optoelectronics of two-dimensional transition metal dichalcogenides," *Nature nanotechnology*, vol. 7, no. 11, pp. 699–712, 2012.
- [17] N. Mounet, M. Gibertini, P. Schwaller, D. Campi, A. Merkys, A. Marrazzo, T. Sohier, I. E. Castelli, A. Cepellotti, G. Pizzi, *et al.*, "Two-dimensional materials from high-throughput computational exfoliation of experimentally known compounds," *Nature nanotechnology*, vol. 13, no. 3, pp. 246–252, 2018.
- [18] A. C. Ferrari, F. Bonaccorso, V. Fal'Ko, K. S. Novoselov, S. Roche, P. Bøggild, S. Borini, F. H. Koppens, V. Palermo, N. Pugno, *et al.*, "Science and technology roadmap for graphene, related two-dimensional crystals, and hybrid systems," *Nanoscale*, vol. 7, no. 11, pp. 4598–4810, 2015.
- [19] S. Manzeli, D. Ovchinnikov, D. Pasquier, O. V. Yazyev, and A. Kis, "2D transition metal dichalcogenides," *Nature Reviews Materials*, vol. 2, no. 8, pp. 1–15, 2017.
- [20] B. Radisavljevic, A. Radenovic, J. Brivio, V. Giacometti, and A. Kis, "Single-layer MoS₂ transistors," *Nature nanotechnology*, vol. 6, no. 3, pp. 147–150, 2011.
- [21] F. Schwierz, "Graphene transistors," *Nature nanotechnology*, vol. 5, no. 7, pp. 487–496, 2010.
- [22] C. Ahn, Z. Jiang, C.-S. Lee, H.-Y. Chen, J. Liang, L. S. Liyanage, and H.-S. P. Wong, "1D selection device using carbon nanotube FETs for high-density cross-point memory arrays," *IEEE Transactions on Electron Devices*, vol. 62, no. 7, pp. 2197–2204, 2015.
- [23] J. Knoch, S. Mantl, and J. Appenzeller, "Impact of the dimensionality on the performance of tunneling FETs: Bulk versus one-dimensional devices," *Solid-State Electronics*, vol. 51, no. 4, pp. 572–578, 2007.
- [24] Y. Xia, P. Yang, Y. Sun, Y. Wu, B. Mayers, B. Gates, Y. Yin, F. Kim, and H. Yan, "One-dimensional nanostructures: synthesis, characterization, and applications," *Advanced materials*, vol. 15, no. 5, pp. 353–389, 2003.

-
- [25] X. Gonze and C. Lee, "Dynamical matrices, Born effective charges, dielectric permittivity tensors, and interatomic force constants from density-functional perturbation theory," *Physical Review B*, vol. 55, no. 16, p. 10355, 1997.
- [26] S. Baroni, S. De Gironcoli, A. Dal Corso, and P. Giannozzi, "Phonons and related crystal properties from density-functional perturbation theory," *Reviews of modern Physics*, vol. 73, no. 2, p. 515, 2001.
- [27] P. Giannozzi, S. De Gironcoli, P. Pavone, and S. Baroni, "Ab initio calculation of phonon dispersions in semiconductors," *Physical Review B*, vol. 43, no. 9, p. 7231, 1991.
- [28] A. Dal Corso, S. Baroni, R. Resta, and S. de Gironcoli, "Ab initio calculation of phonon dispersions in II-VI semiconductors," *Physical Review B*, vol. 47, no. 7, p. 3588, 1993.
- [29] T. Sohier, M. Calandra, and F. Mauri, "Density-functional calculation of static screening in two-dimensional materials: The long-wavelength dielectric function of graphene," *Physical Review B*, vol. 91, no. 16, p. 165428, 2015.
- [30] N. W. Ashcroft, N. D. Mermin, *et al.*, "Solid state physics," 1976.
- [31] H. Böttger, *Principles of the theory of lattice dynamics*. Vch Pub, 1983.
- [32] G. Grosso and G. P. Parravicini, *Solid state physics*. Academic press, 2013.
- [33] F. Giustino, *Materials modelling using density functional theory: properties and predictions*. Oxford University Press, 2014.
- [34] J. M. Ziman, *Electrons and phonons: the theory of transport phenomena in solids*. Oxford university press, 2001.
- [35] P. Hohenberg and W. Kohn, "Inhomogeneous electron gas," *Physical review*, vol. 136, no. 3B, p. B864, 1964.
- [36] W. Kohn and L. J. Sham, "Self-consistent equations including exchange and correlation effects," *Physical review*, vol. 140, no. 4A, p. A1133, 1965.
- [37] P. Giannozzi, S. Baroni, N. Bonini, M. Calandra, R. Car, C. Cavazzoni, D. Ceresoli, G. L. Chiarotti, M. Cococcioni, I. Dabo, *et al.*, "Quantum espresso: a modular and open-source software project for quantum simulations of materials," *Journal of physics: Condensed matter*, vol. 21, no. 39, p. 395502, 2009.
- [38] G. Giuliani and G. Vignale, *Quantum theory of the electron liquid*. Cambridge university press, 2005.
- [39] M. Born, K. Huang, and M. Lax, "Dynamical theory of crystal lattices," *American Journal of Physics*, vol. 23, no. 7, pp. 474–474, 1955.
- [40] W. Cochran and R. Cowley, "Dielectric constants and lattice vibrations," *Journal of Physics and Chemistry of Solids*, vol. 23, no. 5, pp. 447–450, 1962.

Bibliography

- [41] T. Sohier, M. Gibertini, M. Calandra, F. Mauri, and N. Marzari, “Breakdown of optical phonons’ splitting in two-dimensional materials,” *Nano letters*, vol. 17, no. 6, pp. 3758–3763, 2017.
- [42] R. M. Pick, M. H. Cohen, and R. M. Martin, “Microscopic theory of force constants in the adiabatic approximation,” *Physical Review B*, vol. 1, no. 2, p. 910, 1970.
- [43] M. Tinkham, *Group theory and quantum mechanics*. Courier Corporation, 2003.
- [44] P. Vogl, “Microscopic theory of electron-phonon interaction in insulators or semiconductors,” *Physical Review B*, vol. 13, no. 2, p. 694, 1976.
- [45] T. Sohier, M. Calandra, and F. Mauri, “Two-dimensional fröhlich interaction in transition-metal dichalcogenide monolayers: Theoretical modeling and first-principles calculations,” *Physical Review B*, vol. 94, no. 8, p. 085415, 2016.
- [46] G. Chen, *Nanoscale energy transport and conversion: a parallel treatment of electrons, molecules, phonons, and photons*. Oxford university press, 2005.
- [47] S. Poncé, W. Li, S. Reichardt, and F. Giustino, “First-principles calculations of charge carrier mobility and conductivity in bulk semiconductors and two-dimensional materials,” *Reports on Progress in Physics*, vol. 83, no. 3, p. 036501, 2020.
- [48] T. Sohier, D. Campi, N. Marzari, and M. Gibertini, “Mobility of two-dimensional materials from first principles in an accurate and automated framework,” *Physical Review Materials*, vol. 2, no. 11, p. 114010, 2018.
- [49] P. Giannozzi, O. Andreussi, T. Brumme, O. Bunau, M. B. Nardelli, M. Calandra, R. Car, C. Cavazzoni, D. Ceresoli, M. Cococcioni, *et al.*, “Advanced capabilities for materials modelling with quantum espresso,” *Journal of physics: Condensed matter*, vol. 29, no. 46, p. 465901, 2017.
- [50] C. A. Rozzi, D. Varsano, A. Marini, E. K. Gross, and A. Rubio, “Exact Coulomb cutoff technique for supercell calculations,” *Physical Review B*, vol. 73, no. 20, p. 205119, 2006.
- [51] M. Royo and M. Stengel, “Exact long-range dielectric screening and interatomic force constants in quasi-two-dimensional crystals,” *Phys. Rev. X*, vol. 11, p. 041027, Nov 2021.
- [52] A. Castro, E. Räsänen, and C. A. Rozzi, “Exact Coulomb cutoff technique for supercell calculations in two dimensions,” *Physical Review B*, vol. 80, no. 3, p. 033102, 2009.
- [53] R. Resta, “Macroscopic polarization in crystalline dielectrics: the geometric phase approach,” *Reviews of modern physics*, vol. 66, no. 3, p. 899, 1994.
- [54] R. Resta and D. Vanderbilt, “Theory of polarization: a modern approach,” *Physics of ferroelectrics: a modern perspective*, pp. 31–68, 2007.

-
- [55] S. Ismail-Beigi, "Truncation of periodic image interactions for confined systems," *Physical Review B*, vol. 73, no. 23, p. 233103, 2006.
- [56] S. Piscanec, M. Lazzeri, F. Mauri, A. Ferrari, and J. Robertson, "Kohn anomalies and electron-phonon interactions in graphite," *Physical review letters*, vol. 93, no. 18, p. 185503, 2004.
- [57] N. Rivano, N. Marzari, and T. Sohler, "Infrared-active phonons in one-dimensional materials and their spectroscopic signatures," *arXiv.2208.09887, under review*, 2023.
- [58] X. Gonze, J.-C. Charlier, D. Allan, and M. Teter, "Interatomic force constants from first principles: The case of α -quartz," *Physical Review B*, vol. 50, no. 17, p. 13035, 1994.
- [59] G. Kern, G. Kresse, and J. Hafner, "Ab initio calculation of the lattice dynamics and phase diagram of boron nitride," *Physical Review B*, vol. 59, no. 13, p. 8551, 1999.
- [60] M. Royo and M. Stengel, "First-principles theory of spatial dispersion: Dynamical quadrupoles and flexoelectricity," *Phys. Rev. X*, vol. 9, p. 021050, Jun 2019.
- [61] N. Rivano, N. Marzari, and T. Sohler, "Density functional perturbation theory for one-dimensional systems: implementation and relevance for phonons and electron-phonon interaction," *to be submitted*, 2023.
- [62] E. Mele and P. Král, "Electric polarization of heteropolar nanotubes as a geometric phase," *Physical review letters*, vol. 88, no. 5, p. 056803, 2002.
- [63] D. Sánchez-Portal and E. Hernandez, "Vibrational properties of single-wall nanotubes and monolayers of hexagonal BN," *Physical Review B*, vol. 66, no. 23, p. 235415, 2002.
- [64] K. Michel and B. Verberck, "Theory of elastic and piezoelectric effects in two-dimensional hexagonal boron nitride," *Physical review B*, vol. 80, no. 22, p. 224301, 2009.
- [65] M. De Luca, X. Cartoixa, D. I. Indolese, J. Martín-Sánchez, K. Watanabe, T. Taniguchi, C. Schönenberger, R. Trotta, R. Rurali, and I. Zardo, "Experimental demonstration of the suppression of optical phonon splitting in 2D materials by Raman spectroscopy," *2D Materials*, vol. 7, no. 3, p. 035017, 2020.
- [66] J. Sjakste, N. Vast, M. Calandra, and F. Mauri, "Wannier interpolation of the electron-phonon matrix elements in polar semiconductors: Polar-optical coupling in gaas," *Phys. Rev. B*, vol. 92, p. 054307, Aug 2015.
- [67] C. Verdi and F. Giustino, "Fröhlich electron-phonon vertex from first principles," *Physical review letters*, vol. 115, no. 17, p. 176401, 2015.
- [68] N. Rivera, T. Christensen, and P. Narang, "Phonon polaritonics in two-dimensional materials," *Nano letters*, vol. 19, no. 4, pp. 2653–2660, 2019.

Bibliography

- [69] R. H. Lyddane, R. G. Sachs, and E. Teller, "On the polar vibrations of alkali halides," *Phys. Rev.*, vol. 59, pp. 673–676, Apr 1941.
- [70] I. Zardo, S. Conesa-Boj, F. Peiro, J. Morante, J. Arbiol, E. Uccelli, G. Abstreiter, and A. F. i Morral, "Raman spectroscopy of wurtzite and zinc-blende GaAsnanowires: polarization dependence, selection rules, and strain effects," *Physical review B*, vol. 80, no. 24, p. 245324, 2009.
- [71] S. Zhang, Y. Liu, M. Xia, L. Zhang, E. Zhang, R. Liang, and S. Zhao, "Long-wavelength optical phonons in single-walled boron nitride nanotubes," *Physica B: Condensed Matter*, vol. 403, no. 23-24, pp. 4196–4201, 2008.
- [72] S. Piscanec, M. Lazzeri, J. Robertson, A. C. Ferrari, and F. Mauri, "Optical phonons in carbon nanotubes: Kohn anomalies, Peierls distortions, and dynamic effects," *Physical Review B*, vol. 75, no. 3, p. 035427, 2007.
- [73] K. W. Adu, Q. Xiong, H. Gutierrez, G. Chen, and P. Eklund, "Raman scattering as a probe of phonon confinement and surface optical modes in semiconducting nanowires," *Applied Physics A*, vol. 85, no. 3, pp. 287–297, 2006.
- [74] R. Nemanich, S. Solin, and R. M. Martin, "Light scattering study of boron nitride microcrystals," *Physical Review B*, vol. 23, no. 12, p. 6348, 1981.
- [75] G. Mahan, R. Gupta, Q. Xiong, C. Adu, and P. Eklund, "Optical phonons in polar semiconductor nanowires," *Physical Review B*, vol. 68, no. 7, p. 073402, 2003.
- [76] G. D. Mahan, "Nanoscale dielectric constants: Dipole summations and the dielectric function in nanowires and quantum dots of cubic materials," *Phys. Rev. B*, vol. 74, p. 033407, Jul 2006.
- [77] I. Campbell and P. M. Fauchet, "The effects of microcrystal size and shape on the one phonon Raman spectra of crystalline semiconductors," *Solid State Communications*, vol. 58, no. 10, pp. 739–741, 1986.
- [78] H. Richter, Z. Wang, and L. Ley, "The one phonon Raman spectrum in microcrystalline silicon," *Solid State Communications*, vol. 39, no. 5, pp. 625–629, 1981.
- [79] Q. Xiong, G. Chen, H. Gutierrez, and P. Eklund, "Raman scattering studies of individual polar semiconducting nanowires: phonon splitting and antenna effects," *Applied Physics A*, vol. 85, no. 3, pp. 299–305, 2006.
- [80] P. M. Fauchet and I. H. Campbell, "Raman spectroscopy of low-dimensional semiconductors," *Critical Reviews in Solid State and Material Sciences*, vol. 14, no. S1, pp. s79–s101, 1988.
- [81] L. Wirtz, A. Rubio, R. A. de la Concha, and A. Loiseau, "Ab initio calculations of the lattice dynamics of boron nitride nanotubes," *Phys. Rev. B*, vol. 68, p. 045425, Jul 2003.

-
- [82] V. N. Popov, "Lattice dynamics of single-walled boron nitride nanotubes," *Physical Review B*, vol. 67, no. 8, p. 085408, 2003.
- [83] J. Tóbkik and A. Dal Corso, "Electric fields with ultrasoft pseudo-potentials: Applications to benzene and anthracene," *The Journal of Chemical Physics*, vol. 120, no. 21, pp. 9934–9941, 2004.
- [84] E. K. Yu, D. A. Stewart, and S. Tiwari, "Ab initio study of polarizability and induced charge densities in multilayer graphene films," *Phys. Rev. B*, vol. 77, p. 195406, May 2008.
- [85] B. Kozinsky and N. Marzari, "Static dielectric properties of carbon nanotubes from first principles," *Phys. Rev. Lett.*, vol. 96, p. 166801, Apr 2006.
- [86] T. Tian, D. Scullion, D. Hughes, L. H. Li, C.-J. Shih, J. Coleman, M. Chhowalla, and E. J. Santos, "Electronic polarizability as the fundamental variable in the dielectric properties of two-dimensional materials," *Nano letters*, vol. 20, no. 2, pp. 841–851, 2019.
- [87] K. Andersen, S. Latini, and K. S. Thygesen, "Dielectric genome of van der Waals heterostructures," *Nano letters*, vol. 15, no. 7, pp. 4616–4621, 2015.
- [88] M. J. Mohn, R. Hambach, P. Wachsmuth, C. Giorgetti, and U. Kaiser, "Dielectric properties of graphene/mos 2 heterostructures from ab initio calculations and electron energy-loss experiments," *Physical Review B*, vol. 97, no. 23, p. 235410, 2018.
- [89] T. Sohler, M. Gibertini, and M. J. Verstraete, "Remote free-carrier screening to boost the mobility of fröhlich-limited two-dimensional semiconductors," *Physical Review Materials*, vol. 5, no. 2, p. 024004, 2021.
- [90] L. Sponza and F. Ducastelle, "Proper ab-initio dielectric function of 2D materials and their polarizable thickness," *arXiv preprint arXiv:2011.07811*, 2020.
- [91] C. Freysoldt, P. Eggert, P. Rinke, A. Schindlmayr, and M. Scheffler, "Screening in two dimensions: G w calculations for surfaces and thin films using the repeated-slab approach," *Physical Review B*, vol. 77, no. 23, p. 235428, 2008.
- [92] E. Rokuta, Y. Hasegawa, K. Suzuki, Y. Gamou, C. Oshima, and A. Nagashima, "Phonon dispersion of an epitaxial monolayer film of hexagonal boron nitride on Ni (111)," *Physical review letters*, vol. 79, no. 23, p. 4609, 1997.
- [93] R. Geick, C. Perry, and G. Rupprecht, "Normal modes in hexagonal boron nitride," *Physical Review*, vol. 146, no. 2, p. 543, 1966.
- [94] D. Strauch and B. Dorner, "Phonon dispersion in gaas," *Journal of Physics: Condensed Matter*, vol. 2, no. 6, p. 1457, 1990.
- [95] J. Waugh and G. Dolling, "Crystal dynamics of gallium arsenide," *Physical Review*, vol. 132, no. 6, p. 2410, 1963.

Bibliography

- [96] K. S. Novoselov, A. K. Geim, S. V. Morozov, D.-e. Jiang, Y. Zhang, S. V. Dubonos, I. V. Grigorieva, and A. A. Firsov, "Electric field effect in atomically thin carbon films," *Science*, vol. 306, no. 5696, pp. 666–669, 2004.
- [97] Y. Zhang, Y.-W. Tan, H. L. Stormer, and P. Kim, "Experimental observation of the quantum hall effect and berry's phase in graphene," *Nature*, vol. 438, no. 7065, pp. 201–204, 2005.
- [98] K. S. Novoselov, A. K. Geim, S. V. Morozov, D. Jiang, M. I. Katsnelson, I. V. Grigorieva, S. Dubonos, and a. Firsov, "Two-dimensional gas of massless dirac fermions in graphene," *Nature*, vol. 438, no. 7065, pp. 197–200, 2005.
- [99] D. K. Efetov and P. Kim, "Controlling electron-phonon interactions in graphene at ultrahigh carrier densities," *Physical review letters*, vol. 105, no. 25, p. 256805, 2010.
- [100] S. Lebègue, T. Björkman, M. Klintenberg, R. M. Nieminen, and O. Eriksson, "Two-dimensional materials from data filtering and ab initio calculations," *Physical Review X*, vol. 3, no. 3, p. 031002, 2013.
- [101] D. Hanlon, C. Backes, E. Doherty, C. S. Cucinotta, N. C. Berner, C. Boland, K. Lee, A. Harvey, P. Lynch, Z. Gholamvand, *et al.*, "Liquid exfoliation of solvent-stabilized few-layer black phosphorus for applications beyond electronics," *Nature communications*, vol. 6, no. 1, pp. 1–11, 2015.
- [102] P. Yasaei, B. Kumar, T. Foroozan, C. Wang, M. Asadi, D. Tuschel, J. E. Indacochea, R. F. Klie, and A. Salehi-Khojin, "High-quality black phosphorus atomic layers by liquid-phase exfoliation," *Advanced Materials*, vol. 27, no. 11, pp. 1887–1892, 2015.
- [103] G. Cheon, K.-A. N. Duerloo, A. D. Sendek, C. Porter, Y. Chen, and E. J. Reed, "Data mining for new two-and one-dimensional weakly bonded solids and lattice-commensurate heterostructures," *Nano letters*, vol. 17, no. 3, pp. 1915–1923, 2017.
- [104] C. Gibaja, D. Rodriguez-San-Miguel, P. Ares, J. Gómez-Herrero, M. Varela, R. Gillen, J. Maultzsch, F. Hauke, A. Hirsch, G. Abellán, *et al.*, "Few-layer antimonene by liquid-phase exfoliation," *Angewandte Chemie*, vol. 128, no. 46, pp. 14557–14561, 2016.
- [105] D. A. Bandurin, A. V. Tyurnina, G. L. Yu, A. Mishchenko, V. Zólyomi, S. V. Morozov, R. K. Kumar, R. V. Gorbachev, Z. R. Kudrynskyi, S. Pezzini, *et al.*, "High electron mobility, quantum hall effect and anomalous optical response in atomically thin InSe," *Nature nanotechnology*, vol. 12, no. 3, pp. 223–227, 2017.
- [106] G. E. Moore, "Cramming more components onto integrated circuits," *Proceedings of the IEEE*, vol. 86, no. 1, pp. 82–85, 1998.
- [107] B. Radisavljevic, M. B. Whitwick, and A. Kis, "Integrated circuits and logic operations based on single-layer MoS₂," *ACS nano*, vol. 5, no. 12, pp. 9934–9938, 2011.
- [108] S. Bertolazzi, J. Brivio, and A. Kis, "Stretching and breaking of ultrathin MoS₂," *ACS nano*, vol. 5, no. 12, pp. 9703–9709, 2011.

-
- [109] O. V. Yazyev and A. Kis, "MoS₂ and semiconductors in the flatland," *Materials Today*, vol. 18, no. 1, pp. 20–30, 2015.
- [110] D. Lembke and A. Kis, "Breakdown of high-performance monolayer MoS₂ transistors," *ACS nano*, vol. 6, no. 11, pp. 10070–10075, 2012.
- [111] D. Lembke, S. Bertolazzi, and A. Kis, "Single-layer MoS₂ electronics," *Accounts of chemical research*, vol. 48, no. 1, pp. 100–110, 2015.
- [112] C. R. Dean, A. F. Young, I. Meric, C. Lee, L. Wang, S. Sorgenfrei, K. Watanabe, T. Taniguchi, P. Kim, K. L. Shepard, *et al.*, "Boron nitride substrates for high-quality graphene electronics," *Nature nanotechnology*, vol. 5, no. 10, pp. 722–726, 2010.
- [113] F. Xia, D. B. Farmer, Y.-m. Lin, and P. Avouris, "Graphene field-effect transistors with high on/off current ratio and large transport band gap at room temperature," *Nano letters*, vol. 10, no. 2, pp. 715–718, 2010.
- [114] P. Allen, "New method for solving Boltzmann's equation for electrons in metals," *Physical Review B*, vol. 17, no. 10, p. 3725, 1978.
- [115] G. Grimvall *et al.*, "The electron-phonon interaction in metals," 1981.
- [116] F. Giustino, "Electron-phonon interactions from first principles," *Reviews of Modern Physics*, vol. 89, no. 1, p. 015003, 2017.
- [117] T. Gunst, T. Markussen, K. Stokbro, and M. Brandbyge, "First-principles method for electron-phonon coupling and electron mobility: Applications to two-dimensional materials," *Physical Review B*, vol. 93, no. 3, p. 035414, 2016.
- [118] M. M. Dacorogna, M. L. Cohen, and P. K. Lam, "Self-consistent calculation of the q dependence of the electron-phonon coupling in aluminum," *Physical review letters*, vol. 55, no. 8, p. 837, 1985.
- [119] J. M. Ziman, *Principles of the Theory of Solids*. Cambridge university press, 1972.
- [120] W. Li, "Electrical transport limited by electron-phonon coupling from Boltzmann transport equation: An ab initio study of si, al, and mos 2," *Physical Review B*, vol. 92, no. 7, p. 075405, 2015.
- [121] G. Samsonidze and B. Kozinsky, "Accelerated screening of thermoelectric materials by first-principles computations of electron–phonon scattering," *Advanced Energy Materials*, vol. 8, no. 20, p. 1800246, 2018.
- [122] M. Omini and A. Sparavigna, "Beyond the isotropic-model approximation in the theory of thermal conductivity," *Physical Review B*, vol. 53, no. 14, p. 9064, 1996.
- [123] M. Omini and A. Sparavigna, "Heat transport in dielectric solids with diamond structure," *NUOVO CIMENTO-SOCIETA ITALIANA DI FISICA SEZIONE D*, vol. 19, pp. 1537–1564, 1997.

Bibliography

- [124] D. Broido, A. Ward, and N. Mingo, “Lattice thermal conductivity of silicon from empirical interatomic potentials,” *Physical Review B*, vol. 72, no. 1, p. 014308, 2005.
- [125] G. Fugallo, M. Lazzeri, L. Paulatto, and F. Mauri, “Ab initio variational approach for evaluating lattice thermal conductivity,” *Physical Review B*, vol. 88, no. 4, p. 045430, 2013.
- [126] M. Fiorentini and N. Bonini, “Thermoelectric coefficients of n-doped silicon from first principles via the solution of the Boltzmann transport equation,” *Physical Review B*, vol. 94, no. 8, p. 085204, 2016.
- [127] L. Chaput, “Direct solution to the linearized phonon Boltzmann equation,” *Physical review letters*, vol. 110, no. 26, p. 265506, 2013.
- [128] A. Cepellotti and N. Marzari, “Thermal transport in crystals as a kinetic theory of relaxations,” *Physical Review X*, vol. 6, no. 4, p. 041013, 2016.
- [129] D. Campi, N. Mounet, M. Gibertini, G. Pizzi, and N. Marzari, “Novel materials in the Materials Cloud 2D database,” *arXiv preprint arXiv:2210.11301*, 2022.
- [130] G. Pizzi, A. Cepellotti, R. Sabatini, N. Marzari, and B. Kozinsky, “AiiDA: automated interactive infrastructure and database for computational science,” *Computational Materials Science*, vol. 111, pp. 218–230, 2016.
- [131] S. P. Huber, S. Zoupanos, M. Uhrin, L. Talirz, L. Kahle, R. Häuselmann, D. Gresch, T. Müller, A. V. Yakutovich, C. W. Andersen, *et al.*, “AiiDA 1.0, a scalable computational infrastructure for automated reproducible workflows and data provenance,” *Scientific data*, vol. 7, no. 1, pp. 1–18, 2020.
- [132] M. Uhrin, S. P. Huber, J. Yu, N. Marzari, and G. Pizzi, “Workflows in AiiDA: Engineering a high-throughput, event-based engine for robust and modular computational workflows,” *Computational Materials Science*, vol. 187, p. 110086, 2021.
- [133] “Inorganic Crystal Structure Database – ICSD | FIZ Karlsruhe.”
- [134] S. Gražulis, A. Daškevič, A. Merkys, D. Chateigner, L. Lutterotti, M. Quiros, N. R. Serebryanaya, P. Moeck, R. T. Downs, and A. Le Bail, “Crystallography open database (cod): an open-access collection of crystal structures and platform for world-wide collaboration,” *Nucleic acids research*, vol. 40, no. D1, pp. D420–D427, 2012.
- [135] P. Villars, N. Onodera, and S. Iwata, “The Linus Pauling file (LPF) and its application to materials design,” *Journal of Alloys and Compounds*, vol. 279, no. 1, pp. 1–7, 1998.
- [136] R. Claes, G. Brunin, M. Giantomassi, G.-M. Rignanese, and G. Hautier, “Assessing the quality of relaxation-time approximations with fully automated computations of phonon-limited mobilities,” *Physical Review B*, vol. 106, no. 9, p. 094302, 2022.

- [137] C. Zhang, R. Wang, H. Mishra, and Y. Liu, "Two-dimensional semiconductors with high intrinsic carrier mobility at room temperature," *Physical Review Letters*, vol. 130, no. 8, p. 087001, 2023.
- [138] J. Feng, M. Graf, K. Liu, D. Ovchinnikov, D. Dumcenco, M. Heiranian, V. Nandigana, N. R. Aluru, A. Kis, and A. Radenovic, "Single-layer MoS₂ nanopores as nanopower generators," *Nature*, vol. 536, no. 7615, pp. 197–200, 2016.
- [139] J. T. Robinson, J. S. Burgess, C. E. Junkermeier, S. C. Badescu, T. L. Reinecke, F. K. Perkins, M. K. Zalalutdniov, J. W. Baldwin, J. C. Culbertson, P. E. Sheehan, *et al.*, "Properties of fluorinated graphene films," *Nano letters*, vol. 10, no. 8, pp. 3001–3005, 2010.
- [140] H. Şahin, M. Topsakal, and S. Ciraci, "Structures of fluorinated graphene and their signatures," *Physical Review B*, vol. 83, no. 11, p. 115432, 2011.
- [141] H. Liu, Z. Hou, C. Hu, Y. Yang, and Z. Zhu, "Electronic and magnetic properties of fluorinated graphene with different coverage of fluorine," *The Journal of Physical Chemistry C*, vol. 116, no. 34, pp. 18193–18201, 2012.
- [142] F. Withers, M. Dubois, and A. K. Savchenko, "Electron properties of fluorinated single-layer graphene transistors," *Physical review B*, vol. 82, no. 7, p. 073403, 2010.
- [143] T. Deng, G. Wu, W. Shi, Z. M. Wong, J.-S. Wang, and S.-W. Yang, "Ab initio dipolar electron-phonon interactions in two-dimensional materials," *Phys. Rev. B*, vol. 103, p. 075410, Feb 2021.
- [144] M. M. Khatami, G. Gaddemane, M. L. Van de Put, M. K. Moravvej-Farshi, and W. G. Vandenberghe, "Electronic transport properties of hydrogenated and fluorinated graphene: a computational study," *Journal of Physics: Condensed Matter*, vol. 32, no. 49, p. 495502, 2020.
- [145] T. Sohler, P. M. de Melo, M. J. Verstraete, and Z. Zanolli, "The impact of valley profile on the mobility and Kerr rotation of transition metal dichalcogenides," *2D Materials*, 2022.
- [146] D. Plašienka and R. Martoňák, "Transformation pathways in high-pressure solid nitrogen: From molecular N₂ to polymeric cg-N," *The Journal of Chemical Physics*, vol. 142, no. 9, p. 094505, 2015.
- [147] C. Ji, A. A. Adeleke, L. Yang, B. Wan, H. Gou, Y. Yao, B. Li, Y. Meng, J. S. Smith, V. B. Prakapenka, *et al.*, "Nitrogen in black phosphorus structure," *Science advances*, vol. 6, no. 23, p. eaba9206, 2020.
- [148] N. Rivano, T. Sohler, G. Pizzi, and N. Marzari, "High-mobility single-valley candidates from the Materials Cloud 2D database," *in preparation*, 2023.
- [149] O. Lopez-Sanchez, D. Lembke, M. Kayci, A. Radenovic, and A. Kis, "Ultrasensitive photodetectors based on monolayer MoS₂," *Nature nanotechnology*, vol. 8, no. 7, pp. 497–501, 2013.

Bibliography

- [150] S. Manzeli, A. Allain, A. Ghadimi, and A. Kis, “Piezoresistivity and strain-induced band gap tuning in atomically thin MoS₂,” *Nano letters*, vol. 15, no. 8, pp. 5330–5335, 2015.
- [151] A. Splendiani, L. Sun, Y. Zhang, T. Li, J. Kim, C.-Y. Chim, G. Galli, and F. Wang, “Emerging photoluminescence in monolayer MoS₂,” *Nano letters*, vol. 10, no. 4, pp. 1271–1275, 2010.
- [152] B. W. Baugher, H. O. Churchill, Y. Yang, and P. Jarillo-Herrero, “Intrinsic electronic transport properties of high-quality monolayer and bilayer MoS₂,” *Nano letters*, vol. 13, no. 9, pp. 4212–4216, 2013.
- [153] S. Kim, A. Konar, W.-S. Hwang, J. H. Lee, J. Lee, J. Yang, C. Jung, H. Kim, J.-B. Yoo, J.-Y. Choi, *et al.*, “High-mobility and low-power thin-film transistors based on multilayer MoS₂ crystals,” *Nature communications*, vol. 3, no. 1, p. 1011, 2012.
- [154] W. Bao, X. Cai, D. Kim, K. Sridhara, and M. S. Fuhrer, “High mobility ambipolar MoS₂ field-effect transistors: Substrate and dielectric effects,” *Applied Physics Letters*, vol. 102, no. 4, p. 042104, 2013.
- [155] M. S. Fuhrer and J. Hone, “Measurement of mobility in dual-gated MoS₂ transistors,” *Nature nanotechnology*, vol. 8, no. 3, pp. 146–147, 2013.
- [156] K. Kaasbjerg, K. S. Thygesen, and A.-P. Jauho, “Acoustic phonon limited mobility in two-dimensional semiconductors: Deformation potential and piezoelectric scattering in monolayer MoS₂ from first principles,” *Physical Review B*, vol. 87, no. 23, p. 235312, 2013.
- [157] K. Kaasbjerg, K. S. Thygesen, and K. W. Jacobsen, “Phonon-limited mobility in n-type single-layer MoS₂ from first principles,” *Physical Review B*, vol. 85, no. 11, p. 115317, 2012.
- [158] X. Liu, A. K. Sachan, S. T. Howell, A. Conde-Rubio, A. W. Knoll, G. Boero, R. Zenobi, and J. Brugger, “Thermomechanical nanostraining of two-dimensional materials,” *Nano letters*, vol. 20, no. 11, pp. 8250–8257, 2020.
- [159] A. Conde-Rubio, X. Liu, G. Boero, and J. Brugger, “Edge-contact MoS₂ transistors fabricated using thermal scanning probe lithography,” *ACS applied materials & interfaces*, vol. 14, no. 37, pp. 42328–42336, 2022.
- [160] X. Xu, W. Yao, D. Xiao, and T. F. Heinz, “Spin and pseudospins in layered transition metal dichalcogenides,” *Nature Physics*, vol. 10, no. 5, pp. 343–350, 2014.
- [161] D. Xiao, G.-B. Liu, W. Feng, X. Xu, and W. Yao, “Coupled spin and valley physics in monolayers of MoS₂ and other group-VI dichalcogenides,” *Physical review letters*, vol. 108, no. 19, p. 196802, 2012.

-
- [162] T. Sohler, E. Ponomarev, M. Gibertini, H. Berger, N. Marzari, N. Ubrig, and A. F. Morpurgo, “Enhanced electron-phonon interaction in multivalley materials,” *Physical Review X*, vol. 9, no. 3, p. 031019, 2019.
- [163] M. Bollinger, K. W. Jacobsen, and J. K. Nørskov, “Atomic and electronic structure of MoS₂ nanoparticles,” *Physical Review B*, vol. 67, no. 8, p. 085410, 2003.
- [164] G. H. Begbie and M. Born, “Thermal scattering of X-rays by crystals-I. Dynamical foundation,” *Proceedings of the Royal Society of London. Series A. Mathematical and Physical Sciences*, vol. 188, no. 1013, pp. 179–188, 1947.
- [165] R. M. Pick, M. H. Cohen, and R. M. Martin, “Microscopic theory of force constants in the adiabatic approximation,” *Phys. Rev. B*, vol. 1, pp. 910–920, Jan 1970.
- [166] C. Lin, S. Poncé, and N. Marzari, “General invariance and equilibrium conditions for lattice dynamics in 1D, 2D, and 3D materials,” *npj Computational Materials*, vol. 8, no. 1, p. 236, 2022.
- [167] S. Baroni, S. de Gironcoli, A. Dal Corso, and P. Giannozzi, “Phonons and related crystal properties from density-functional perturbation theory,” *Rev. Mod. Phys.*, vol. 73, pp. 515–562, Jul 2001.
- [168] A. Dal Corso, “Pseudopotentials periodic table: From H to Pu,” *Computational Materials Science*, vol. 95, pp. 337–350, 2014.
- [169] G. Prandini, A. Marrazzo, I. E. Castelli, N. Mounet, and N. Marzari, “Precision and efficiency in solid-state pseudopotential calculations,” *npj Computational Materials*, vol. 4, no. 1, pp. 1–13, 2018.
- [170] L. Talirz, S. Kumbhar, E. Passaro, A. V. Yakutovich, V. Granata, F. Gargiulo, M. Borelli, M. Uhrin, S. P. Huber, S. Zoupanos, *et al.*, “Materials Cloud, a platform for open computational science,” *Scientific data*, vol. 7, no. 1, pp. 1–12, 2020.
- [171] M. J. van Setten, M. Giantomassi, E. Bousquet, M. J. Verstraete, D. R. Hamann, X. Gonze, and G.-M. Rignanese, “The PseudoDojo: Training and grading a 85 element optimized norm-conserving pseudopotential table,” *Computer Physics Communications*, vol. 226, pp. 39–54, 2018.
- [172] J. P. Perdew, K. Burke, and M. Ernzerhof, “Generalized gradient approximation made simple,” *Physical review letters*, vol. 77, no. 18, p. 3865, 1996.
- [173] D. Hamann, “Optimized norm-conserving Vanderbilt pseudopotentials,” *Physical Review B*, vol. 88, no. 8, p. 085117, 2013.

Curriculum Vitae

Personal data

Name	Norma Rivano
Date and place of birth	24.04.1994, Cagliari (Italy)
Citizenship	Italian
Email	norma.rivano@epfl.ch

Education

- 2018–2023 **PhD in Materials Science and Engineering**
École polytechnique fédérale de Lausanne (EPFL), Switzerland
PhD thesis: *Phonons, electron-phonon coupling and charge transport in low-dimensional materials*
Supervisors: Prof. Nicola Marzari, Dr. Giovanni Pizzi
- 2015–2018 **MSc in Physics, Structure of Matter**
University of Cagliari, Italy, **110/110 cum laude**
MSc thesis: *Structural, vibrational and thermal properties of one-dimensional carbon allotrope: an ab-initio study*
Supervisors: Prof. Luciano Colombo, Prof. Nicola Marzari
- 2017 Mar–Oct **MARVEL INSPIRE Potentials Fellowship**
École polytechnique fédérale de Lausanne (EPFL), Switzerland
MSc thesis and project (8 months)
- 2012–2015 **BSc in Physics**
University of Cagliari, Italy, **110/110 cum laude**
BSc thesis: *Thermal conductivity in crystalline solids: a microscopic theory based on phonon mean free path*
Supervisors: Prof. Claudio Melis, Prof. Luciano Colombo

Teaching

- 2020–2021 **Teaching assistant - Laboratory of Optical Metallography**
École polytechnique fédérale de Lausanne
Spring semester
Dr. Adeline Mélanie Agnès
- 2020–2021 **Teaching assistant - Laboratory of Optical Metallography**
École polytechnique fédérale de Lausanne
Fall semester
Dr. Adeline Mélanie Agnès
- 2019–2020 **Teaching assistant - Atomistic and Quantum Simulations of Materials**
École polytechnique fédérale de Lausanne
Spring semester
Prof. Nicola Marzari
- 2018–2019 **Teaching assistant - Quantum Physics**
École polytechnique fédérale de Lausanne
Spring semester
Prof. Alfredo Pasquarello

Research interests

Theoretical Condensed Matter Physics: semiconductors, electronic structure, vibrational properties, polar-optical phonons, electron-phonon interactions, charge transport, low-dimensional materials, high-throughput computing, first-principles methods, density-functional and density-functional perturbation theory.

Honors, awards and scholarship

- **INSPIRE Potentials MARVEL Master's Fellowship** – Fellowships to women students to conduct their Master's research thesis in a group participating in MARVEL (typically 4 places for each round of applications).
- **EDMX Research Day 2022** – Selected by a jury of postdocs as one of five the most impressive nominees within the PhD students of the EDMX department for an oral presentation.

Languages

English	Full professional proficiency
French	Elementary proficiency
Italian	Native language

Technical Skills

1. Development of numerical algorithms and theoretical first-principles methods
2. Software engineering: design, implementation and debugging of codes
3. Programming languages: Python, Fortran, Unix/Shell scripting
4. Version-control: Git (GitHub, GitLab)
5. Editing and typesetting tools: VSCode, Vim, LaTeX
6. Codes and softwares: Quantum ESPRESSO, Phonopy, Wannier90, AiiDa, XCrySDen
7. Other tools: Microsoft Office (Excel, Word, Powerpoint)

Publications

1. *Infrared-active phonons in one-dimensional materials and their spectroscopic signatures*, Norma Rivano, Nicola Marzari and Thibault Sohier (2022) –arXiv.2208.09887, under review in npj.
2. *Density functional perturbation theory for one-dimensional systems: implementation and relevance for phonons and electron-phonon interaction*, Norma Rivano, Nicola Marzari and Thibault Sohier (2023) – to submitted.
3. *Strained Monolayer MoS₂ Field Effect Transistors*, Xia Liu, Berke Erbas, Ana Conde-Rubio, Norma Rivano, Zhenyu Wang, Jin Jiang, Thibault Sohier, Marcos Penedo, Giovanni Boero, Mitali Banerjee, Georg Fantner, Nicola Marzari, Andras Kis, Juergen Brugger (2023) – to be submitted.
4. *High-mobility single-valley candidates from the Materials Cloud 2D database*, Norma Rivano, Thibault Sohier, Giovanni Pizzi and Nicola Marzari (2023) – in preparation.
5. AiiDA plugin package *aiida-wannier90*, Dominik Gresch, Antimo Marrazzo, Daniel Marchand, Giovanni Pizzi, Junfeng Qiao, Norma Rivano, and the AiiDA team
<https://aiida-team.github.io/aiida-registry/plugins/wannier90.html>.

Talks and posters

- Mar 2023 **Contributed talk** – APS March Meeting 2023, Las Vegas, Nevada
Novel high-mobility candidates from the Materials Cloud 2D database
- Nov 2022 **Invited talk** – MODL seminar, Louvain-la-Neuve (Université catholique de Louvain), Belgium
Dimensionality signatures on infrared-active phonons, electron-phonon coupling and charge transport
- Aug 2022 **Contributed talk** – Psi-k Conference 2022, École polytechnique fédérale de Lausanne, Switzerland
Breakdown of LO-TO polar splitting in 1D materials: dimensionality signatures and their spectroscopic relevance
- Mar 2022 **Contributed talk** – APS March Meeting 2022, online
Breakdown of LO-TO polar splitting in 1D materials and its application to nanowires and nanotubes
- Feb 2022 **Invited talk** – ETSF Seminar, online
Breakdown of LO-TO polar splitting in 1D materials and its application to nanowire and nanotubes
- Sep 2021 **Contributed talk** – The 17th ETSF young researchers' Meeting (2021), Cagliari, Italy
Breakdown of LO-TO polar splitting in 1D materials and its application to nanowires and nanotubes
- Mar 2021 **Contributed talk** – APS March Meeting 2021, online
Breakdown of LO-TO polar splitting in nanowires
- Jan 2019 **Poster** – 19th International Workshop on Computational Physics and Materials Science: Total Energy and Force Methods (2019), Trieste (ICTP), Italy
Thermal transport in one-dimensional carbon chains: a first-principles relaxon approach